# Weak Lensing–X-ray Scaling Relations for a High Redshift Galaxy Clusters Sample

Dissertation
zur
Erlangung des Doktorgrades (Dr. rer. nat.)
der
Mathematisch-Naturwissenschaftlichen Fakultät
der
Rheinischen Friedrich-Wilhelms-Universität Bonn

von
Alberto Doria
aus
Bari, Italien

Bonn, 05.09.2016

Dieser Forschungsbericht wurde als Dissertation von der Mathematisch-Naturwissenschaftlichen Fakultät der Universität Bonn angenommen und ist auf dem Hochschulschriftenserver der ULB Bonn `http://hss.ulb.uni-bonn.de/diss_online` elektronisch publiziert.

| | |
|---|---|
| 1. Gutachter: | Prof. Dr. Thomas H. Reiprich |
| 2. Gutachter: | Prof. Dr. Peter Schneider |
| Tag der Promotion: | 11.04.2017 |
| Erscheinungsjahr: | 2017 |

# Abstract

Galaxies have the inclination of being attracted by each other, gathering in structures which represent the largest gravitationally bound objects in the universe: galaxy clusters. The possibility to conduct multiwavelength analysis with different approaches on these giants, brings us toward a better understanding of the origin, the physics and the history of the universe we live in.

Galaxy clusters are a powerful tool for several relevant studies, such as the behavior of gas in a dense and hot environment, the interplay between active galactic nuclei and the surrounding medium, investigation on the dark matter and dark energy nature.

One of the major challenges of today's astrophysics and cosmology is to develop a deeper knowledge of dark energy. In the standard cosmological model, our universe is constituted for about 70% by this "mysterious" component, which is supposed to be responsible for the accelerated expansion of our universe. The main approach to this problem by means of galaxy clusters, is to count these objects with a given mass at a given redshift. X-ray observations provide an excellent tool for galaxy cluster detection, as the hot gas of those objects yields an extended emission at short wavelengths. Furthermore, X-ray galaxy cluster masses rely on the spherical symmetry and the hydrostatic equilibrium assumptions. This induces systematics that are consequently reflected on the study of the correlation between several X-ray observables (i.e., mass-luminosity, mass-temperature, etc.).

Accurate cosmology through large X-ray selected galaxy cluster samples will rely on accurate mass estimates and well-calibrated mass-observable relations. The comparison of independent approaches, such as X-ray and gravitational lensing analysis, yields the most accurate results in tracing the cosmic evolution. This also contributes to improve our understanding of the scaling laws between X-ray luminosity and mass ($L_{\rm X}$–$M_{\rm tot}$), providing the essential connection between observations and cosmological constraints that will be obtained thanks to the forthcoming *eROSITA* X-ray space telescope.

Our project aims at the mass estimation via the weak lensing follow-up of the cosmological subsample of the *400d Galaxy Cluster Survey*: a homogeneous, statistically complete and flux limited X-ray sample of 36 high-redshift ($0.35 \leq z < 0.90$) clusters, covering an as yet unexplored region in the mass-redshift parameter space.

In this thesis methods and results are presented of the cluster mass estimation through homogeneous weak lensing analysis of 18 galaxy clusters.

For our purposes we use optical data from archival and granted observations at ground-based instruments: *IMACS*, *WFI* and *MegaCam* wide-field cameras. Given the poor quality of the data of the *IMACS* camera, we modify the `THELI` data reduction pipeline (Erben et al. 2005) and implement a method for recovering precious astrometric information.

We provide revised scaling relations of weak lensing mass with several X-ray observables ($L_{\rm X}$, $T_{\rm X}$, $Y_{\rm X}$, $f_{\rm g}$) integrating the new data with updated masses from the previous work of Israel et al. (2012), basing on a total of 25 high-$z$ clusters ($\langle z \rangle = 0.48$). We compare our results with the X-ray work of Vikhlinin et al. (2009a) and recent mass comparison projects.

Recent insights from the *Planck* mission reveal a disagreement between the primary cosmic microwave background data and the Sunyaev-Zel'dovich cluster count cosmology. Therefore, the cross-calibration between different methods gains more relevance and weak lensing can be used as an impartial probe to inspect on this tension.

We find a hint for a mass-dependent mass bias $\langle \log_{10}(M^{\rm X}/M^{\rm WL}) \rangle$, with X-ray mass estimates of

low-mass clusters (w.r.t. the sample median mass) being biased-high ($\langle M^{\rm X}\rangle = (1.477 \pm 0.174)\langle M^{\rm WL}\rangle$), while they are biased-low at the high-mass end ($\langle M^{\rm X}\rangle = (0.794 \pm 0.078)\langle M^{\rm WL}\rangle$). However, the overall trend is consistent with the zero bias ($\langle M^{\rm X}\rangle = (1.069 \pm 0.105)\langle M^{\rm WL}\rangle$), hence not showing any indication for a strong cluster mass bias which would be needed to alleviate the *Planck* CMB-cluster tension.

# Contents

CHAPTER 1

# Preface

While astronomy is the oldest of all sciences, cosmology is a relatively recent branch. The simple observation of the sky with naked eyes opens a plethora of questions about what happens outside our planet. Technical progress helps scientists to address an increasing number of questions of this kind, with the consequence of opening more and more interrogatives, triggering a loop of expansion of the human knowledge.

Cosmologists and astrophysicists investigate on the evolution and composition of the Universe, trying to retrace its whole history. This challenge is more ambitious than it appears, as what we actually see through our eyes and instruments is only a tiny part of what our Universe is made of. We observe planets, stars, galaxies, galaxy clusters thanks to the baryons they are made of; but this is just the tip of the iceberg. What we do not directly observe are "invisible" components such as dark matter and dark energy, which we can luckily trace thanks to their effects in extragalactic astrophysics. The current cosmological paradigm, also known as the $\Lambda$CDM model, is based on the combination of these two invisible contributors.

Zwicky (1933) introduced for the first time the idea of a "dark" matter, as his observations of huge systems like galaxy clusters could not be justified by baryonic matter only. Nowadays it is known that dark matter accounts for about 80% of the total matter contribution and its transparency is explicable by the fact that it does not interact with the ordinary matter. Despite being collisionless, dark matter or, more precisely, cold dark matter (CDM) shows its presence through gravitation.

At the very end of the XX century, Riess et al. (1998) and Perlmutter et al. (1999) observations of type-Ia supernovae brought the first evidence of the accelerated expansion of the universe, as predicted decades before by Albert Einstein with the introduction of the cosmological constant $\Lambda$. This discovery has been having numerous confirmations via other techniques, and in the early 2000's brought the Dark Energy Task Force (Albrecht et al. 2006, DETF) and the ESA-ESO Working Group on Fundamental Cosmology (Peacock et al. 2006) to consider the opportunity of coordinating and combining the different methods to improve the precision in constraining dark energy.

The most promising results are obtained mainly through supernovae studies, cosmic microwave background, galaxy cluster surveys, baryonic acoustic oscillations, and weak gravitational lensing. All these approaches contribute to a better understanding of dark energy properties and evolution, exploiting the expansion history and the growth of structure. For this reason astrophysics and cosmology are living exciting times: not only there has been a good number of experiments active in the field but, in the very near future, a breakthrough is expected thanks to several forthcoming missions. The imminent launch of the *eROSITA/SRG* satellite (Predehl et al. 2010; Merloni et al. 2012) and the *Euclid* mission (Laureijs 2009) will have a major impact on the constraining precision for testing cosmological models.

In this thesis we study the most massive gravitationally-bound objects in our Universe, galaxy clusters, which are unique laboratories both for astrophysics and cosmology. The aforementioned *eROSITA* instrument will conduct a 4-years sky survey in the X-ray band, yielding with unprecedented sensitivity a census of the galaxy clusters in the Universe. The estimation of the mass of galaxy clusters at different epochs provides important insights on the geometry and evolution of our Universe. However, observational methods suffer from systematic uncertainties which need to be cross-calibrated with techniques based on different assumptions, in order to enhance the accuracy of cluster cosmology.

This work aims to push the study of scaling relations to the low mass and high redshift regime, through a detailed weak lensing study of a sample with a well-known selection function. Scaling laws between X-ray observables and weak lensing masses will play a strong supportive role in large cluster surveys: they provide a more feasible approach, preferred over the calculation of X-ray hydrostatic masses. The focus of this work is the investigation of the correlation of galaxy cluster masses estimated with two different approaches: X-ray and weak gravitational lensing. We report methods and results of the cluster mass estimation through a homogeneous weak lensing analysis of a subsample of the *400d Galaxy Cluster Survey*: a catalog of serendipitous detections obtained with the *ROSAT* X-ray telescope (Burenin et al. 2007). Vikhlinin et al. (2009a) select a complete sample of 36 high redshift ($0.35 \leq z < 0.90$) clusters, to study the cluster mass function through dedicated X-ray *Chandra* observations (Vikhlinin et al. 2009b). Our project consists in the weak lensing follow-up of this cosmological sample, the *400dCS*. In this thesis we provide a detailed analysis of 18 clusters and, including the eight *400dCS* clusters studied in Israel et al. (2012), we provide X-ray-weak lensing scaling relations for a final subsample of 25 galaxy clusters.

An overview on the basic concepts of cosmology is provided in Chapter 2, dedicated to the introduction of the cosmological model that describes our Universe and its composition. Also, we treat the formation and growth of the cosmic structures that we observe nowadays.

The objects studied in this thesis are galaxy clusters. A multiwavelength perspective on them, as well as the description of why they are an important tool for advancements in cosmology, is given in Chapter 3.

In Chapter 4, we briefly introduce the foundations of gravitational lensing, with a special focus on the weak lensing techniques, which we exploit for our mass reconstruction.

The advancements and results of this work are presented in Chapters 5–7 and will be published in Doria et al., in preparation. After a brief introduction of the *400dCS* and the optical data of our follow-up, collected from three different ground telescopes. In Chapter 5 is shown how we process our data from raw images to the compilation of the galaxy shape catalogs, including our checks for systematics. Chapter 6 is dedicated to the background galaxy selection and the estimation of the weak lensing masses. In Chapter 7 we provide revised scaling relations of weak lensing masses with several X-ray observables, basing on a total of 25 high redshift clusters. Our results are compared with with the X-ray work of Vikhlinin et al. (2009a) and recent mass comparison projects by other groups.

Our findings are finally summarized in Chapter 8, including an outlook to future perspectives.

CHAPTER 2

# Cosmology

A better understanding of the nature, origin and evolution of the Universe is one of most intricate but compelling tasks in modern astrophysics. In the last fifty years cosmology has progressed in a way that theories can be easily investigated by well-designed experiments, conceived for empiric validation of natural laws using the latest available technologies.

Those theoretical models are characterized by a set of cosmologial parameters which not only describe the overall dynamics of the Universe and its matter composition budget, but also the nature of perturbations and the Universe physical state. The currently most accepted cosmological model, also called "concordance model" or "ΛCDM model", builds on Einstein's *general relativity* and on the *Friedmann-Lemaître-Robertson-Walker metric*. It asserts that our universe is infinite and it consists not only by ordinary matter which accounts for the 5% of its total composition, but also for the 25% by collisionless *dark matter* and for the 70% by *dark energy*.

This work is centered on the study of galaxy clusters: important bricks of our Universe, interesting both for they physics and for their cosmological role. For this reason, in this Chapter are laid the groundwork for the understanding of the theory behind our results. In particular, in Section 2.1, we give an overview on the basic concepts of cosmology and the different cosmological models. Section 2.1.4 treats the understanding of geometry of the Universe through distance definitions. Dark matter and dark energy are briefly presented in Sections 2.1.2 and 2.1.3, while the growth of cosmic structure is the central topic of Section 2.2.

The concepts treated in this Chapter are in great part based on Peacock (1999); Coles & Lucchin (2002); Mortonson et al. (2014); Schneider (2015).

## 2.1 Einstein's Legacy and the Concordance Model

Einstein's major scientific success is the *Theory of General Relativity*, which introduces a four-dimensional universe (space-time) described by a metric tensor: $g_{\alpha\beta}$. The first and second derivatives of this metric, describe the *Einstein tensor* $G_{\alpha\beta}$, which is part of *Einstein's fields equations*:

$$G_{\alpha\beta} = -\frac{8\pi G}{c^2} T_{\alpha\beta} - \Lambda g_{\alpha\beta} \quad . \tag{2.1}$$

The content of the matter of the Universe is related to the energy-momentum tensor $T_{\alpha\beta}$, with matter and radiation considered ideal fluids. $\Lambda$ is what Einstein proposed as *cosmological constant*, initially to obtain a static universe, but modern observational evidence turned it to be responsible for the acceleration of the universe expansion. $G$ and $c$ are the gravitational constant and the speed of light in vacuum, respectively.

### 2.1.1 The ΛCDM Universe

A solution to Einstein Field Equations can easily be found by applying the *cosmological principle* which states that the Universe is *homogeneous* and *isotropic* on large scales for any comoving observer (which moves along with the expansion). A geometrical description which gives an exact solution to equation (2.1) satisfying these two fundamental postulates, is the Friedmann-Lemaître-Robertson-Walker (FLRW) metric (independently defined by Friedmann 1922; Lemaître 1933; Robertson 1935; Walker 1937)

$$\mathrm{d}s^2 = g_{\alpha\beta}\,\mathrm{d}x^\alpha \mathrm{d}x^\beta = c^2\mathrm{d}t^2 - a^2(t)\,\mathrm{d}r^2\ ; \quad \mathrm{d}r^2 = \mathrm{d}\chi^2 + f_K^2(\chi)\left(\mathrm{d}\Theta^2 + sin^2\Theta\mathrm{d}\Phi^2\right) \tag{2.2}$$

where $a(t)$ is the *scale factor* (normalized such that at the present epoch $t_0$: $a_0 = a(t_0) = 1$), and $dr$ is the comoving line element of a three-dimensional space with constant curvature. $f_K(\chi)$ is a function which depends on the space curvature K:

$$f_K(\chi) = \begin{cases} \frac{1}{\sqrt{K}}\left(\sqrt{K}\chi\right) & K > 0 \\ \chi & K = 0 \\ \frac{1}{\sqrt{-K}} sinh\left(\sqrt{-K}\chi\right) & K < 0 \end{cases} \tag{2.3}$$

The three curvature cases in the equations (2.3) describe a closed universe ($K > 0$), a flat universe ($K = 0$) and an open universe ($K < 0$). The expansion of the space-time metric implies that if at time $t_1$ a photon is emitted with a wavelength $\lambda_\mathrm{e}$, when observed at later time $t_2 > t_1$ its wavelength $\lambda_\mathrm{obs}$ has been shifted towards red ("redshifted") to a value given by:

$$1 + z = \frac{a(t_2)}{a(t_1)} = \frac{\lambda_\mathrm{obs}}{\lambda_\mathrm{e}} = \frac{1}{a(t)} \quad . \tag{2.4}$$

Solving Einstein's field equations (2.1) using the FLRW metric (equations (2.2)) provides two equations that describe the evolution of the scale factor $a(t)$, the *Friedmann equations*:

$$\frac{\ddot{a}}{a} = -\frac{4\pi G}{3}\left(\rho + \frac{3p}{c^2}\right) + \frac{\Lambda c^2}{3} \quad , \tag{2.5}$$

$$\left(\frac{\dot{a}}{a}\right)^2 = \frac{8\pi G}{3}\rho - \frac{Kc^2}{a^2} + \frac{\Lambda c^2}{3} \quad . \tag{2.6}$$

The initial role of the cosmological constant $\Lambda$ was to obtain a static universe, which has been proved wrong from the discovery of the expansion. Details about it and the parametrization of dark energy are contained in Section 2.1.3.

The first Friedmann equation (2.5) describes the accelerated expansion, while the second equation (2.6) delineates the expansion rate of the universe, commonly described by the *Hubble parameter*:

$$H = \frac{\dot{a}(t)}{a(t)} \quad . \tag{2.7}$$

At the present epoch, $t_0$, it is called the *Hubble constant*:

$$H_0 = \frac{\dot{a}(t_0)}{a(t_0)} = \frac{\dot{a}_0}{a_0} \tag{2.8}$$

and it is measured via several probes. Recent measurements of this constant give $H_0 \approx 67.74 \pm$

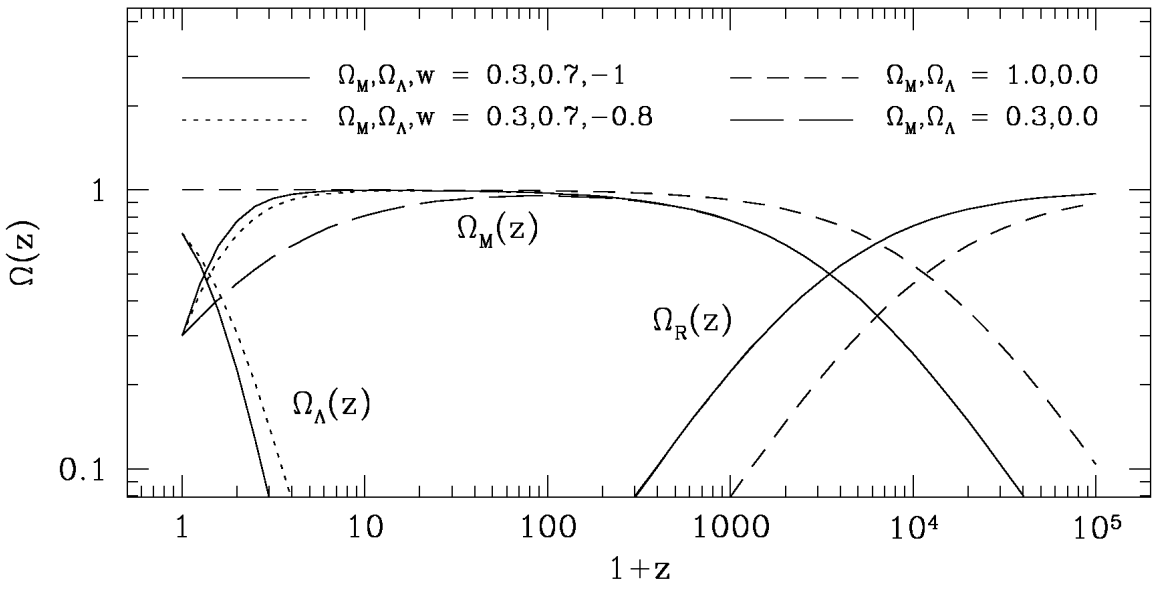


Figure 2.1: Evolution of the energy densities of matter, radiation and dark energy for four different cosmological models. The solid line indicates the ΛCDM model, the long-dashed line shows a low density universe without dark energy, the short-dashed is the Einstein-de Sitter universe. The dotted line is similar to the ΛCDM, but with a different value for the $w$-parameter of dark energy. Radiation dominates at very high redshift in all four cases but, at $z \sim 10^4$ $\Omega_\mathrm{m}$ takes the lead. Dark energy becomes important only recently: after a quick growth of its energy density, it becomes dominant at $z \sim 0.5$. Credit: Voit (2005).

$0.46\,\mathrm{km\,s^{-1}\,Mpc^{-1}}$ (Planck Collaboration et al. 2015b). Its value can also be parametrized by the dimensionless variable $h = H_0/(100\,\mathrm{km\,s^{-1}\,Mpc^{-1}})$. Inverting the Hubble constant yields the *Hubble time*: $H_0^{-1} \approx 10h^{-1}\,\mathrm{Gyr}$, which would equal the age of the Universe for a constant expansion rate. From equation (2.6) it is also easy to note how the geometry of the Universe, represented by the curvature $K$, is strictly linked to the density.

The *Einstein-de Sitter universe* is a model where the total energy density comes only from matter ($\Omega_\mathrm{m} = 1$, $\Omega_\Lambda = 0$) in a flat universe.

It is possible to define a *critical density*:

$$\rho_{crit}(t) = \frac{3H^2(t)}{8\pi G} \quad , \tag{2.9}$$

which also relates the density to the Hubble constant. For a parametrization of the model of our Universe, the *density parameters* can be defined by scaling each density component by the critical density:

$$\Omega_\mathrm{x} = \frac{\rho_\mathrm{x}}{\rho_\mathrm{crit}} \tag{2.10}$$

where x = {m, r, b, DE} which stand for matter, radiation, baryons and dark energy, respectively. With the expansion of the Universe, these energy densities evolve with time following different trends. As it is safe to treat the universe as a perfect fluid, the definition of an *equation of state* is needed:

$$p = w\rho c^2 \tag{2.11}$$

where the parameter $w$ is constant. From the Friedmann equation it is also possible to derive the general evolution of the density:

$$\rho = \rho_0 a^{-3(1+w)} \tag{2.12}$$

which involves the $w$ parameter of the equation of state. For an ideal gas of non-degenerate, ultrarelativistic particles in thermal equilibrium, $w = 1/3$. While, for a "dust" universe, i.e. made only by non-relativistic matter, $w = 0$ as the pressure $p = 0$. The scale factor (or redshift) dependency from matter, radiation and dark energy density is given by:

$$\begin{aligned} &\rho_\mathrm{m} \propto a^{-3} && \rho_\mathrm{m} \propto (1+z)^3 \\ &\rho_\mathrm{r} \propto a^{-4} && \rho_\mathrm{r} \propto (1+z)^4 \\ &\rho_\mathrm{DE} \propto a^{-3(1+w)} && \rho_\mathrm{DE} \propto (1+z)^{3(1+w)} \quad . \end{aligned} \tag{2.13}$$

Figure 2.1 illustrates how the energy density of the different components of the Universe contribute to its total energy. Different universe models show different swap points, but confirm the trend of having a single dominant component at the time. There are only two exceptions during the whole cosmic evolution: at $z \sim 10^4$, when matter took over on radiation, and more recently at $z \sim 0.5$ where the dark energy density started to be an important contributor to today's Universe composition.

In the light of equations (2.7), (2.10) and (2.13), the Friedmann equation (2.6) can be rewritten in terms of all density parameters as:

$$H^2 = H_0^2 \left[ \Omega_\mathrm{m} a^{-3} + \Omega_\mathrm{r} a^{-4} + \Omega_\Lambda + \Omega_\mathrm{K} a^{-2} \right] \tag{2.14}$$

where $\Omega_\mathrm{K} = 1 - \sum \Omega_\mathrm{TOT}$ is the curvature parameter. The bracket of the right-hand term is (rewritten in terms of redshift)

$$E(z) = \sqrt{\Omega_\mathrm{m}(1+z)^3 + \Omega_\mathrm{r}(1+z)^4 + \Omega_\mathrm{DE} + \Omega_\mathrm{K}(1+z)^2} \tag{2.15}$$

and it is called the *redshift evolution factor* which, for a flat universe ($\Omega_\mathrm{K} = 0$) with negligible radiation density and constant dark energy density, can be reformulated as:

$$E(z) = \sqrt{\Omega_\mathrm{m}(1+z)^3 + \Omega_\Lambda} \quad . \tag{2.16}$$

This quantity is extremely useful in order to scale galaxy cluster masses, to make them independent from the critical density at their redshifts.

### 2.1.2 Dark Matter

The energy density contribution of matter is not only composed by the "visible" baryons but also by an invisible component: dark matter (DM). More precisely, dark matter accounts for ~80% of the total matter density. Neglecting neutrinos, which do not have a strong impact on structure formation with their ~0.4% of contribution, the total matter energy density can be seen as

$$\Omega_\mathrm{m} = \Omega_\mathrm{b} + \Omega_\mathrm{DM} \quad . \tag{2.17}$$

The presence of dark matter is predicted by several probes. The first time it was introduced dates back to 1933 when Zwicky suspected that baryons only could not explain the existence of a such massive and gravitationally bound system as the Coma cluster. Furthermore, it has been shown that the rotation curves of galaxies needed the contribution of a significant amount of invisible matter to be explained. The invisibility of dark matter is then due to its null interaction with the electromagnetic field, being

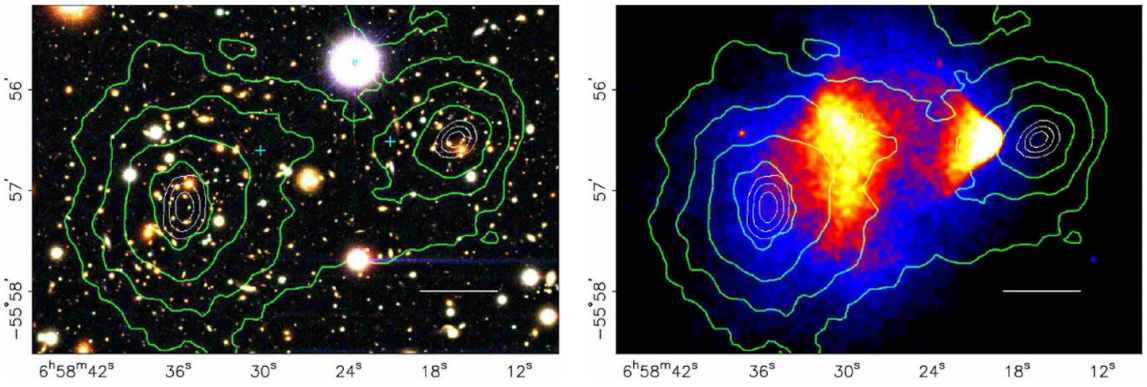


Figure 2.2: The *Bullet cluster* (or 1E0657-558), studied for the first time by Clowe et al. (2004) and proposed as the observational evidence for the existence of dark matter. Looking only at the optical image with the weak lensing contours overlaid on it (*left panel*), one would notice only two separated distributions of galaxies, followed by the lensing signal. However, adding the X-ray information (*right panel*), shows that this clusters is in a clear merging state. The intracluster gas shows two different peaks (white is hottest and blue is coolest) which are offset from the lensing peaks (green contours). Also, its distribution give the hints that the right X-ray clump is the "bullet" who crossed the leftmost one. Credit: Clowe et al. (2006).

impossible to be detected directly. However, two candidates for non-baryonic dark matter have been proposed: hot dark matter (HDM) and cold dark matter (CDM). The difference between two is that HDM would favor relativistic particles (e.g., neutrinos) as dark matter candidates; while CDM could consist of non-relativistic particles which are currently only hypothetical.

An indirect method to "detect" dark matter exists and consists in the observation of galaxy clusters formed by merging of two smaller clusters. One expects to see the hot baryons of one of the two initial clusters interacting with the baryons of the other. Meanwhile, the galaxies meet and cross each other undisturbed. Dark matter, being collisionless, is supposed to follow the same behavior of galaxies. This finds the support of combined X-ray and weak lensing observations: the first, tracking the intracluster gas interaction; the second, following the potential of the dark matter halos. The first observation of this phenomenon was the "Bullet cluster" (Clowe et al. 2006, illustrated in Figure 2.2). Nowadays a handful of "Bullet-like" clusters have been studied in detail with the support of both X-ray and optical observations.

### 2.1.3 Dark Energy

As seen in the Friedmann equations, the introduction of the cosmological constant by Einstein was motivated by the need of a static universe. This requirement is satisfied by

$$\Lambda_{\mathrm{E}} = \frac{4\pi G\rho}{c^2} \quad , \tag{2.18}$$

which would indeed produce a static model, but unstable against small perturbations.

After the discovery of the expansion of the Universe, $\Lambda$ was set aside. More recently, it has been called back into play for describing the accelerating expansion of our Universe.

It is easy to note that in the last case of equation (2.13), a value $w = -1$ would yield the particular case of the cosmological constant, $\Lambda = \mathrm{const}$. The $\Lambda$CDM universe is indeed based on the fact that dark energy behaves like the cosmological constant. However, $w$ in equation (2.12) can also assume a different

value, allowing the dark energy density to vary during the cosmic epoch. As a consequence, it is possible to parametrize $w$ in dependency of the scale factor via a linear evolution model:

$$w(a) = w_0 + w_a(1 - a) \quad . \tag{2.19}$$

The suggestion of a non-constant $w$ would trigger a change in the expansion rate of the universe (equation (2.14)). For the case of a time-dependent $w$, the dark energy dependency on the scale factor can be generalized as:

$$\rho_{\mathrm{DE}}(t) = \rho_{\mathrm{DE},0}\exp\left(-3\int_0^{a(t)} \frac{1}{a}\left[1 + w(a)\right]\mathrm{d}a\right) \quad . \tag{2.20}$$

Different cosmological probes are used to investigate on $w$, such as type Ia supernovae (SNIa), baryon acoustic oscillations (BAOs), cosmic shear and galaxy clusters. Their results all converged to the finding that dark energy started to dominate only very recently. However, these measurements have large systematics which need hard work to be understood. In particular, for galaxy clusters it is of crucial importance to calibrate the observable-mass relation, for more accurate constraints on the dark energy equation of state.

### 2.1.4 Cosmological Distances

A unique definition of distance in a non-Euclidean or expanding space-time does not exist. Unlike for a Euclidean space, there are various definitions of cosmological distances. The most relevant for the topics treated in this thesis is the *angular diameter distance*, which relates the physical diameter $d$ of an observed object to the angular diameter $\Theta$ it subtends on the sky:

$$D_{\mathrm{A}} = \frac{d}{\Theta} = \frac{f_K(\chi)}{(1 + z)} \quad . \tag{2.21}$$

In our lensing analysis (see Chapter 6) we turn to the following expression to calculate the angular diameter distance between two objects at two different redshifts ($z_2 > z_1 > 0$):

$$D_{\mathrm{A}}(z_1, z_2) = \frac{1}{1 + z} f_K\left(\chi(z_2) - \chi(z_1)\right) \quad . \tag{2.22}$$

The prefactor $(1 + z)^{-1} = a$ in equation (2.22) prevents the angular diameter to grow infinitely when $z_2$ goes at extremely high redshifts. As an example, fixing $z_1 = 0$, the objects observed beyond $z \sim 1.4$ can appear bigger than objects with the same $d$ but a lower redshift. This means that $D_{\mathrm{A}}$ is not additive: $D_{\mathrm{A}}(z_1, z_2) \neq D_{\mathrm{A}}(z_2) - D_{\mathrm{A}}(z_1)$.

A second distance definition also worth to mention is the *luminosity distance*. It relates the source flux $f$ to its intrinsic luminosity via the relation

$$D_{\mathrm{L}} = \sqrt{\frac{L}{4\pi f(z)}} \quad , \tag{2.23}$$

which is related to the angular diameter distance as

$$D_{\mathrm{L}}(z) = (1 + z)^2 D_{\mathrm{A}}(z) = (1 + z) f_K(\chi) \quad . \tag{2.24}$$

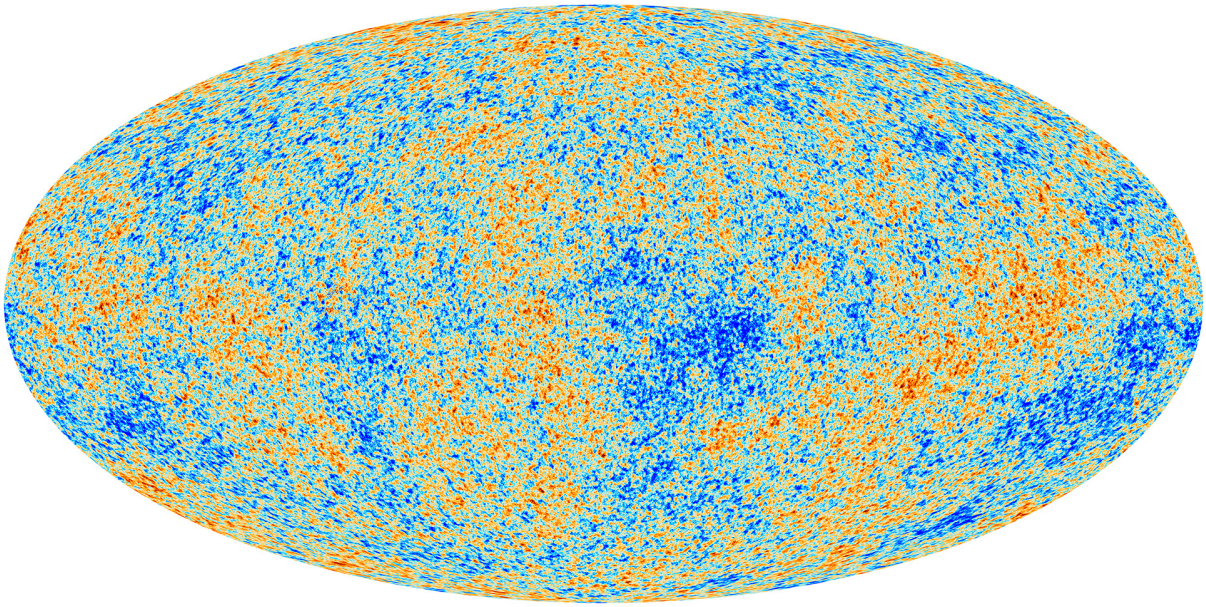

Figure 2.3: The Cosmic Microwave Background temperature radiation as seen by *Planck*. The red areas on this temperature map are slightly warmer than the colder blue areas. Credit: ESA and the Planck Collaboration.

The $\chi(z)$ used in the previous definitions is the *comoving distance*

$$\chi(z) = \int_0^z \frac{\mathrm{d}z'}{H(z')} \tag{2.25}$$

which factors out the expansion of the universe, hence the distance between two objects which passively follow the space-time expansion remains constant.

To define a boundary to the portion of the universe we can observe, we use the *cosmological horizon*:

$$R_H = \int_0^\infty \frac{c}{a^2 H(a)} \mathrm{d}a \quad , \tag{2.26}$$

that is the maximum scale within which an event can be casually connected with an observer.

## 2.2 Cosmic Structure Formation

The central topic of this study is the mass estimation of clusters of galaxies, which are massive virialized conglomerates of galaxies, baryons and dark matter. While galaxy clusters will be treated more in detail in Chapter 3, here we focus on how they have been built.

The overview on the energetic content of the universe introduced in the above sections is based on the cosmological principle assumption. However, despite the space-time we live in is indeed homogeneous on large scales, on scales smaller than few hundreds of megaparsecs, density perturbations are imprinted on a smooth background. These fluctuations have been discovered in 1964 as part of a residual radiation of the early universe: the *Cosmic Microwave Background* (*CMB*). Several missions, such as *COBE*, *WMAP* and *Planck* had the task to study it. They accomplished to measure its spectrum, which is a close-to-perfect blackbody with a temperature T $\approx$ 2.725 $\pm$ 0.0006 K. With this high precision measurement it is possible to map the very small excesses and depressions from the background radiation

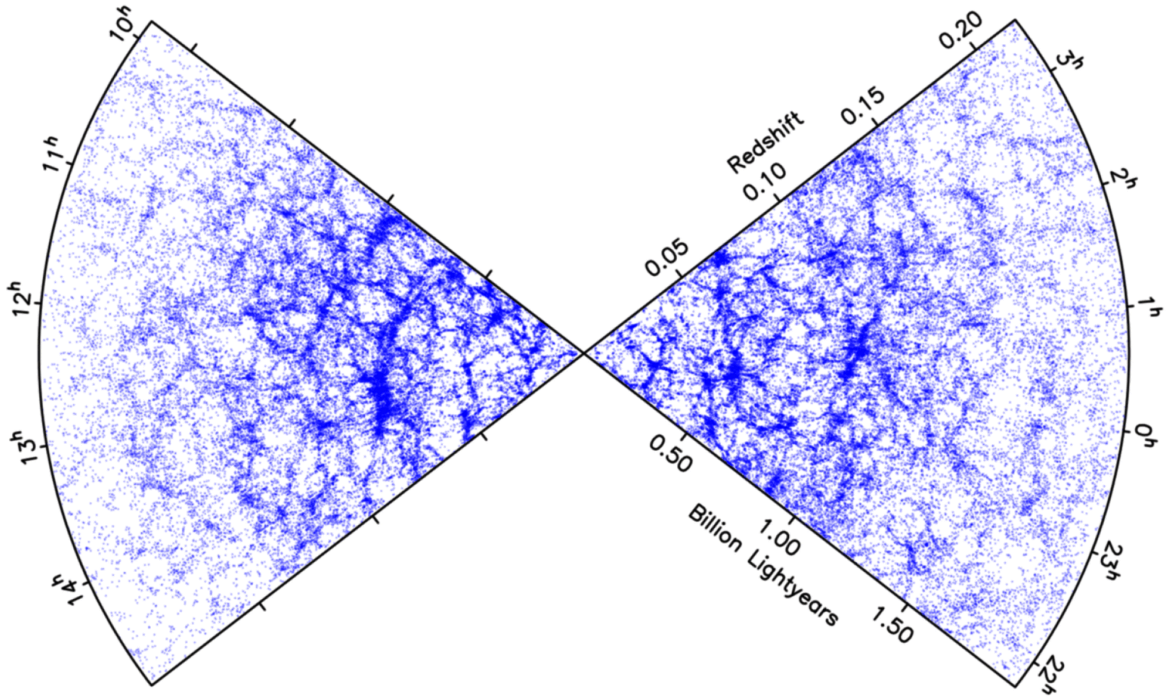


Figure 2.4: Distribution of galaxies in the 2dF Galaxy Redshift Survey. The redshifts have been measured through spectroscopic observations and are displayed in the radial direction. The projected map includes only the reliable spectroscopic redshift measurements, which sum to ≳200 thousand. This is a striking observational probe of the fact that matter follows denser clustered structures, voids and filaments. Credit: 2dFGRS-team.

($\Delta T/T \approx \Delta\rho_{\rm baryon}/3\rho_{\rm baryon} \approx 10^{-5}$), yielding the spatial distribution of baryonic matter at the epoch of its last interaction with radiation ($z \approx 1090$, Planck Collaboration et al. 2015b). Figure 2.3 represents the first picture of the Universe, when it was only ∼380 thousand years old and it has been obtained from *Planck* observations. It also represents the starting point from where structures take shape via gravitational instability. Denser regions collapse into *overdensities* (red color) dragging from the surrounding areas even more matter through *filaments*. The neighboring regions lower their density becoming the so-called *voids*. All these peculiarities are easily visible in the three-dimensional (coordinates plus redshift) reconstruction of the "cosmic web" pursued by the spectral study of more than 200 thousand galaxies in the *2dF Galaxy Redshift Survey* (Figure 2.4). The global distribution of matter in the universe is called *Large Scale Structure* (LSS).

Cosmic microwave background observations, constraining the fraction of massive neutrinos as dark matter particles, rule out the HDM model (discussed in Section 2.1.2) as relativistic particles would escape from the small primordial perturbation of the universe. Finally, CDM favors the hierarchical clustering, bottom-up scenario of structure formation, which requires the building of the structures from small to large scales.

Despite the big importance of the CMB for the advancements in cosmology, we refer to e.g. Hu & Dodelson (2002) for a detailed summary. In this context we are more interested to see how those tiny perturbations could lead the Universe to appear how we see it today: filled with structures which are clumps of matter forming stars, galaxies, galaxy clusters and superclusters.

### 2.2.1 Linear Growth

From the puny density fluctuations observed in the CMB ($\sim 10^{-5}$) to the densities of the order of $100\rho_{\mathrm{crit}}$ observed in local galaxy clusters, the universe has undergone a serious growth. Approximating with the linear perturbation theory the growth of structure, one needs to assume that the initial density perturbations are small. It is possible to define a *relative density contrast*

$$\delta(\vec{x},t) = \frac{\Delta\rho(\vec{x},t)}{\bar{\rho}(t)} = \frac{\rho(\vec{x},t)-\bar{\rho}(t)}{\bar{\rho}(t)} \ll 1 \quad , \tag{2.27}$$

where $\rho(\vec{x},t)$ is a *Gaussian random field* in comoving coordinates and $\bar{\rho}(t)$ is the mean density. In this approximation, dark energy is purely the cosmological constant and only scales smaller than the horizon $R_{\mathrm{H}}$ (equation (2.26)) can be considered in order to adopt Newtonian gravity. Hence, a self-gravitating fluid can be described by three formulae in terms of random field $\rho(\vec{x},t)$, peculiar velocity $\vec{v}(\vec{x},t)$ and scale factor $a(t)$. Those are: the continuity equation which states mass conservation; the Euler equation; and the Poisson equation which denotes the gravitational potential. The evolution of the density contrast can be described by a linear differential equation of the second order:

$$\frac{\partial^2\delta(\vec{x},t)}{\partial t^2} + 2H(t)\frac{\partial\delta(\vec{x},t)}{\partial t} - \frac{3H_0^2\Omega_{\mathrm{m}}}{2a^3(t)}\delta(\vec{x},t) = 0 \quad . \tag{2.28}$$

The dependency from the comoving coordinate is only implicit, then the solution can be expressed as a product of separated functions of $\vec{x}$ and $t$

$$\delta(\vec{x},t) = D_+(t)\Delta_+(x) + D_-(t)\Delta_-(\vec{x}) \quad , \tag{2.29}$$

where $D_-(t)$ and $D_+(t)$ are the decaying and growing solution, respectively. The first solution can be excluded as it leads the perturbation to a quick decline, thus it does not play any role in the inhomogeneities growth. On the other hand, $D_+(t)$ describes the time evolution of growing perturbations, which can be expressed analytically only for a universe with a cosmological constant ($w = -1$) as:

$$D_+(a) \propto \frac{H(a)}{H_0}\int_0^a \left(\Omega_{\mathrm{m}}a^{-1} + \Omega_{\mathrm{r}}a^{-2} + (1-\Omega_0) + \Omega_\Lambda a^2\right)^{-3/2}\mathrm{d}a \quad . \tag{2.30}$$

A numerical solution of equation (2.29) is required for all the other cases. For a broader application to other cosmological models, this positive mode is usually normalized by $D(t_0) = 1$, giving the so-called *growth factor*:

$$D \equiv D_+(a) = \frac{D_+(a)}{D_+(1)} \tag{2.31}$$

and would describe the current fluctuation if their evolution would have been linear.

Given the very large density contrasts observed in the current universe ($\delta \gg 1$), at the time of photon-baryon decoupling one expects $\delta(z \sim 1100) \gtrsim 10^{-3}$. This value, translated in temperature anisotropies, overestimates by two orders of magnitudes the CMB observational results. This implies that a large portion of the matter content of the universe is not baryonic. When the microwave background was emitted at $z \sim 1100$, dark matter was already at a further stage in the gravitational collapse process than baryons. As baryonic matter and radiation were still coupled, the pressure of the radiation component was still leading the distribution of baryons, preventing them to cool down enough to fall into the potential well already traced by the dark matter.

### 2.2.2 Stochastic Methods and Power Spectrum

The linear approximation (described in Section 2.2.1) allows one to know the evolution of density perturbations with time. However, it fails when one wants to calculate the current density fluctuations, because it is impossible to know the exact value of the density fields at earlier cosmic times. A good approach to solve this problem is to predict the statistical properties of the initial fluctuation field using the information provided by the observed properties of the density field. In this case, density fluctuations $\delta\vec{x}$ at a fixed time are considered to be a realization of a random field. This means that we observe one of the realization of the random field, characterized by given statistical properties. Hence, the density field can be described by its *two-point correlation function*

$$\xi(|\vec{x} - \vec{x}'|) = \langle \delta(\vec{x})\delta^*(\vec{x}') \rangle \quad . \tag{2.32}$$

Given that the density field is assumed isotropic in large enough volumes of the universe, one expects to find the same mean in all volumes, allowing to neglect angles and focusing only on the $\vec{x}$ modulus. As a consequence, it is possible to decompose the Gaussian random field in a sum of plane waves, exploiting their Fourier space properties. Defining $\hat{\delta}(\vec{k}, t)$ as the Fourier transform of the density contrast and using equation (2.31), one can describe an isotropic Gaussian random field by its *power spectrum*

$$P(k) = \langle |\bar{\delta}(\vec{k}, t)|^2 \rangle \tag{2.33}$$

whose evolution is

$$P(k) = D_+^2(t) P_0(k) \quad , \tag{2.34}$$

where $P_0$ is the linearly evolved power spectrum at the present time.

Assuming that at very early cosmic times all fluctuations were smaller than the horizon ($\delta \ll R_\mathrm{H}$), the power spectrum can be modeled with a power law:

$$P(k) \propto A k^n \quad . \tag{2.35}$$

This is a "scale-free" power law, i.e. their logarithmic slope is the same on all scales, hence it is not characterized by a particular physical scale. The *spectral index n* is measured to be slightly below one (Planck Collaboration et al. 2015b), well within the range $-3 < n < 1$ required by hierarchical clustering.

The just described linear approximation for evolution of the power spectrum does not hold when the condition $\delta \ll 1$ is broken, or when one considers a radiation dominated universe. Also, as the cosmological horizon is defined by a monotonically increasing function (equation (2.26)), smaller fluctuations enter the horizon earlier, while the larger ones keep growing and cannot be described using Newtonian theory.

More detailed models via higher-order perturbation theory are able to account for the fluctuation of each individual matter density component and the impact of their pressure term. Furthermore, it is also possible to treat the dependency on the size of the perturbations with $R_\mathrm{H}$.

Is not possible to predict the normalization $A$ of the power spectrum (equation (2.35)), thus observations are fundamental in this case. As will be shown in Section 2.2.4, the normalization plays a big role for the galaxy cluster abundance. For this reason, it is preferred to identify $A$ with another parameter $\sigma_8$, which is measured from the observations of the standard deviation of the matter distribution on scales

with radius $r = 8h^{-1}$ Mpc. The parameter $\sigma_8$ is defined as:

$$\sigma_8^2 = \sigma(8h^{-1}\mathrm{Mpc})^2 = \frac{A}{2\pi^2}\int_0^\infty k^{2+n}\,T(k)^2\,W(k\,h^{-1}\mathrm{Mpc})^2\mathrm{d}k \quad , \tag{2.36}$$

where $W$ is a spherical top-hat filter function in linear space which smoothes the mass peaks smaller than the considered mass ($M = 4\pi\rho_{\mathrm{m},0}r^3/3$); $P_{\mathrm{lin}}(k, z)$ is the linear power spectrum. $T(k)$ is the *transfer function*, which is determined by the fact that there is a delay in the growth of the perturbations between the time when they came through the horizon and began to grow again.

The introduction of $\sigma_8$ is due to the observation of a value $\sigma_8 \sim 0.75$ in the local universe at galaxy cluster scales. The degeneracy of $\sigma_8$ and $\Omega_{\mathrm{m}}$ means that also small fluctuations are able to form structures, as the other parameter will have to compensate, following the opposite trend.

### 2.2.3 Spherical Collapse

As already discussed, when density fluctuations grow and $\delta \not\ll 1$, the structure evolution becomes strongly non-linear and cannot be calculated analytically. Numerical simulations are a powerful tool for the study of the growth of different scales in a non-linear trend, without following a Gaussian approximation of the density field. Figure 2.5 shows the state-of-the-art of those simulations: the *Millennium–II* (Boylan-Kolchin et al. 2009). The filamentary structure of the universe is reproduced by these simulations and the knots where dark matter collapse forming galaxy clusters are easily visible.

A simplified but still analytical alternative approach is to analyze the behavior of an inhomogeneity which has a particularly easy shape: a sphere. Adopting an Einstein-de Sitter universe ($\Omega_{\mathrm{m}} = 1, \Omega_{\mathrm{DE}} = 0$), one can place in it a slightly overdense spherical perturbation of constant density. The sphere expands independently from the background universe and its evolution follows the Friedmann model (see Section 2.1). In particular, this spherical overdensity expands slower than the background universe and starts its collapse as soon as it will exceed the critical overdensity. This critical overdensity can be calculated using the linear perturbation theory and results in

$$\delta_c \approx 1.686 \tag{2.37}$$

which is the value of the critical overdensity of collapsed perturbations in the linear regime. As will be discussed in Section 2.2.4, this is linked with the statistics of the collapsed halos. However, for an inhomogeneous sphere (situation closer to reality), the perturbation cannot collapse into a single point. Instead, through *violent relaxation*, it will virialize reaching the equilibrium when the orbital radius of its particles is

$$R_{\mathrm{vir}} = \frac{GM}{2E_{\mathrm{kin}}} \quad , \tag{2.38}$$

where $E_{\mathrm{kin}}$ is the particles kinetic energy. Bryan & Norman (1998) approximated the virial overdensity for a flat universe as:

$$\Delta_{\mathrm{vir}} = \frac{\rho_{\mathrm{vir}}}{\mathrm{crit}} = 18\pi^2 + 82(\Omega_{\mathrm{m}} - 1) - 39(\Omega_{\mathrm{m}} - 1)^2 \quad . \tag{2.39}$$

For what concerns galaxy clusters, their radii are defined with respect to an overdensity rather than on their virialization, which would be difficult to determine exactly. The adopted overdensity radii in the mass estimation of galaxy clusters are discussed in Section 3.2.3.

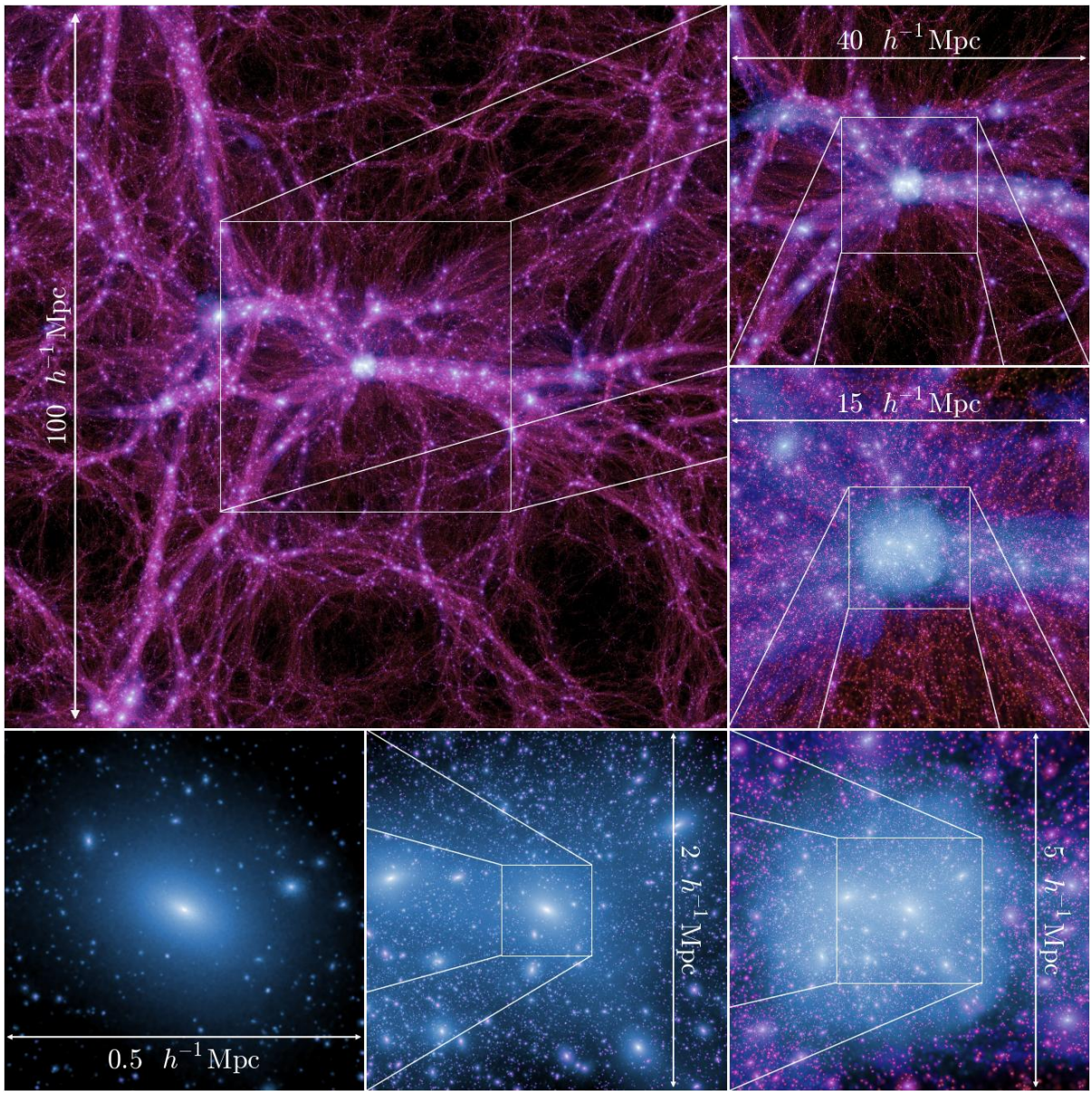


Figure 2.5: Image cuts from the *Millennium II* simulation. This sequence zooms from a scale of 100 Mpc/$h$ to 0.5 Mpc/$h$ into the most massive halo at redshift zero. The filamentary structure of the Universe is well-visible: showing a net of filaments (purple) connecting denser halos (blue). Credit: Boylan-Kolchin et al. (2009).

### 2.2.4 Halo Mass Function

Galaxy clusters sit at the top of the non-linear structure formation and their initial evolution could be approximated by the *spherical collapse* model, the only non-linear approximation which can be solved analytically (see Section 2.2.3). Given the assumptions that a halo collapses into a structure when its overdensity $\delta_{crit} > 1.686$, and that the initial density fluctuations are described by a Gaussian random field, Press & Schechter (1974) proposed a halo mass function as a tool to predict the number of collapsed halos ($N$) given mass and redshift:

$$\frac{\mathrm{d}n(M,z)}{\mathrm{d}M\,\mathrm{d}z} = f(\sigma)\,\frac{\rho_{\mathrm{m},0}}{M}\,\frac{\mathrm{d}\ln\left[\sigma^{-1}(M,z)\right]}{\mathrm{d}M} \quad , \tag{2.40}$$

where $\rho_{m,0}$ is the mean background matter density at redshift zero and $\sigma$ is the variance of the random density field defined by:

$$\sigma^2(M,z) = \frac{1}{2\pi^2}\int_0^\infty k^2\,P_{\mathrm{lin}}(k,z)\,W^2(k,M)\mathrm{d}k \quad , \tag{2.41}$$

where $W$ is the same filter used in equation (2.36).

For the function $f(\sigma)$ in equation (2.40), Press & Schechter (1974) proposed:

$$f_{\mathrm{PS}}\left(\sigma(M,z)\right) = \sqrt{\frac{2}{\pi}}\frac{\delta_{\mathrm{c}}}{\sigma(M,z)}\exp\left(-\frac{\delta_{\mathrm{c}}^2}{2\sigma^2(M,z)}\right) \quad . \tag{2.42}$$

More recently, a number of other parametrizations have been introduced by several authors (Jenkins et al. 2001; Sheth & Tormen 2002; Warren et al. 2006; Tinker et al. 2008), improving the Press & Schechter (1974) formalism, as they fit better with numerical simulations results.

In general, the halo mass function is not much affected by the shape of the power spectrum, but strongly depends on the overdensity $\Delta_{\mathrm{vir}}$ of the halo. Furthermore, it is sensitive to the values of $\Omega_{\mathrm{m}}$ and $\Omega_\Lambda$ and to the normalization of the initial power spectrum through $\sigma_8$ (equation (2.36)).

To fully exploit surveys of galaxy clusters in order to obtain accurate cosmological parameters, the theoretical mass function needs to be calibrated to a precision of less than 10% (e.g., Wu et al. 2010). For this, the effects of baryonic matter have to be included to reduce the uncertainty in the mass function calubration (Cui et al. 2012; Bocquet et al. 2016).

CHAPTER 3

# Galaxy Clusters

Figure 3.1: The local cluster of galaxy Hydra A in a X-ray/radio/optical composite image. The X-ray emission (in blue) overlays the galaxies of the cluster and presents two cavities, which are filled by the radio jets (red). Credit: X-ray: NASA/CXC/U.Waterloo/C.Kirkpatrick et al.; Radio: NSF/NRAO/VLA; Optical: Canada-France-Hawaii-Telescope/DSS.

Galaxies have the inclination of being attracted by each other, gathering in structures which represent the largest mass concentrations in the Universe: clusters of galaxies. These are the largest gravitationally bound objects in the universe with sizes of several megaparsecs and measured masses up to $10^{15}\,M_{\odot}$

(assuming virial equilibrium). The visible mass in galaxy clusters is only a small fraction of the total mass of these collapsed systems (Zwicky 1933), so it is generally accepted that dark matter is the dominant component with a 85% of contribution to the total mass. The remaining 15% is due to baryonic matter, in particular 2% to galaxies and an important 13% to the hot X-ray emitting atmosphere. A typical mass of a galaxy cluster lies between $10^{14}\,M_\odot$ and $10^{15}\,M_\odot$, while smaller overdensities of galaxies (of $\sim 10^{13}\,M_\odot$) are called *galaxy groups*. Galaxy clusters are detectable by multiwavelength observations, where each energy band is able to highlight different features and physics hidden in these interesting objects.

The start of the study of galaxy clusters is dated back to the first years of the XX Century with the first real approach by Wolf (1906). For an early statistically complete catalog five more decades passed until the work of Abell (1958). The interest in clusters of galaxies grew up once that the new born X-ray astronomy began to develop: the first X-ray survey made after the launch of the X-ray satellite *Uhuru* (Giacconi et al. 1972), confirmed the previous hypothesis which stated that these enormous structures were principally high energy emitters (Cavaliere et al. 1971) with typical luminosities $L_X \sim 10^{43} - 10^{45}$ erg/s, being one of the most luminous objects in the universe. The observed low gas density ($n_{\rm gas} \sim 10^{-3}$ atoms/cm$^3$) and the extended not-variable X-ray emission of clusters, suggested the scenario of large amounts of fully ionized gas ($T \sim 10^7 - 10^8$ K) filling the intra-cluster medium (ICM) and losing energy by thermal bremsstrahlung processes, due to accelerated electrons in the Coulombian field of the ions in which they are mixed. It has been estimated that the 90% of the baryons is located in the hot plasma, while the remaining 10% forms stars in the galaxies and are held in a cold phase (Lin, Mohr, & Stanford 2003). Supporting the hypothesis of thermal emission, from 1976 were observed X-ray iron emission lines, due to thermal processes, in many of the most analyzed objects at that time, such as the Perseus, Coma and Virgo clusters (Sarazin 1986).

Since heavy elements are displaced throughout the intergalactic medium and then in the ICM by processes related to the stellar evolution (e.g., supernovae explosions), the high abundance ($Z \sim 0.3\,Z_\odot$) observed in clusters of galaxies could find an explanation in the context of hierarchical structure formation and in the most recent studies of the mixing induced by AGN outflows (e.g., McNamara & Nulsen 2007, and references therein).

In this chapter, we focus on the physics of the ICM, giving an overview about emission mechanisms at different wavelengths. This will be of support to the aim of this work: the comparison of cluster masses obtained through two different methods, weak gravitational lensing and X-rays. Useful publications about the topics here treated are: Sarazin (1986); Fabian (1994); Voit (2005); Allen et al. (2011); Schneider (2015).

## 3.1 Optical Appearance

Although the visible matter in galaxy clusters accounts for an extremely small fraction of the cluster components, it offers observables which are extremely useful for total mass estimates.

At optical wavelenghts galaxy cluster show up as stashes of galaxies with the number density of objects decreasing with radius from the center. The projected density distribution of cluster members is usually estimated through parametrized models which can be either physically or mathematically justified. However, the distribution of galaxies is dependent on the galaxy type (e.g., early-type galaxies are more abundant near the cluster center), thus the distribution of galaxies does not trace the total cluster matter.

Alternatively, through the spectroscopic analysis of the single cluster galaxies, the retrieved dynamical

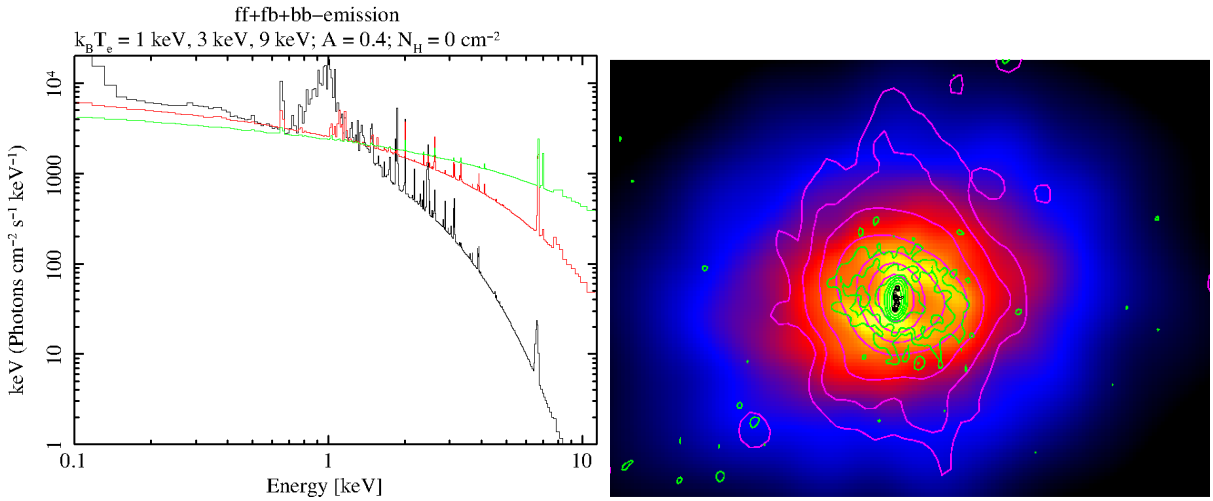


Figure 3.2: *Left panel:* X-ray spectra which include free-free, free-bound, and bound-bound emission types. The different colored lines indicate different cluster temperatures (black: 1 keV, red: 3 keV, green: 9 keV). Atomic transitions and recombination radiation features as lines above the bremsstrahlung emission, which is exponentially cut off at higher energies for higher temperatures. Credit: Reiprich et al. (2013). *Right panel:* Overlay of radio contours from the *Very Large Array* (*VLA*) on the *Chandra* X-ray image of the galaxy cluster RBS 797 (at redshift 0.35). Different colors indicate different radio frequencies and *VLA* interferometric configuration, showing a strong interplay between X-ray and low-frequency emission. Credit: Doria et al. (2012); Gitti et al. (2012).

information (i.e., the tridimensional velocity dispersion) combined with model assumptions from the velocity dispersion profiles and the projected number density of galaxies, yields *dynamical masses* of galaxy clusters. Despite this optical-dynamical method is insensitive to non-thermal pressure (e.g., magnetic fields, turbulence, cosmic ray pressure) the uncertainty in determining the cluster center, and the finite number of galaxies, allows to recover mass information with only ∼50% of accuracy (Rines & Diaferio 2006).

Finally, the most promising optical technique for cluster mass estimates is via weak gravitational lensing. As this is the core method used in this thesis, it will be discussed in the dedicated Chapter 4.

## 3.2 X-ray Emission

Since the satellite *Uhuru* became operative, it was found that the detected X-ray emission in galaxy clusters could not be traced back to compact sources. It was observed that the emission is too diffuse throughout the clumps of galactic objects, and it is not variable with time (Elvis 1976).

The gas of the ICM is close to hydrostatic equilibrium in the gravitational field of a virialized galaxy cluster, and can preserve this state only if its sound speed

$$c_\mathrm{s} = \sqrt{\gamma \frac{kT}{\mu m_\mathrm{p}}} \quad [\mathrm{km/s}] \tag{3.1}$$

is similar to the velocity dispersion of the cluster:

$$\frac{kT}{\mu m_\mathrm{p}} \approx \sigma_\mathrm{r}^2 \quad [\mathrm{km^2 s^{-2}}] \quad , \tag{3.2}$$

where $m_p$ is the proton mass and $\mu$ is the mean molecular weight (for solar abundances $\sim 0.6$). Here $\sigma_r$ is the line of sight velocity dispersion of galaxies in the cluster which assumes a value in the range from 300 to 1200 $\mathrm{kms}^{-1}$, giving temperatures of $10^7 - 10^8$ K.

Since the ICM is an hydrostatic self-supported atmosphere, the similarity of the sound speed of the gas with the typical velocity dispersion of the galaxy cluster is justified by the gravitational energy release (by accretion shocks and adiabatic compression) distributed equally between the ICM, as kinetic energy per unit mass, and galaxies (Fabian 1994).

The most important properties easily derivable from the X-ray spectrum of a cluster, are the temperature of the diffuse gas from line emission and the *emission integral*:

$$\epsilon = \int n_e \, n_p \, dV \tag{3.3}$$

where $n_e$ is the electron density, $n_p$ is the proton density, and $V$ is the volume of the gas in the galaxy cluster. In fact the relation

$$L_X \propto \epsilon \, T^{1/2} \tag{3.4}$$

indicates that the X-ray luminosity depends on emission integral and gas temperature.

### 3.2.1 Thermal Bremsstrahlung from Hot Plasma

High temperatures and low electron densities ($n_e \simeq 10^{-2} - 10^{-4}\,\mathrm{cm}^{-3}$) in a gas composed mainly by hydrogen and concentrated in the range of few Mpc, make it possible to assume the thermal bremsstrahlung radiation as the main mechanism producing X-ray emission in galaxy clusters.

Given a volume $dV$ in an emitting region with a section $d\Sigma$ perpendicular to our line of sight and a depth $\mathrm{d}l$ along the line of sight ($\mathrm{d}V = \mathrm{d}\Sigma\mathrm{d}l$), the monochromatic specific emissivity, $J(\nu)$, is the monochromatic luminosity per unit volume, so defined:

$$J(\nu) = \frac{L(\nu)}{\mathrm{d}V} \quad [\mathrm{erg\ s^{-1}\ Hz^{-1}\ cm^{-3}}] \quad . \tag{3.5}$$

The free-free process due to the collision between electrons and ions in thermal equilibrium in am ionized plasma (valid for $T \geq 3 \times 10^7$K), gives a specific emissivity at a frequency $\nu$:

$$J_{br}(\nu, T) = 6.8 \times 10^{-38}\, T^{-1/2} \mathrm{e}^{-h\nu/kT} n_e n_z Z^2 \, \overline{g_{ff}(T,\nu)} \quad [\mathrm{erg\ cm^{-3}\ s^{-1}\ Hz^{-1}}] \tag{3.6}$$

where $T$ is the temperature of the gas, $Z$ is the charge of the nuclei, $n_e$ and $n_z$ are the number density of electrons and ions respectively (Rybicki & Lightman 1979). The coefficient $\overline{g_{ff}(T,\nu)}$ depends on the electron energy and on the frequency of its radiation; it is called Gaunt factor and corrects for quantum mechanical effects and for the effect of distant collisions (Karzas & Latter 1961; Kellogg et al. 1975).

Integrating the specific emissivity on the whole spectrum, it is possible to obtain the total emissivity:

$$J_{br}(T) \propto T^{1/2} n_e^2 \quad . \tag{3.7}$$

Assuming that the ICM has roughly a single temperature, the emissivity tells us that the X-ray spectrum should be close to an exponential of the frequency. Defining the total emitted specific intensity as

$$I_\nu \propto \int n_e^2 T^{1/2} \mathrm{d}l \quad , \tag{3.8}$$

as a matter of fact, it has been observed that it follows the behavior

$$I_\nu \propto \mathrm{e}^{-\frac{h\nu}{kT}} \tag{3.9}$$

instead of the expected spectrum from an initially proposed (then discarded) inverse Compton mechanism, which would give a power-law trend,

$$I_\nu \propto \nu^{-\alpha} \quad , \tag{3.10}$$

but this process is not consistent with observations, therefore is in contrast with the detection of X-ray line emission.

The spectral lines emission is governed by bound-bound radiation. One of the most prominent lines is the ionized iron Fe-k$\alpha$ line, well visible in the spectra of Figure 3.2 (left panel) at ~7 keV. Line emission becomes important at lower temperatures $T \lesssim 2\,\mathrm{keV}$, as fewer elements of the ICM are fully ionized. In fact, ionized atoms (C, N, O, Ne, Mg, Si, S, Ar, Ca and the ~1 keV Fe complex) can dominate this range as stands out from the spectrum of the 1keV ICM temperature in the left panel of Figure 3.2.

### 3.2.2 Hydrostatic Modeling of the ICM

To obtain physical quantities from galaxy cluster radial profiles, it is used to fit the profiles to a hydrostatic-isothermal model (Cavaliere & Fusco-Femiano 1976). Jones & Forman (1984) used this model to describe the surface brightness profile of rich clusters. The hydrostatic isothermal model is based on the assumptions of: isothermal behavior of ICM and galaxies, hydrostatic equilibrium between these two component of the baryonic mass of the cluster, and the equilibrium of the galaxies with the total gravitational mass. If the distribution of the galaxies in the cluster core can be described by a self-gravitating simple isothermal sphere (SIS) model, such as the Emden sphere (Zwicky 1957) adopting the King (1962) approximation (it is considered that most of the mass lies in the core of the cluster), the X-ray surface brightness distribution can be characterized using the so called *$\beta$-profile*:

$$S(r) = S_0 \left[1 + \left(\frac{R}{r_\mathrm{c}}\right)^2\right]^{-3\beta+\frac{1}{2}} \tag{3.11}$$

where $r_\mathrm{c}$ is the core radius of the gas distribution, while $\beta$ is the ratio of the energy per unit mass in galaxies to the energy per unit mass in gas defined as follows:

$$\beta = \frac{\mu m_\mathrm{p} \sigma_\mathrm{r}^2}{kT} \tag{3.12}$$

with $k$ being the Boltzmann's constant and $T$ the X-ray gas temperature, while $\sigma_r$ is the cluster velocity dispersion so defined (Binney & Tremaine 1987):

$$\sigma_\mathrm{r}^2 = \frac{4\pi G \rho_0 r_\mathrm{c}^2}{9} \quad . \tag{3.13}$$

It has been estimated, for galaxies in clusters, a value of $\sigma_\mathrm{r} \approx 1000$ km/s.

The parameter $\beta$ is expected to be $\beta = 1$ for the considered isothermal sphere, as ICM and galaxies have the same kinetic energies (equal gas and galaxy distribution) in that model. However, since the difference between the two is that the ICM is a collisional fluid while galaxies are considered as non-collisional structures, we expect a decreasing $\beta$ (it is observed $\beta \lesssim 1$). Although most authors have estimated $\beta$ from surface brightness profiles, it can in principle be determined by directly measuring the velocity dispersion

of the cluster ($\sigma_r$) and the temperature of the gas.

However, the average value of the $\beta$ parameter determined by fits to the X-ray surface brightness of a large number of clusters was found by Jones & Forman (1984):

$$< \beta_{\rm fit} >= 0.65 \quad . \tag{3.14}$$

The surface brightness can be derived from the integration of the emissivity of the gas along the line of sight. Thus, we can easily find that also the gas density profile in a cluster of galaxies is well described by a $\beta$-model (Cavaliere & Fusco-Femiano 1976),

$$\rho_{\rm gas}(r) = \rho_{\rm gas,0} \left[ 1 + \left( \frac{R}{r_{\rm c}} \right)^2 \right]^{-\frac{3\beta}{2}} \quad , \tag{3.15}$$

where $r_c$ is the *core radius* which is helpful to avoid that the density grows to infinitely high values in the center and $\rho_{\rm gas,0}$ is the density at $r$=0. This model characterizes an isothermal gas in hydrostatic equilibrium within the potential associated with a King dark matter density profile. This model is a useful guideline for interpreting cluster emissivity in terms of physical properties.

Despite the ICM is not isothermal and does not follow a smooth spatial distribution, the $\beta$-model is a good approximation for the surface brightness profile with the exception for the central part. Usually adopting a double $\beta$-model, the central excess is well fitted as well.

### 3.2.3 Hydrostatic Mass Estimates

Cluster of galaxies mass measurements through their X-ray emission rely on the hydrostatic equilibrium assumption and on spherical symmetry. When X-ray observations of one object are deep enough to allow gas density and temperature (respectively $\rho_{\rm gas}(r)$ and $T_{\rm gas}(r)$) profile studies, it is possible to relate them to the cumulative mass within a certain radius $r$ by:

$$M(r) = -\frac{r\, kT_{\rm gas}(r)}{G\mu m_p} \left( \frac{{\rm d}\ \ln \rho_{\rm gas}(r)}{{\rm d}\ \ln r} + \frac{{\rm d}\ \ln T_{\rm gas}(r)}{{\rm d}\ \ln r} \right) \quad . \tag{3.16}$$

The hydrostatic equilibrium assumption breaks down when the ICM is perturbed by a major merger event or, especially in the inner regions of a clusters, when AGN feedback plays an important role. Furthermore, simulations have shown that normal dynamical events within the ICM, such as bulk motion, gas clumping and turbulence can invalidate the hydrostatic equilibrium inducing a bias at the tens of per cent level (e.g., Nagai et al. 2007; Simionescu et al. 2011; Rasia et al. 2012).

Equation (3.16) can be used to calculate the mass within any radius, however some values are usually taken for convention. Following the spherical collapse model (e.g., Amendola & Tsujikawa 2010, , see also Section 2.2.3), one can divide the relaxed, virialized area, from the outer region where the infall into the potential well of the cluster is still taking place. This is done by adopting a virial radius ($r_\Delta$) which corresponds to an overdensity $\Delta(z)$ w.r.t. the critical density of the universe ($\rho_{crit}$) at that time (or redshift), as expressed by:

$$\Delta(z) = \frac{3M(< r_\Delta)}{4\pi r_\Delta^3\, \rho_{\rm crit}(z)} \quad , \tag{3.17}$$

where typically $\Delta(z)$ = 2500, 1000, 500, for X-ray masses; while goes to larger radii, $\Delta(z)$ = 200 (shown by simulations to be very close to the true virial radius), in weak lensing mass reconstruction and in X-ray works based on *Suzaku* telescope observations (e.g., Reiprich et al. 2013).

## 3.3 Radio Emission

Even if galaxy clusters emit primarily in the X-ray band due to the bremsstrahlung radiation of the hot ionized plasma, they also have a significant emission in the radio band. Their radio emission gives an important contribution in the understanding of the physics within the cluster and of the interactions between the gas and the compact galaxies.

The radio emission in clusters of galaxies, for the most part, is referable to discrete sources, as galaxies are. But an important role is played also by radio sources, unrelated to individual galaxies, which show a diffuse large-scale emission: halos, relics and mini-halos (Section 3.3.1).

The non-thermal emission in clusters was studied for the first time by Mills (1960) and van den Bergh (1961) and it was found that many radio sources were located within a certain radius close to the center of the cluster. The synchrotron emission (Ginzburg & Syrovatskii 1965), due to electrons accelerated by the magnetic field, follows a power-law behavior over a wide range of frequencies $\nu$,

$$I_\nu \propto \nu^{-\alpha_\mathrm{r}} \,, \tag{3.18}$$

where $\alpha_\mathrm{r}$ is the radio spectral index which assumes the typical value $\alpha_r \approx 0.8$ for extragalactic radio sources.

Strong radio emission is primarily associated with cD galaxies (giant elliptical galaxies) which occur, in most cases, in the center of clusters. Moreover, cluster radio sources present a spectral index $\alpha_\mathrm{r} \gtrsim 1$, hence showing a steeper radio spectra than other radio sources. It has been found a connection between the steepness and the richness of the cluster (McHardy 1979; Roland et al. 1976). The steep spectrum of cluster radio source could find an explanation in the dynamical interaction between the ICM and the radio emitting relativistic electrons.

Since it has been observed that the main radio emission from galaxies is detected when streams or blobs of the relativistic non-thermal plasma are ejected from the nucleus of the galaxy (Miley 1980), the intra-cluster gas with its pressure forces, could confine the emitting plasma and prevent its adiabatic expansion. Thus, synchrotron losses become relevant, especially for high energy electrons, causing a steepening of the spectrum. The strong pressure force of the ICM could also explain the absence of very large radio galaxies in the inner radii of the clusters.

Recent studies are pointing out the interesting evidence of an interplay between the ICM and the AGNs hosted in the core of galaxy clusters, especially in those with cooling flows. This can have relevant importance in the understanding of the heating and cooling mechanisms of the intra-cluster gas and could lead to a solution of the cooling flow problem.

### 3.3.1 Diffuse Emission of the ICM

Large-scale diffuse radio emission presents a steep spectrum, with a typical spectral index $\alpha \approx 1.2 - 1.4$. It is also observed that the radio spectral index tends to become steeper in outer regions, and this steepening of the spectra is indicative of a spectral break at low frequencies (Pedlar et al. 1990; Giovannini et al. 1993).

Halos, mini-halos and relics are the three main type of diffuse radio sources in the ICM, not directly associated with galaxies (e.g., Feretti & Giovannini 2008).

**Radio Halos and Mini-Halos.** Giant radio halos have been observed in a good number of galaxy clusters, emitting by synchrotron radiation on scales of mega-parsec, with a power at 1.4 GHz: $P_{1.4\mathrm{GHz}} =$

$10^{23} - 10^{25}$ W/Hz. Radio halos have low surface brightness and for this reason are difficult to detect. In addition, it is also a complex work separating the diffuse emission from the embedded discrete radio sources. Halos have a regular morphology, similar to that observed in the X-ray band and since they have been found commonly in cluster mergers, their origin could be related to the particle re-acceleration occurring in-situ in turbulences and shocks introduced by these merging events (e.g., Ferrari et al. 2008 and references therein).

Mini-halos can be distinguished by halos, not only for their dimension (mini-halos extend on a moderate scale of $\sim 500$ kpc) but also because it is common to observe them in the surroundings of the central radio galaxy or in the center of cooling flows. They are not related to ongoing cluster merger activity. The evidence that mini-halos are mostly observed at the center of cool core clusters indicates that their origin and evolution can be related to the energy feedback from the cooling flow itself. In particular, Gitti et al. (2002) developed a model of particle acceleration driven by magneto-hydrodynamics turbulence, finding that the diffuse synchrotron emission of the radio mini-halos may be due to the re-acceleration of relativistic electrons via Fermi-like processes in the ICM. The role of the cooling flow is to provide the necessary energetics to support these processes. If any re-acceleration or injection of relativistic electrons in strong magnetic fields were not present, it would be not possible to observe such radio diffuse structures, owing to the short lifetime of the emission.

**Radio Relics.** Relics are observed in the cluster periphery and can assume different morphologies, but more commonly they are structures perpendicular to the cluster radius. Those features are characterized by a strong polarization of their radio emission. They are unrelated to member galaxies, hence, as radio halos, relics could have originated by cluster mergers. Relics could be the remnant of recent merger events, strictly tied to the shock front as the relativistic particles have a short lifetime in a magnetic field enhanced from the compression by the shock of the thermal gas (Ensslin et al. 1998).

## 3.4 Sunyaev-Zel'dovich Effect

When cosmic microwave background photons penetrate the hot plasma of clusters of galaxies, they are scattered up towards higher energies via inverse Compton scattering. The energetic ICM electrons are subject to a decrease in energy to the advantage of the CMB photons, which then are up shifted at higher energies. As illustrated in Figure 3.3, the unique spectral signature of the SZ effect consists in a decrease of the intensity below $\sim 218$ GHz and an opposite trend at higher frequencies. This effect is known as the Sunyaev-Zel'dovich effect (SZE), as it has been proposed by Sunyaev & Zel'dovich (1970), and it has been observed for the first time few years later by Birkinshaw et al. (1978). Its effects are measurable in the microwave wavelengths and can be expressed in terms of CMB temperature change for a cloud with electron pressure $p_e$:

$$\frac{\Delta T_{\rm SZ}}{T_{\rm CMB}} = -2 \int \frac{p_{\rm e}\, \sigma_{\rm T}}{m_{\rm e} c^2}\, {\rm d}l = -2 \int \frac{n_{\rm e}\, kT_{\rm e}}{m_{\rm e} c^2}\, \sigma_{\rm T}\, {\rm d}l = -2y \tag{3.19}$$

where $\mathrm{d}l = c\mathrm{d}t$ is the length of a photon path through the cloud and $\sigma_T = 8\pi \mathrm{e}^4/(3m_{\rm e}^2 c^4)$ is the Thomson cross-section. $y$ is the Compton-$y$ parameter which, integrated over the solid angle ($\mathrm{d}\Omega = \mathrm{d}A\, D_{\rm A}^2$) of a cluster, provides a measure of its total thermal energy:

$$Y_{\rm SZ} = \int y\, {\rm d}\Omega \quad . \tag{3.20}$$

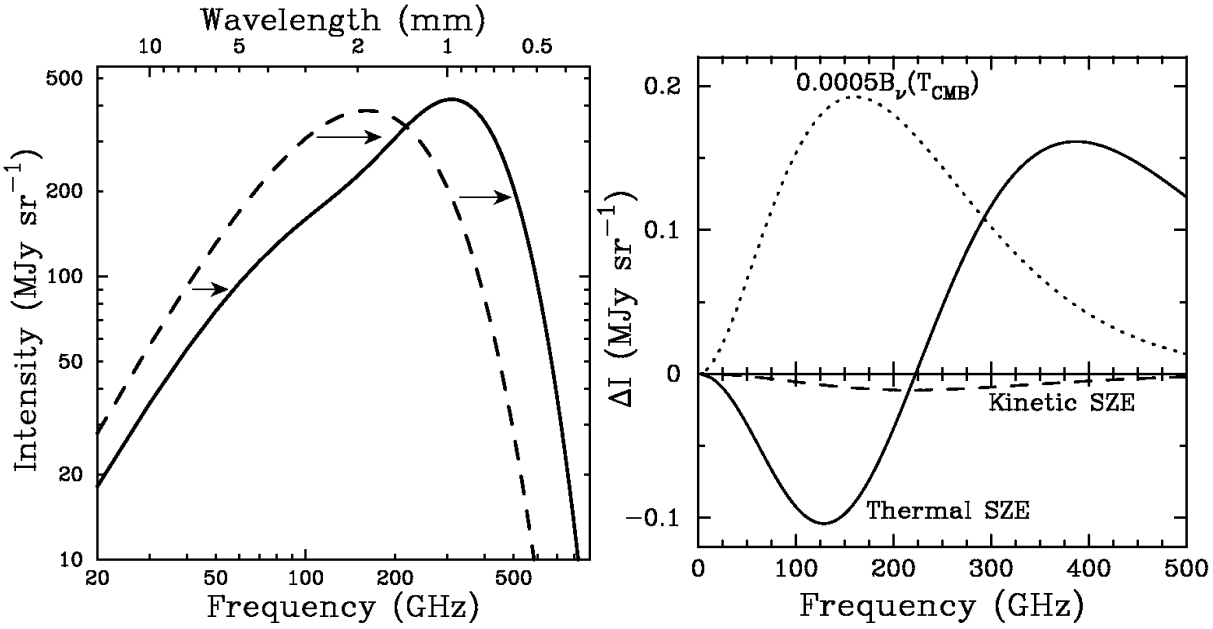


Figure 3.3: *Left panel:* The CMB black-body spectrum (dashed line) is affected by the inverse Compton scattering (solid line) which upscatters the photons at high frequencies. *Right panel:* Spectral distortion (magnified for illustration purposes) on the intensity of the cosmic microwave background radiation due to the Sunyaev-Zel'dovich effect. Both the thermal SZE (solid line) and the kinetic SZE (dashed line) are shown for a cluster at temperature $kT = 10\,\mathrm{keV}$, Compton $y$ parameter of $10^{-4}$, and a peculiar velocity of 500km/s. The dotted points indicate, for reference, the thermal spectrum of the CMB, scaled by a factor of 0.0005. Figures from Carlstrom et al. (2002).

Because of its linear dependence (in contrast with the quadratic dependence of the X-ray emission, equation (3.3)), the SZ effect allows a different, less biased, approach on the cluster ICM density, being thus independent of the spatial distribution of the gas.

Moreover, as its signal is independent of redshift, it allows to push cluster detections to higher distances with the only limiting factor being the spatial resolution. As an example, many new clusters have been found thanks to the Atacama Cosmology Telescope (*ACT*), the *Planck* mission and the *South Pole Telescope* (*SPT*) (e.g., Menanteau et al. 2010; Planck Collaboration et al. 2011; Bleem et al. 2015).

## 3.5 Clusters in $\gamma$-rays

The study of galaxy clusters in Gamma-rays is a very young field of research. Predictions on $\gamma$-ray emission (through $\pi^\circ$ decay) has been proposed by simulations (e.g., Pinzke & Pfrommer 2010) and during the last decade many $\gamma$-ray telescopes saw their first light, starting the investigation both on the "low"- and the high-energy regimes (GeV and TeV ranges, respectively). Recent findings of the $\gamma$-ray satellite *Fermi - Large Area Telescope*, show an hint of a double-peak excess above the diffuse power-law background at energies of 110 GeV and 130 GeV (Hektor et al. 2013). This is the first time a boost factor due to dark matter annihilation has been measured. However, to improve the significance of this finding, more data and further analysis are needed. However, the debate is still ongoing as Liang et al. (2016), using a sample of 16 clusters, retract any evidence of spectral excess signal in the $\sim 110 - 130\,\mathrm{GeV}$ energy range.

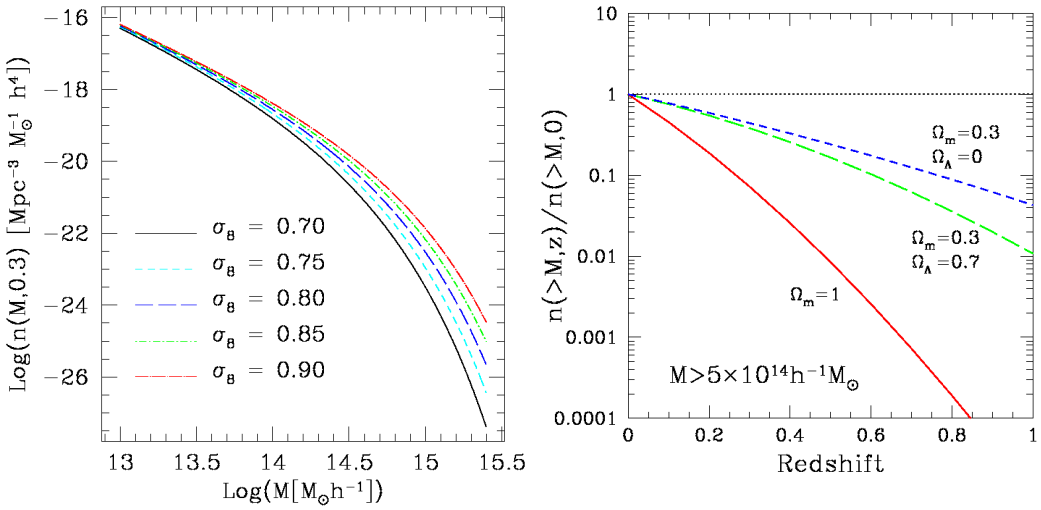


Figure 3.4: *Left:* Behavior of the halo mass function with different values of $\sigma_8$ at $z = 0$. The high mass clusters are more likely in a universe with a larger amplitude of the primordial density fluctuations. Figure from: Fedeli et al. (2008). *Right:* Adopting different cosmologies drastically changes the evolution of the cluster mass function. Here are shown two low-density universes, one accounting for dark energy (green dashed line) and one without it (blue short-dashed line), together with the Einstein-de Sitter universe (red line). The latter case shows the fastest evolution, as $\Omega_m = 1$ ($\sigma_8 = 0.5$). While for the two low-density cases ($\sigma_8 = 0.5$ was used) the evolution is slower, especially for the non-ΛCDM one. Figure from: Rosati et al. (2002).

## 3.6 Galaxy Clusters as Cosmological Tool

### 3.6.1 Non-linear Structure Formation

Galaxy clusters have the big advantage of being relatively simple objects to study. Firstly, because their evolution and physics and their spatial distribution are governed by a well known force: gravity. Secondly, because they are easy to observe at different frequencies, which unveil different properties, as shown in the previous sections of this Chapter. Finally, all those various information can be combined together in order to investigate not only the physics of their hot gas, but also the so-called "*dark sector*", that is the properties of dark matter and dark energy. Furthermore, cluster properties bring the signatures of dark energy influence, as their formation and evolution time covers the time range in which the effect of dark energy were more relevant.

The different cosmological probes touched upon in Chapter 2 are affiliated under two main categories: geometrical tests and growth of structure tests. The former focus on measuring distances and volumes, while the latter studies the large scale structure. Cluster cosmology has the privilege to play an important role in both branches. Galaxy cluster spatial clustering and cluster abundance trace the evolution of structures (with the latter method being sensitive also to the geometry); while studies of the gas mass fraction and estimates of the angular diameter distance, combining complementary observables, test the geometry of the universe (see Allen et al. 2011, and references therein).

The halo mass function (equation (2.40)) is of extraordinary importance as it has a strong dependence on cosmological parameters and can be tested at its massive end by galaxy clusters. Counting the number of galaxy clusters in bins of mass and redshift is useful to constrain $\Omega_m$, $\sigma_8$ and $\Omega_\Lambda$. In addition, galaxy

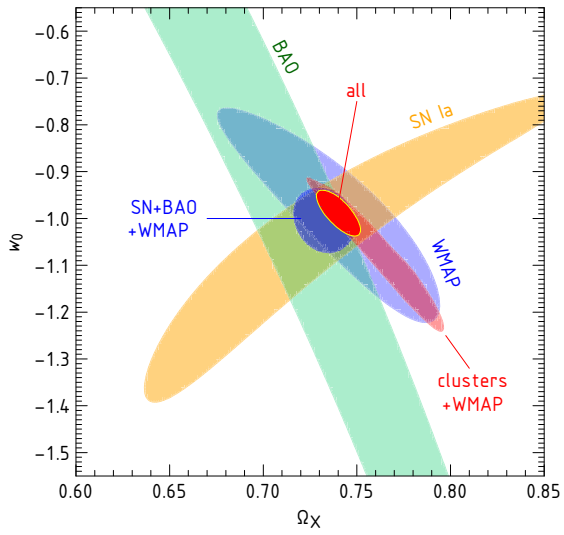


Figure 3.5: Overlap of the 68.3% credibility regions for the estimate of the cosmological parameters $\Omega_X = 1 - \Omega_m = \Omega_\Lambda$ and $w_0$ combining many cosmological datasets. The cluster results has been obtained by Vikhlinin et al. (2009b) by means of the *400d Cosmological Sample*, which we study via weak lensing observations in this work. The full red area is the result of combining all probes, including the cluster mass function. Different methods are complementary in order to explore different parts of the $\Omega_\Lambda - w_0$ plane. The joint credibility regions show that galaxy cluster cosmology does have a significant impact, significantly shrinking the allowed confidence region with respect to the joint SN+BAO+WMAP area. Credit: Vikhlinin et al. (2009b).

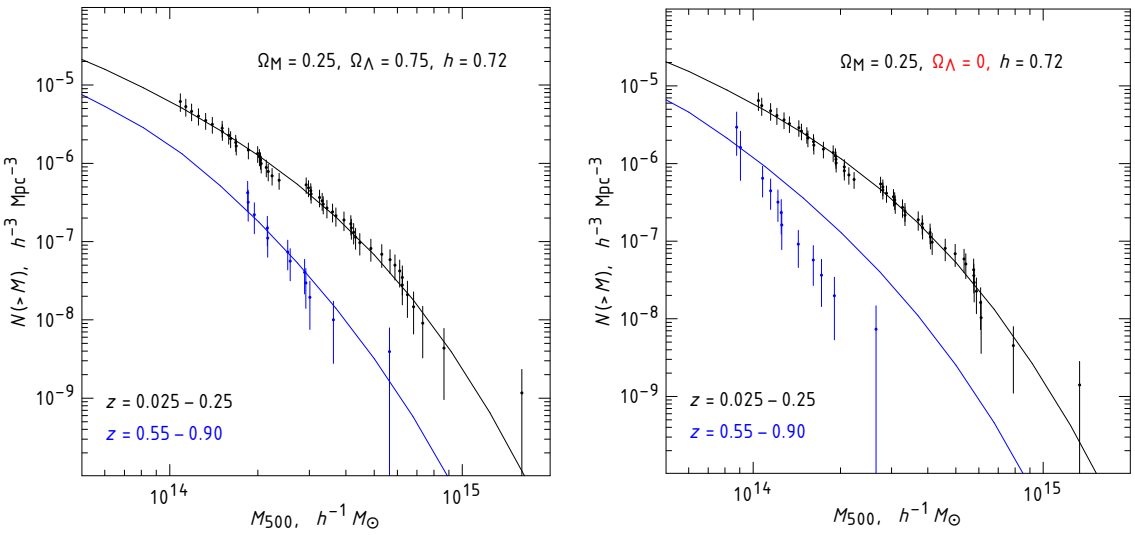


Figure 3.6: Cluster mass functions obtained by the X-ray study of the *400d* cluster sample. Here the sample is split in two redshift regimes, while all masses are calculated using the $Y_X$ proxy (discussed in Section 3.6.2). This shows how galaxy clusters are affected by a two-level of sensitivity to the cosmology: both the predicted theoretical model (lines) and the observational data (points) move because of their strong dependence on the cosmology. The bigger discrepancy is noticed in the high-redshift sample, where dark energy is more influential. Credit: Vikhlinin et al. (2009b).

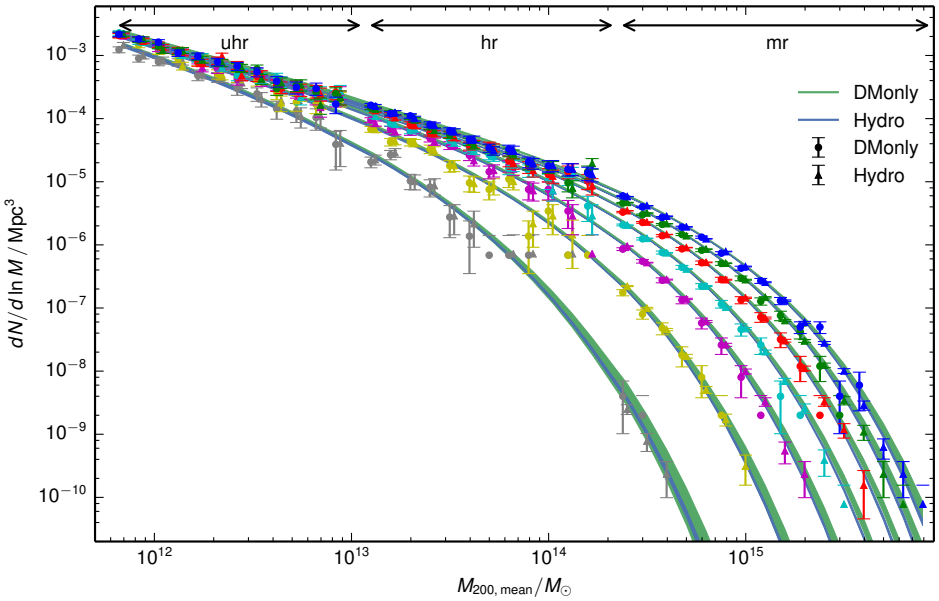


Figure 3.7: *Left:* Halo mass function at different redshifts ($z$=0, 0.13, 0.3, 0.5, 0.8, 1.2, 2) from simulations. The cut-off moves at larger masses for lower redshifts. Credit: Bocquet et al. (2016).

clusters are a fundamental tool for measuring the rate of structure formation via the comparison between today's cluster mass distribution with mass distribution at earlier times. This can be done by studying cluster samples at different redshifts and provides information on the $w$-parameter of the dark energy equation of state (Section 2.1.3). Galaxy clusters study yields constraints on cosmological models, investigating the parameter space in a complementary way w.r.t. various other methods (e.g., Voit 2005; Vikhlinin et al. 2009b; Allen et al. 2011; Schneider 2015; Mantz et al. 2015).

The exponential tail of the cluster mass function is extremely sensitive to cosmology. Its cut-off varies strongly with different cosmologies, which also define the speed of the evolution of collapsed structures. The right panel of Figure 3.4 shows that for a flat universe the evolution is faster than in a low-density universe. Furthermore it also proves that dark energy makes an impact on the mass function. This is easiest to see when comparing mass functions of cluster samples at different redshifts as done by Vikhlinin et al. (2009b) (Figure 3.6). The structure formation had to be faster than in the local universe in order to be seen as they are today (Borgani & Guzzo 2001). Additionally, for a precise cosmological use of the cluster mass function, it is important to capture the variation with redshift (as shown by simulations, Figure 3.7), investigating larger samples at different high-redshift ranges. Using the constraining power of the cluster mass function alone, one reaches a precision at a similar level of the gas mass fraction geometrical test (Allen et al. (2008), Section 3.6.2).

The first approach to the cluster mass function (more precisely they measured the temperature function) has been done by Henry & Arnaud (1991). Subsequently, Reiprich & Böhringer (2002) studied a X-ray flux limited sample (*HIFLUGCS*) which was more than double in size. The joint use of galaxy clusters in a complementary way to CMB, SNIa, galaxy clustering and lensing, has been made by Vikhlinin et al. (2009b) (Figure 3.6 & 3.5), which also studied the evolution of the mass function. They showed that the combination of different probes including galaxy clusters, which are characterized by systematics and degeneracies different from those of other methods, increases the precision on cosmological parameter

estimates Recent progress has been made by Mantz et al. (2010a, 2015), which stress the importance to apply a simultaneous fit to the cosmology and scaling relations.

### 3.6.2 Scaling Relations

When studying large samples of galaxy clusters for cosmological purposes (e.g., cluster mass function, large-scale structure), it is common praxis to link cluster masses with observables. The X-ray properties of clusters provide the most important observables, as through X-ray observations one can construct a complete, homogeneous and flux-limited sample, very useful for accurate cosmological parameter estimates. However, the assumptions needed for calculating X-ray masses (hydrostatic equilibrium and spherical symmetry, see Section 3.2.3) can be too simplistic, introducing biases which need to be cross-calibrated with other mass estimate methods which suffer from different systematics (e.g., Giodini et al. 2013, for a review).

With the forthcoming X-ray missions,*eROSITA* (Predehl et al. 2010; Merloni et al. 2012) and *Athena* (Nandra et al. 2013; Pointecouteau et al. 2013), tens of thousands of new galaxy clusters will be detected, spanning from the local universe to high redshifts and reaching low X-ray fluxes. In particular, *eROSITA*, the German-Russian mission which will carry out eight all-sky surveys in four years, will give with unprecedented depth a census of the universe reaching clusters and groups at $z > 1$ also probing the low mass cluster regime (Pillepich et al. 2012; Borm et al. 2014).

Therefore, in order to improve cosmological constraints analyzing such big samples with low quality data, the use of scaling relations is a more feasible approach, preferred over the calculation of hydrostatic masses. Hence, it is of crucial importance to use well-calibrated scaling laws which relate the true mass with "cheaper" (in terms of observation time) observables which can be obtained also with short exposures of the instrument or in case of bad quality data.

#### Self-Similarity

Adopting the approximation that *(i)* clusters form via a single gravitational collapse at a given redshift, and *(ii)* the only source of energy in the cluster gas comes from gravity, we can predict simple power law relations between the different observational properties of galaxy clusters (e.g., Borgani & Kravtsov 2011, for a review). As it is assumed that only gravity interacts with galaxy clusters during their formation, Kaiser (1986) proposed a *self-similar* model for their properties and evolution. This means that clusters are scaled versions of each other. Furthermore, they are self-similar with redshift: when they form, clusters reflect the density of the universe at that time. Hence, after being normalized by the same radius and mass, they all have the same properties.

The precision cosmological parameters are constrained with, depends on how precisely an observable can be estimated. This reflects onto the uncertainty in cluster cosmology as they are driven by the scatter in scaling relations. The cause of this scatter can be attributed to the failure of the assumptions adopted for the use of self-similarity. Furthermore, for high redshift samples, such as the *400d Cosmological Sample* studied in this work, one has to consider the evolution in those scalings as it affects both the mapping of the observable onto the cluster mass, and the number density inferred from clusters at a given mass from a survey based on the considered observable (Voit 2005).

Because of cosmic expansion, the critical density is higher at high redshift, and according to the hierarchical scenario of structure formation, the gravitational collapse of a halo happens when the matter

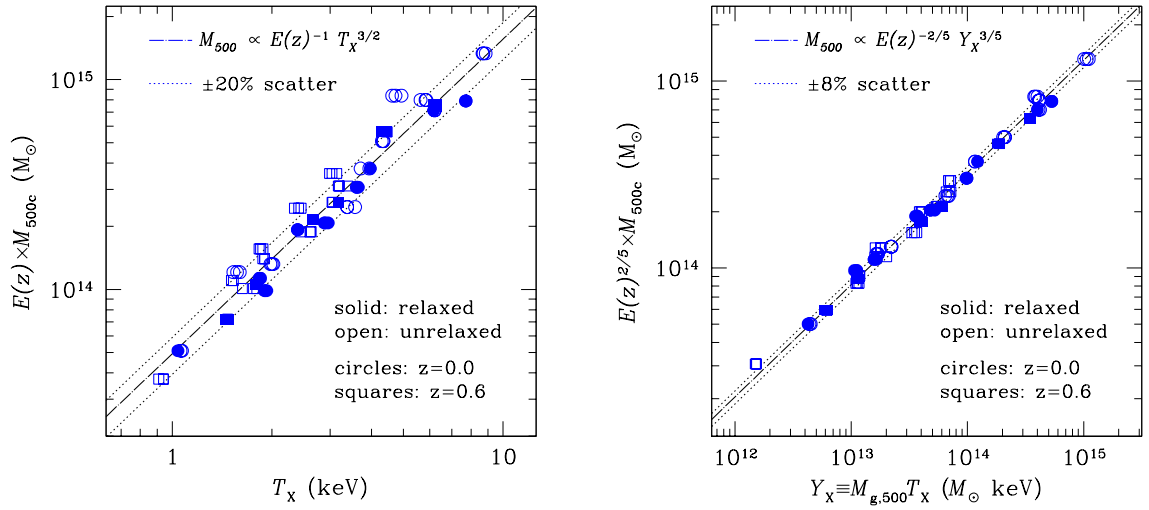


Figure 3.8: Mass-temperature (*left panel*) and $Y_X$–$M$ (*right panel*) relations investigated via simulations. The $M$–$T$ scaling law is more affected by the presence of unrelaxed clusters, while the $Y_X$–$M$ relation appears to be unaffected by it. Figures from Kravtsov et al. (2006).

overdensity overcomes the critical density at that redshift. Applying the redshift evolution factor (equation (2.15)), scaling relations are corrected for the redshift dependence.

### $M$–$T_X$ Relation

The *mass-temperature* scaling relation derivation relies on the self-similarity and on the virial theorem:

$$2K = -U \tag{3.21}$$

where $K$ and $U$ are the kinetic and potential energy, respectively. Adopting the assumption that clusters are made by a monoatomic gas, we can rewrite the virial equilibrium as:

$$M_\Delta kT \propto M_\Delta^2 R_\Delta^{-1} \quad . \tag{3.22}$$

From the total cluster mass (inverting equation (3.17)), making explicit $\rho \propto \Delta E(z)^2$ and substituting $R_\Delta \propto \Delta^{-1/3} M_\Delta^{1/3} E(z)^{-2/3}$ in equation (3.22), one obtains the final relation:

$$M_\Delta \propto (kT)^{3/2} \Delta^{-1/2} E(z)^{-1} \quad . \tag{3.23}$$

The X-ray temperature ($T_X$) is estimated from a single temperature fit to the cluster spectrum up to the chosen overdensity radius. The $M$–$T_X$ scaling law implies that for fixed mass, temperatures are higher the higher is the redshift of the galaxy clusters. This appears straightforward, given that the collapse onto galaxy clusters happened when the universe was more dense.

Using simulations, Kravtsov et al. (2006) showed that despite mass and temperature have a tight correlation, unrelaxed clusters add 20% scatter to the $M$–$T$ scaling law (left panel of Figure 3.8).

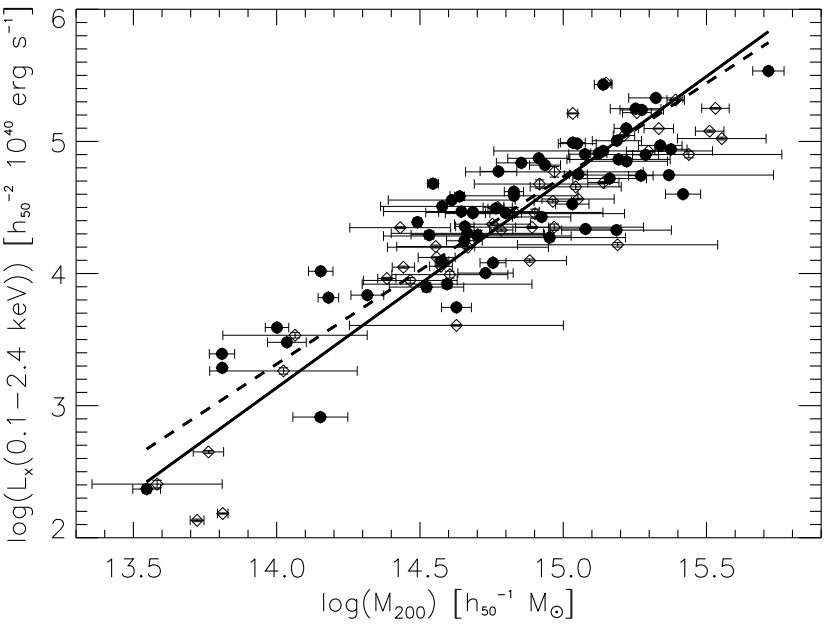


Figure 3.9: Luminosity-mass relation obtained for the *HIFLUGCS* sample, composed by 63 low redshift galaxy clusters. The solid line indicates the scaling relation for the extended sample of 106 objects, while the dashed line shows the relation for the *HIFLUGCS* clusters (plotted as filled circles). Credit: Reiprich & Böhringer (2002).

### $L_X$–$M$ Relation

The easiest to measure observable is the X-ray luminosity ($L_X$) which can be handily used for predicting the mass of clusters (Reiprich & Böhringer 2002). $L_X$ is specially optimal for large distant surveys which include faint objects. It can be used for pushing to high redshifts cosmological studies with clusters of galaxies.

As the bremsstrahlung emission tells us that the X-ray luminosity depends on the square of the gas density (equations (3.3) and (3.4)), we can rewrite equation (3.4) as:

$$L_X \propto \rho^2 (kT)^{1/2} R_\Delta^3 \tag{3.24}$$

and plugging in the $M$–$T_X$ relation (equation (3.23)), gives the *X-ray luminosity-mass* scaling relation:

$$L_X \propto M_\Delta^{4/3} \Delta^{7/6} E(z)^{7/3} \quad . \tag{3.25}$$

This tells us, as expected ($L_X \propto \rho^2$), that galaxy clusters of the same mass are more X-ray luminous at high redshift.

### $M_{gas}$–$M$ Relation

This is another low scatter proxy which works well within the assumptions that ICM and dark matter follow an identical distribution and that clusters contain exactly the cosmic mix of baryonic and nonbaryonic

matter (Voevodkin & Vikhlinin 2004). Hence, the *gas mass fraction* can be defined:

$$f_{\rm g} = \frac{M_{\rm gas}}{M_\Delta} \approx \frac{\Omega_{\rm b}}{\Omega_{\rm m}} \approx \frac{1}{6} \quad , \tag{3.26}$$

which has the advantage of being quite stable in a cluster population, being independent from redshift.

As $M_\Delta = f_{\rm g}^{-1} M_{\rm gas}$, where the gas mass is derived from the X-ray image, the total mass can be estimated using equation (3.17).

It is worth to notice that assuming that clusters of galaxies preserve the baryon and total matter quantities of the whole universe (equation (3.26)), it is possible to constrain $\Omega_{\rm m}$ (Allen et al. 2008). Despite the fact that the stellar mass contribution is also included in the calculations, it has been shown that the baryon fraction estimated with this method is lower than the cosmic average probed via CMB observations (LaRoque et al. 2006; Zhang et al. 2011).

### $Y_{\rm X}$–$M$ Relation

Kravtsov et al. (2006) proposed the $Y_{\rm X}$ parameter, the product between the gas temperature and the gas mass:

$$Y_{\rm X} = T_{\rm X} M_{\rm gas} \tag{3.27}$$

as the most precise mass proxy, having just 8% scatter in the correlation with the total cluster mass, without any further complications induced by the dynamical state of the cluster (see right panel of Figure 3.8).

$Y_X$ approximates at the same time the total thermal energy of the ICM and the integrated low-frequency SZ flux (see equation (3.20), also Nagai et al. (2007)). In this case, both $T_{\rm X}$ and $M_{\rm gas}$ come from the X-ray spectral analysis and assuming self-similarity, the relation between the cluster mass and the $Y_{\rm X}$ parameter is:

$$M_\Delta \propto Y_{\rm X}^{3/5} E(z)^{-2/5} \tag{3.28}$$

as a consequence of the expected evolution in the mass-temperature relation.

### Breaking Self-Similarity

Observed scaling relations deviate from the theoretical laws (e.g., Reiprich & Böhringer 2002; Maughan 2007; Pratt et al. 2009; Vikhlinin et al. 2009a; Reichert et al. 2011; Mantz et al. 2016). Self-similarity can be broken by non-gravitational processes, merging events, heating and cooling of the ICM and presence of substructures. Furthermore, all scaling relations use the assumption that all properties are constant ($T$, $\rho$, etc.).

More in detail, radiative cooling in cluster cores requests clusters to be brighter and cooler. The scatter introduced by this problem is usually reduced by considering core-excised luminosities and temperatures. On the other hand, the interplay between the central AGN and the ICM, especially for lower mass clusters, heats the cluster temperature (e.g., Croston et al. 2005).

In addition, the assumption of having a single gravitational collapse is contradicted by the fact that cluster formation is rather governed by hierarchical merging events in which smaller systems join together to create a more massive structure (Rowley et al. 2004).

A better understanding on how those caveats affect scaling relations needs to be addressed by more realistic simulations which take into account AGN activity, merging history and heating and cooling

processes of the ICM. Also, there is a strong need of tests on the evolution of the mass scaling relations, which will bring the benefit of a better understanding of the evolution of the mass function.

In this thesis we will focus on the calibration of the scaling relations using cluster masses obtained through the weak lensing technique. In particular, we will compare with the results from Vikhlinin et al. (2009a), as our optically followed-up high-redshift subsample is drawn from their original sample: the *400d* Survey. The self-similar prediction provides a well-justified, simple parameterization for the scaling relations and their redshift evolution. Also, it allows to test a good number of underlying cosmologies. Vikhlinin et al. (2009a) assume a self-similar evolution for the $Y_X$–$M$ relation, which is the proxy they use for estimating cluster masses. Kravtsov et al. (2006) found that the $Y_X$–$M$ scaling law truly has a redshift evolution which is close to the self-similar prediction. This might be due to the fact that since the $Y_X$ estimator is directly linked to the thermal energy (as its SZ equivalent), it is also related to the depth of the cluster potential well. Furthermore, the two factors that contribute to $Y_X$ in equation (3.27), show an anticorrelated evolution. In this thesis the self-similar evolution of scaling relations is verified empirically.

CHAPTER 4

# Weak Gravitational Lensing

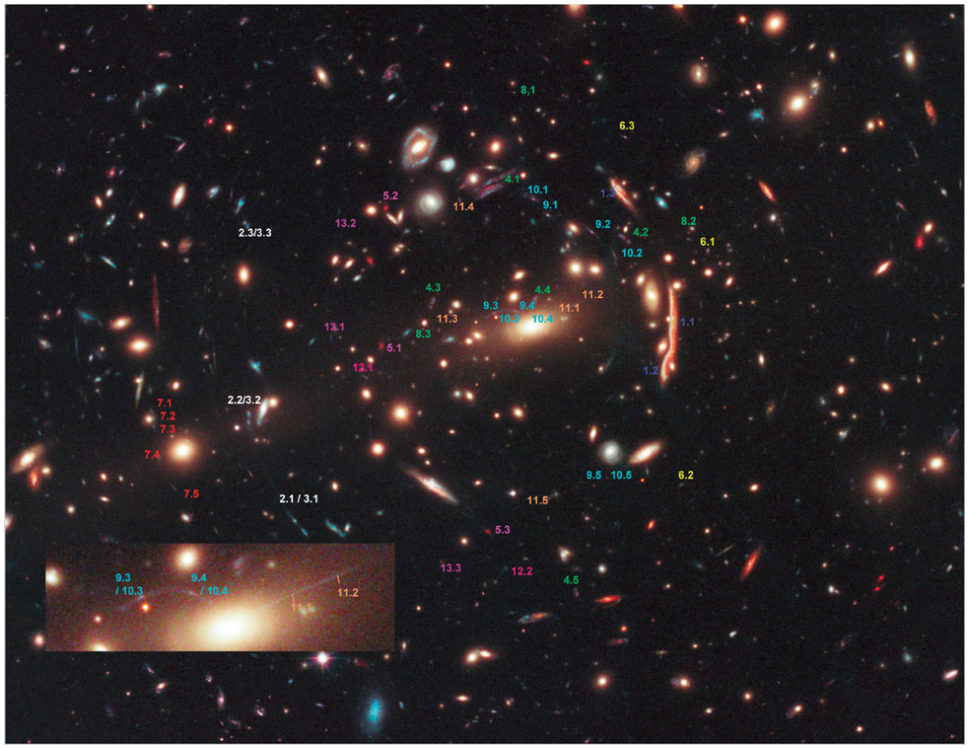


Figure 4.1: A spectacular view of the cluster of galaxies MACS J1206.2−0848 ($z = 0.44$) as seen by the *Hubble Space Telescope*. The numbers outline 47 multiple images coming from at least 12 background sources in total. Credit: Zitrin et al. (2012).

In Chapter 2, has been shown that gravity plays a crucial role in the growth of structures of our Universe. General relativity predicts that massive conglomerates of matter can bend the light of a background source. The image of this source is then distorted and magnified by the intervening mass, which acts like a lens. This effect is known as *gravitational lensing* and it is independent from the type of matter which composes the lens (e.g. baryonic or dark matter). Hence, being insensitive to the dynamical state of the lens, this method can be used for the direct unbiased measure of its gravitational tidal field.

As will be shown in the following sections, gravitational lensing is commonly subdivided into two distinguished regimes, *weak gravitational lensing* and *strong gravitational lensing*, depending on the

projected distance between the source and the lens. The former, statistically accounts for the small distortions of a large sample of background galaxies. The latter, yielding eye-catching features such as multiple or arc-shaped images, is more noticeable. While Figure 4.1 represents a striking example of strong gravitational lensing by a massive galaxy cluster, the subtle weak lensing effect cannot be glimpsed by eye. Nevertheless, it is used as a robust estimator of the mass distribution of galaxy clusters out to large radii.

Moreover, gravitational lensing is a powerful tool for the study of the large-scale structure as well; through galaxy-galaxy lensing and cosmic shear.

In this Chapter, after a short introduction to the general concept of gravitational lensing (Section 4.1), it will be given more focus on the weak lensing regime and its application to galaxy cluster mass estimates. An overview on technical details about the methods used in this work is given in Section 4.2. A more detailed treatment of the gravitational lensing theory is given in Bartelmann & Schneider (2001), Schneider (2006) and Hoekstra (2013).

## 4.1 Basic Formalism of Gravitational Lensing

The Einstein equation (2.1) tells us that light rays follow null geodesics ($ds^2 = 0$ in equation (2.2)) which depend on the matter distribution. In other words, light can be deflected by the presence of a gravitational potential. To calculate how light propagates in a universe filled with structures of various scales (as seen in Section 2.2) is a hard task using general relativity.

### 4.1.1 Lensing Geometry

The typical geometry of lensing is sketched in Figure 4.2, where the light originated from a source at $\vec{\eta}$ is deflected with a *deflection angle* $\vec{\hat{\alpha}}$ by the lens gravitational potential. The distortion depends on the intervening mass distribution and on the *impact parameter* $\vec{\xi}$. The simple model adopted in this description assumes a weak gravitational field ($\Phi/c^2 \ll 1$) and small deflection angles. Thus, it is possible to use the *thin lens* approximation: the deflection happens on the lens plane, where the lens is characterized by a thickness much smaller that the angular diameter distances (as defined in equation (2.21)) between source, lens and observer ($D_\mathrm{s}$, $D_\mathrm{ds}$, $D_\mathrm{d}$). Also, the lens is assumed to be static, as its peculiar velocity is much smaller than the light crossing time.

The true unlensed position of the source is $\vec{\beta} = \vec{\eta}/D_\mathrm{s}$, but its image appears at the position $\vec{\theta} = \vec{\xi}/D_\mathrm{ds}$. These two celestial positions differ only by the deflection angle:

$$\vec{\beta} = \vec{\theta} - \frac{D_\mathrm{ds}}{D_\mathrm{s}}\vec{\hat{\alpha}}(D_\mathrm{d}\vec{\theta}) \quad , \tag{4.1}$$

or with introduction of the *reduced deflection angle* $\vec{\alpha} := \frac{D_\mathrm{ds}}{D_\mathrm{s}}\vec{\hat{\alpha}}(D_\mathrm{d}\vec{\theta})$, becomes

$$\vec{\beta} = \vec{\theta} - \vec{\alpha}(\vec{\theta}) \quad , \tag{4.2}$$

called the *lens equation*.

The deflection angle carries a central information for lensing measurements: the ratio $D_\mathrm{ds}/D_\mathrm{s}$. Considering the simple case of the light being bended by a point mass $M$, and additionally assuming that the impact parameter $\vec{\xi}$ is much larger than the Schwarzschild radius of the lens ($\vec{\xi} \gg 2GM/c^2$), the

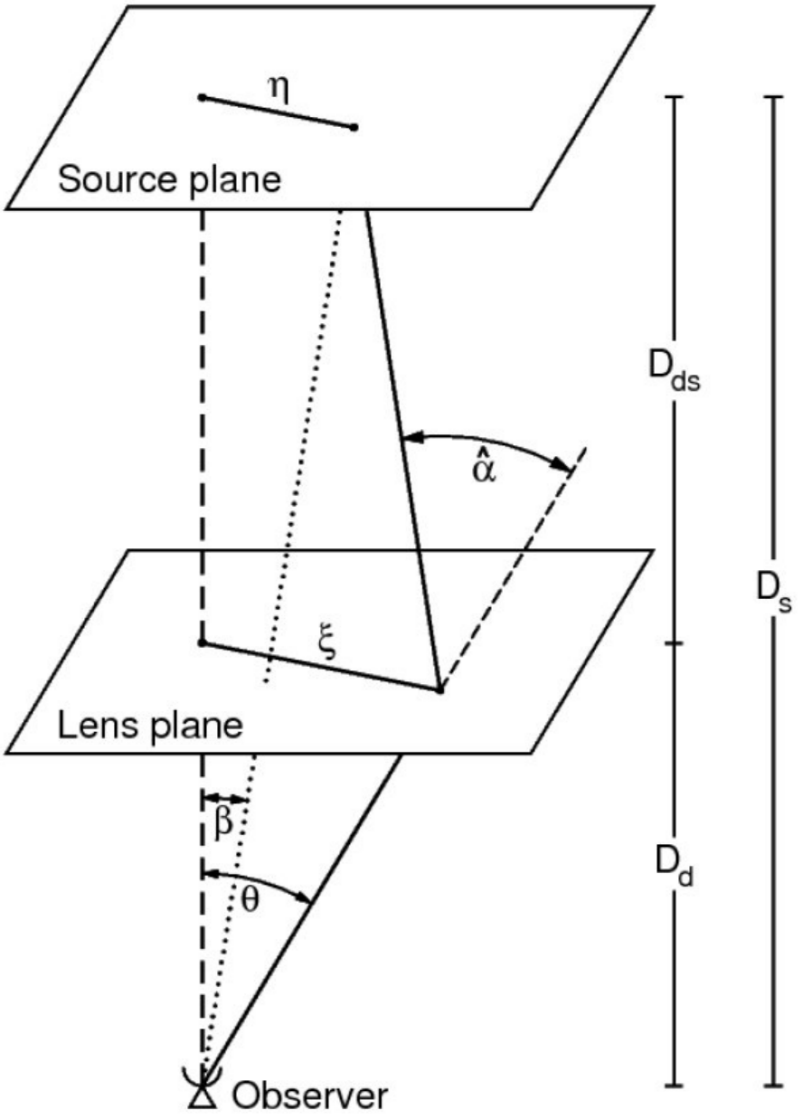


Figure 4.2: Typical gravitational lensing geometry, adopting the thin lens approximation. A source at an angular diameter distance $D_s$ emits light which passes through the plane where the lens is situated, at distance $D_d$. The distance between source and lens plans is $D_{ds}$. The observer is connected to the center of the mass distribution of the lens through an optical axis, perpendicular to both lens and source planes. The intersections between the optical axis and the two planes are the origin of the coordinate system. The perpendicular distance of the source position from the optical axis is indicated by $\vec{\eta}$. In absence of a deflector, the source would be seen with at the angular position $\beta$. Due to lensing, the light coming from this point is deflected by the gravitational field of the lens and it is seen by the observer on the lens plane at a distance $\vec{\xi}$ and at the angular position $\theta$. The light path is deflected by an angle $\hat{\alpha}$. Credit: Schneider (2006).

expression

$$\vec{\tilde{\alpha}} = \frac{4GM}{c^2\xi} \tag{4.3}$$

can be derived for the deflection angle from general relativity. The deflection angle can also be determined for a three-dimensional matter distribution $\rho(\vec{\xi}, r_3)$, as the superposition of the deflection angles of the individual mass elements ($\mathrm{d}m(r) = \rho(r)\mathrm{d}V$) of the extended lens:

$$\vec{\tilde{\alpha}}(\vec{\xi}) = \frac{4G}{c^2} \int \Sigma(\vec{\xi'}) \frac{\vec{\xi} - \vec{\xi'}}{|\vec{\xi} - \vec{\xi'}|^2} \, \mathrm{d}\vec{\xi'} \quad . \tag{4.4}$$

The *surface mass density* has been defined as:

$$\Sigma(\vec{\xi}) = \int \rho(\vec{\xi'}, r_3) \, \mathrm{d}r_3 \quad , \tag{4.5}$$

and represents the projection of the three-dimensional mass on the plane perpendicular to the line of sight, where we choose the coordinate system such that the line of sight to the lens is in the $r_3$ direction. One can also define a *critical surface density*

$$\Sigma_{\mathrm{crit}} = \frac{c^2}{4\pi G} \frac{D_{\mathrm{s}}}{D_{\mathrm{d}} D_{\mathrm{ds}}} \tag{4.6}$$

and the adimensional surface mass density, called *convergence*:

$$\kappa(\vec{\theta}) = \frac{\Sigma(D_{\mathrm{d}}\vec{\theta})}{\Sigma_{\mathrm{crit}}} \quad . \tag{4.7}$$

The convergence allows one to discriminate between the two lensing regimes already touched upon: $\kappa < 1$ indicates the weak lensing regime; while with $\kappa > 1$, strong lensing yields the features of Figure 4.1. For a fixed $\beta$, multiple solutions of equation (4.2) are possible in the strong lensing case, each one corresponding to a different image of the source.

One can re-write the deflection angle as the gradient of the *deflection potential* $\psi$: $\vec{\tilde{\alpha}} = \nabla\psi(\vec{\theta})$, where the deflection potential is defined as

$$\psi(\vec{\theta}) = \frac{1}{\pi} \int \kappa(\vec{\theta'}) \, \ln|\vec{\theta} - \vec{\theta'}| \, \mathrm{d}\vec{\theta'} \quad . \tag{4.8}$$

Resembling the three-dimensional Newtonian potential, but projected in two dimensions, the lensing potential obeys the Poisson equation $\nabla^2\psi(\vec{\theta}) = 2\kappa(\vec{\theta})$. Hence, the gravitational lensing analogs of the Newton's second law and the Poisson equations are linked to the reduced deflection angle and the convergence as:

$$\begin{aligned} \nabla\psi(\vec{\theta}) &= \vec{\tilde{\alpha}} \quad , \\ \nabla^2\psi(\vec{\theta}) &= 2\kappa(\vec{\theta}) \quad . \end{aligned} \tag{4.9}$$

### 4.1.2 Gravitational Shear

When one considers extended sources, it is expected that the light rays originating from the different parts of the source undergo a differential deflection. If the deflection angle and its spatial variation are

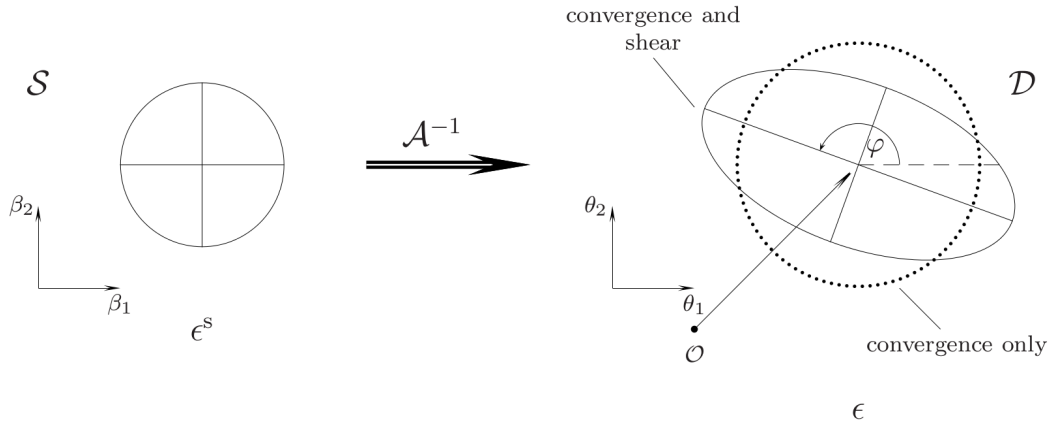


Figure 4.3: Sketch of the effect of the shear on a lensed source. In absence of a lens, the source on the source plane ($\mathcal{S}$) appears circular or, more precisely, it has an intrinsic ellipticity $\epsilon^{(s)}$. The gravitational lensing effect transforms the source in a way that it appears on the lens plane ($\mathcal{D}$) isotropically magnified (dotted circle if $\kappa$ acts alone) and distorted (including the shear effect) as described by a solid ellipse with ellipticity $\epsilon$. Credit: Schneider (2006).

smaller than the scale on which the lens properties change, it is possible to linearize the lens equation:

$$\vec{\beta} - \vec{\beta_0} = \mathcal{A}(\vec{\theta_0})(\vec{\theta} - \vec{\theta_0}) \quad , \tag{4.10}$$

defined around the pivot point $\vec{\beta_0} = \vec{\beta}(\vec{\theta_0})$. As a consequence, the distortion of the images can be described by the *Jacobian* matrix $\mathcal{A}$ (the Jacobian of the lens equation), defined as:

$$\mathcal{A}(\vec{\theta}) = \frac{\partial\vec{\beta}}{\partial\vec{\theta}} = \left(\delta_{i,j} - \frac{\partial^2\psi(\vec{\theta})}{\partial\theta_i\theta_j}\right) = \begin{pmatrix} 1-\kappa-\gamma_1 & -\gamma_2 \\ -\gamma_2 & 1-\kappa+\gamma_1 \end{pmatrix} = (1-\kappa)\begin{pmatrix} 1-g_1 & -g_2 \\ -g_2 & 1+g_1 \end{pmatrix} \quad , \tag{4.11}$$

where $\gamma \equiv \gamma_1 + i\gamma_2$ is the complex *shear* and $g = \gamma(\vec{\theta})/(1-\kappa(\vec{\theta}))$ is the complex *reduced shear*. To see the relation between the lensing potential (equation (4.8)) and the shear and the convergence, one can use the partial derivatives of equation (4.11), obtaining:

$$\gamma_1 = \frac{1}{2}\left(\frac{\partial^2\psi}{\partial\theta_1^2} - \frac{\partial^2\psi}{\partial\theta_2^2}\right) \quad , \quad \gamma_2 = \frac{\partial^2\psi}{\partial\theta_1\partial\theta_2} \quad , \quad \kappa = \frac{1}{2}\left(\frac{\partial^2\psi}{\partial\theta_1^2} + \frac{\partial^2\psi}{\partial\theta_2^2}\right) \quad . \tag{4.12}$$

Remapping a source by $\mathcal{A}$ yields different effects depending on the actions of the convergence and the shear. While the shear distorts anisotropically the image of the sources, in the weak lensing regime ($\kappa \ll 1$) the convergence also isotropically magnifies it. The boost of the observed flux of the source is indicated by the quantity $\mu$, called *magnification*, which can be calculated as the inverse of the determinant of $\mathcal{A}$ as

$$\mu = \frac{1}{\det\mathcal{A}} = \frac{1}{(1-\kappa)^2 - |\gamma|^2} = \frac{1}{(1-\kappa)^2(1-|g|^2)} \quad . \tag{4.13}$$

Solving the lens equation though (4.2) and (4.10), one obtains the image position $\theta$ of a source at the angular position $\beta$. Lensing does not absorb nor emits photons, then the surface brightness of the lensed objects is preserved in the transformation from the source plane to the lens plane (see Figure 4.3). As a consequence, the surface brightness at a point $\theta$ in the lens plane is given by

$$I_\nu(\vec{\theta}) = I_\nu^{(s)}\left[\vec{\beta}(\vec{\theta})\right] = I_\nu^{(s)}\left[\vec{\beta_0} + \mathcal{A}(\vec{\theta})(\vec{\theta} - \vec{\theta_0})\right] \quad , \tag{4.14}$$

where the superscript $(s)$ indicates the quantities not yet lensed, and $I_\nu = S_\nu/\mathrm{d}\omega = S_\nu^{(s)}/\mathrm{d}\omega^{(s)}$ with $S_\nu$ being the flux at frequency $\nu$ and solid angle $\mathrm{d}\omega$.

## 4.2 Weak Gravitational Lensing

As discussed in the previous section, measuring this distortion allows one to reconstruct the mass distribution of the lens as treated in Section 4.3. However, recovering the shear is a tricky task: in contrast with the simple example presented in Figure 4.3, galaxies are far from being perfect circles. Each galaxy has an intrinsic ellipticity, which is modified by the tidal gravitational force of the lens and by instrumental effects as well. This yields an observed light distribution which is different from the one expected in the absence of a lens.

The typical shear induced by the lensing effect of a galaxy cluster is much smaller than the intrinsic ellipticity of the source. In particular, if the central region of a galaxy cluster is avoided, the conditions of tiny distortions and magnifications, $|\gamma| \ll 1$ and $|\kappa| \ll 1$ hold, defining the weak lensing regime.

### 4.2.1 Image Distortion and Magnification

For measuring the shear, i.e. the tiny distortion of the image of the lensed objects, one needs first to define some quantities. It is commonly used to describe the light distribution of an object by its *brightness moments*. The first two moments are

$$\begin{aligned} I_{(1)} &:= \vec{\bar{\theta}} = \frac{\int \vec{\theta}\, W\left(I\left(\vec{\theta}\right)\right) I\left(\vec{\theta}\right) \mathrm{d}^2\vec{\theta}}{\int W\left(I\left(\vec{\theta}\right)\right) I\left(\vec{\theta}\right) \mathrm{d}^2\vec{\theta}} \quad , \\ I_{(2)} &:= Q = Q_{i,j} = \frac{\int \left(\theta - \bar{\theta}_i\right)\left(\theta_j - \bar{\theta}_j\right) W\left(I\left(\vec{\theta}\right)\right) I\left(\vec{\theta}\right) \mathrm{d}^2\vec{\theta}}{\int W\left(I\left(\vec{\theta}\right)\right) I\left(\vec{\theta}\right) \mathrm{d}^2\vec{\theta}} \quad , \end{aligned} \tag{4.15}$$

where $I_{(1)} = \vec{\bar{\theta}} = (\bar{\theta}_1, \bar{\theta}_2)$ is the image center and $W(I(\vec{\theta}))$ is a weight function. The second brightness moments allow as to use the ellipticity estimators

$$|\epsilon| = \frac{1-r}{1+r} \quad , \quad |\chi| = \frac{1-r^2}{1+r^2} \quad , \tag{4.16}$$

which are equivalent, but while the first is preferentially used in theory, the second is more frequent in practical implementations. They correspond to the complex quantities $\epsilon = |\epsilon|\exp(2\mathrm{i}\phi)$ and $\chi = |\chi|\exp(2\mathrm{i}\phi)$ respectively, where $0 \leq r = b/a \leq 1$. Equations (4.16) can be expressed by the second-order brightness moments as

$$\begin{aligned} \epsilon &:= \frac{Q_{11} - Q_{22} + 2\mathrm{i}Q_{12}}{Q_{11} + Q_{22} + 2\sqrt{Q_{11}Q_{22} - Q_{12}^2}} \quad , \\ \chi &:= \frac{Q_{11} - Q_{22} + 2\mathrm{i}Q_{12}}{Q_{11} + Q_{22}} \quad . \end{aligned} \tag{4.17}$$

Both expressions differ only for their absolute values, while they have a common orientation, given the same numerator. The mapping of the source ellipticity into the image ellipticity is performed through the second-order brightness moments transformation $Q^{(s)} = \mathcal{A}Q\mathcal{A}$. For the reduced shear this yields the

transformations for the ellipticity estimators:

$$\epsilon = \begin{cases} \dfrac{\epsilon^{(s)} + g}{1 + g^* \epsilon^{(s)}} & \text{for} \quad |g| \leq 1 \\ \dfrac{1 + g\epsilon^{(s)*}}{\epsilon^{(s)*} + g^*} & \text{for} \quad |g| > 1 \end{cases} \tag{4.18}$$

and

$$\chi = \frac{\chi^{(s)} + 2g + g^2 \chi^{(s)*}}{1 + |g|^2 + 2\mathcal{R}e(g\chi^{(s)*})} \quad , \tag{4.19}$$

with the starred quantities being the complex conjugates. The first of the two equations (4.18), i.e. the $|g| \leq 1$ case, is the one that is relevant to the purposes of our cluster lensing mass estimation.

In our statistically isotropic universe it is fair to assume that the intrinsic orientation of galaxies is completely random. Hence, the expectation value of the source ellipticity is zero:

$$\langle \epsilon^{(s)} \rangle = 0 = \langle \chi^{(s)} \rangle \quad . \tag{4.20}$$

By making use of this fundamental assumption together with equations (4.18) and (4.19), Seitz & Schneider (1997) showed that

$$\langle \epsilon \rangle = \begin{cases} g & \text{for} \quad |g| \leq 1 \\ 1/g^* & \text{for} \quad |g| > 1 \end{cases} \tag{4.21}$$

hence, the reduced shear $g$ is the quantity that is possible to measure from the image ellipticity of a large ensemble of sources. However, each image ellipticity is an unbiased, but very noisy estimator of the reduce shear. This noise can be calculated from the dispersion of the $N$ source intrinsic ellipticity as:

$$\sigma_\epsilon = \sqrt{\frac{1}{2N} \sum_{i=1}^{N} \left( \epsilon_{1,i}^2 + \epsilon_{2,i}^2 \right)} \quad . \tag{4.22}$$

The preferential choice for $\epsilon$ in the theoretical treatment, is justified by the fact that $\chi$ does not have an easy form as the one in equations (4.21). However, $\chi$ is preferred for practical use because it does not require to distinguish different cases, as seen in equation (4.19). In this work the code implementation is based on $\chi$. A further advantage of using this formalism comes from the fact that the method we employ for the shear measurement, introduced by Kaiser et al. (1995, hereafter KSB), has been developed few years before the introduction of equations (4.18) for $\epsilon$.

Since the intrinsic ellipticity is usually one order of magnitude higher than the signal induced by the presence of a lens, the approach of weak lensing can only be statistical. In particular, for cluster lensing, to obtain large samples of background galaxies it is strongly preferred to use wide-field cameras with large field of view. This allows one to collect more information about the $|g| \leq 1$ regime and to reach a statistically sufficient number of objects to fairly use equation (4.20).

### 4.2.2 Shear Decomposition

The shear can be decomposed into its *tangential* and *cross* component, indicated by $\gamma_\mathrm{t}$ and $\gamma_\times$, respectively. They are defined as:

$$\gamma_\mathrm{t} = -\mathcal{R}e(\gamma\, \mathrm{e}^{2\mathrm{i}\psi}) \quad , \gamma_\times = -Im(\gamma\, \mathrm{e}^{2\mathrm{i}\psi}) \tag{4.23}$$

Figure 4.4 represent a graphic visualization of those components measured at different position angles

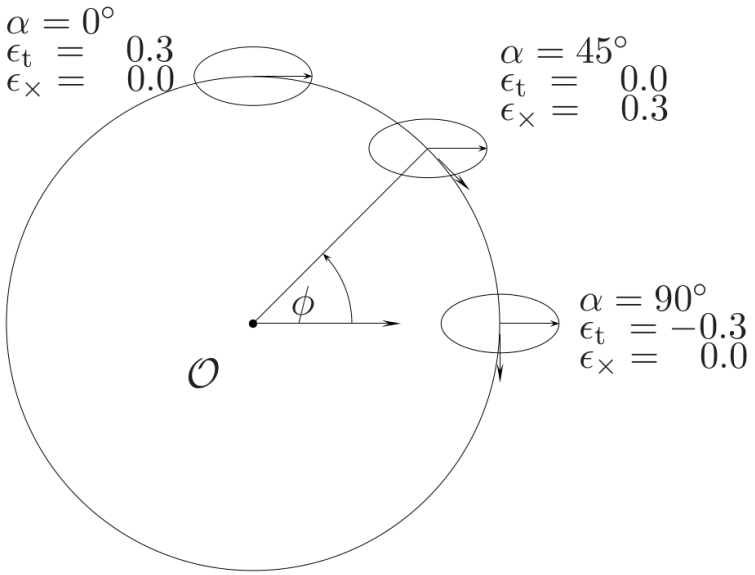


Figure 4.4: Tangential ($\epsilon_t$) and cross ($\epsilon_\times$) component of the ellipticity $|\epsilon| = 0.3$, for three different position angles w.r.t. the reference point $O$. A source with an angle $\phi$ w.r.t. $O$ has the orientation of its tangential vector equal to $\alpha = \pi - \phi$. Credit: Schneider (2006).

with respect to a reference point $O$. The positive value of $\gamma_t$ is always ensured in the case of a tangential alignment of the source. On the other hand, a radial orientation would produce a negative tangential shear. Given the fact that the shear is polar, $\gamma_\times$ is zero in both cases.

In the case of axisymmetric projected matter distribution of galaxy clusters was, background galaxy images are expected to show a tangential elongation aligned around the cluster center. In this paradigm, one would measure $|\gamma| = \gamma_t$ and $\gamma_\times = 0$. The last condition is not true in a real case, even if one considers a spherically-symmetric mass distribution as lens. This is due, as anticipated, to the noise of the intrinsic ellipticity. However, the cross shear is expected to vanish on average and can be used to check for systematics in the shear measurement analysis.

### 4.2.3 Aperture Mass

The *aperture mass* is a method useful for the detection of galaxy clusters through weak gravitational lensing. Schneider (1996) initially devised this tool to address the problem of *mass-sheet degeneracy*: for a given deflector, $\kappa$ can only be constrained up to a constant $\lambda$, implying that it is not possible to distinguish between $\kappa$ and $\kappa'$, where

$$\kappa'(\vec{\theta}) = \lambda\kappa(\vec{\theta}) + (1 - \lambda) \quad . \tag{4.24}$$

The aperture mass is the estimate of the tangential shear around a central point $\vec{\theta_c}$ filtered by a function and is formally defined as:

$$M_{ap}(\vec{\theta_c}) = \int_0^{\theta_{out}} \gamma_t(\vec{\theta} - \vec{\theta_c}) Q(\theta)\, d^2\vec{\theta} = \int_0^{\theta_{out}} \kappa(\vec{\theta}) \mathcal{U}(|(\vec{\theta} - \vec{\theta_c}|)\, d\vec{\theta} \quad , \tag{4.25}$$

where $\theta_{\rm out}$ is the radius of the aperture, while the filter functions $Q$ and $\mathcal{U}$ satisfy the conditions:

$$Q(\theta) = \frac{2}{\theta^2}\int_0^{\theta} \theta'\,\mathcal{U}(\theta')\mathrm{d}\theta' - \mathcal{U}(\theta) \qquad \int_0^{\theta_{\rm out}} \theta'\,\mathcal{U}(\theta')\,\mathrm{d}\theta' = 0 \quad . \tag{4.26}$$

Furthermore, one can estimate the detection significance by using a signal-to-noise ratio where a discretized version of the aperture mass is divided by a noise term which accounts for the intrinsic source ellipticity of equation (4.22). This ratio is also called *S-statistics* and is defined:

$$S_{\theta_{\rm out}}(\vec{\theta_{\rm c}}) = \frac{\sqrt{2}}{\sigma_\epsilon}\frac{\sum_j \epsilon_{{\rm t},j}\,Q_j(|\vec{\theta_j} - \vec{\theta_{\rm c}}|)}{\sqrt{\sum_j Q_j^2(|\vec{\theta_j} - \vec{\theta_{\rm c}}|)}} \quad , \tag{4.27}$$

where $\epsilon_{{\rm t},j}$ is the tangential ellipticity for each galaxy at the position $\vec{\theta_j}$ within the aperture $\theta_{\rm out}$ and with respect to the center $\vec{\theta_{\rm c}}$.

The strength of the shear effect of a galaxy cluster strongly depends on the angular diameter distance ratio: $D_{\rm ds}/D_{\rm s}$, as noticeable from the definition of the critical surface mass density described by equation (4.6). As a consequence, it is of crucial importance to estimate the background source distances in the most accurate way possible. As weak lensing analyses of galaxy clusters are based on the statistical study of a large sample of background sources, one has to consider observationally cheaper options than spectroscopic redshifts. One valid alternative is the use of photometric redshifts, which require the observation of the same cluster field through a minimum of five filter-bands. If none of these methods can be used, other solutions are still possible and are briefly summarized in Section 6.1.

## 4.3 Lensing Mass Reconstruction

The second derivative of the deflection potential gives information about the shear and the convergence. Thus, using equation (4.8) with the definitions of equation (4.12), one finds that the shear can be expressed as the convolution of the convergence $\kappa$ with a kernel $\mathcal{D}$:

$$\gamma(\vec{\theta}) = \frac{1}{\pi}\int \mathcal{D}(\vec{\theta} - \vec{\theta'})\kappa(\vec{\theta'})\mathrm{d}^2\vec{\theta'} \quad , \quad \mathcal{D}(\vec{\theta}) = \frac{-1}{(\theta_1 - \mathrm{i}\theta_2)^2} \quad . \tag{4.28}$$

This equation can be inverted with Fourier transforms, obtaining the description for a mass distribution as:

$$\kappa(\vec{\theta}) = \kappa_0 + \frac{1}{\pi}\int_{\mathbb{R}} \mathcal{R}e\left[\mathcal{D}^*(\vec{\theta} - \vec{\theta'})\gamma(\vec{\theta'})\right]\mathrm{d}^2(\vec{\theta'}) \quad , \tag{4.29}$$

where the constant $\kappa_0$ comes from the fact that a uniform surface mass density does not cause shear. Hence, the reduced shear is insensitive to the mass-sheet degeneracy

$$g = \frac{\lambda\gamma}{\lambda(1-\kappa)} = \frac{\gamma}{1-\kappa} \quad . \tag{4.30}$$

To break the mass-sheet degeneracy we adopt the Seitz & Schneider (1996, 2001) finite-field inversion adaptation of Kaiser & Squires (1993): the mass-reconstruction is done on a finite data field $\mathcal{U}$. The improved method relates the shear to the surface mass density by the relation

$$\nabla K_g(\vec{\theta}) = -\frac{1}{1 - g_1^2 - g_2^2}\begin{pmatrix} 1-g_1 & -g_2 \\ -g_2 & 1+g_1 \end{pmatrix} = \begin{pmatrix} g_{1,1} + g_{2,2} \\ g_{2,1} - g_{1,2} \end{pmatrix} = \vec{u_g}(\vec{\theta}) \quad , \tag{4.31}$$

where $K_g(\vec{\theta}) = \ln(1 - \kappa(\vec{\theta}))$ is a non-linear version of $\kappa$. From the derivative of equation (4.31) one obtains

$$\nabla^2 K = \nabla \cdot \vec{u_g} \quad , \quad \text{with} \quad \vec{n} \cdot \nabla K = \vec{n} \cdot \vec{u_g} \quad . \tag{4.32}$$

Equations (4.32) represent the conditions defining a finite-field Neumann boundary problem which can be solved numerically.

In this thesis the estimate of the cluster mass is performed via the fitting of the tangential shear profile. Nevertheless, we use S-statistics (a modified version, see Section 6.1.3) and convergence maps for further tests, such as the investigation on the possible presence of third-party contributors to the shear signal.

CHAPTER 5

# Sample and Data Reduction

Galaxy clusters are the most massive gravitationally-bound objects located at the intersection of the cosmic web. They serve both as a precious geometric and growth of structure probe, allowing us to investigate fundamental cosmology in a complementary way to other approaches (i.e., supernovae type Ia, cosmic microwave background, the growth rate of linear density perturbations and the baryonic acoustic oscillations; see Albrecht et al. (2006) for a review). The behavior of the cluster mass function is a powerful tool for the accurate estimation of cosmological parameters, such as the amplitude of density perturbations $\sigma_8$ and the matter density of the universe $\Omega_\mathrm{m}$, as well as the $w_0$-parameter in the dark energy equation-of-state (e.g., Voit 2005; Mantz et al. 2008, 2010b, 2015; Vikhlinin et al. 2009b; Planck Collaboration et al. 2015a). Furthermore, it has been shown that cluster counts play an important role since they explore the orthogonal space to the SNIa and CMB results in the $\Omega_\mathrm{m}$-$w_0$ plane (e.g., Vikhlinin et al. 2009b).

To construct such a cluster mass function, distinct methods at different wavelengths are used to weigh galaxy clusters. As an example, the X-ray emission from their hot intracluster medium allows us to accomplish this task. However, the introduction of some assumptions, such as hydrostatic equilibrium, spherical symmetry and intracluster medium composition is needed. The systematics due to these assumptions are reflected on the study of the correlation between several X-ray observables (i.e., $L_\mathrm{X}$–$M_\mathrm{tot}$, $T_\mathrm{X}$–$M_\mathrm{tot}$, etc.). Hence, further checks on the adopted models are indispensable.

### 5.0.1 Cluster Mass Calibration through Weak Gravitational Lensing

Weak gravitational lensing (WL) represents a solid complementary support for cluster mass determination, as this method is sensitive to dark and luminous matter alike and it is not affected by the dynamical state of the cluster. A robust estimate of cosmological parameters is strongly dependent on the selection of the sample of clusters of galaxies. Homogeneity and statistical completeness are fundamental to obtain a good assortment of objects in order to grasp reliable scaling relations (Sereno & Ettori 2015). Combining X-ray and WL analysis of a complete X-ray selected sample of galaxy clusters yields more precise mass models, free of assumptions on the connection between dark and ordinary matter, which are instead needed in the X-ray approach (e.g., Kravtsov et al. 2006). Also, corrections for biases and systematics in both approaches can be performed.

Furthermore, the cross-calibration between different methods is recently gaining a strong importance (Rozo et al. 2014) thanks to recent results showing how WL can be used as an impartial probe to inspect on the tension between *Planck* CMB temperature anisotropies and Sunyaev-Zel'dovich (SZ) cluster count cosmology (Planck Collaboration et al. 2014, 2015c).

Table 5.1: List of previous works on the calibration of the hydrostatic mass bias comparing weak lensing with X-ray or SZ observations. All masses are adapted to the standard cosmology of this paper and are not multiplied by the evolution factor. (*I*) Reference papers where the mass calibration is studied. (see text in Section 7.1.4 for references of the masses they use); (*II*) number of objects used in the study; (*III*) comparison we take into account, as some projects explore both correlations; columns (*IV*) and (*V*) list the redshift and mass ranges of the sample (see Figure 5.1 for a visual representation); (*VI*) hydrostatic bias defined as $b = 1 - \langle M/M^{\rm WL}\rangle$. The reference papers for the listed samples are: [(1)] Israel et al. (2014), [(2)] Israel et al. (2015), [(3)] Donahue et al. (2014), [(4)] von der Linden et al. (2014b), [(5)] Applegate et al. (2016), [(6)] Hoekstra et al. (2015), [(7)] Smith et al. (2016).

| Work (*I*) | # of Clusters (*II*) | Comparison (*III*) | $z$ Range (*IV*) | $M^{\rm WL}$ Range [$\times 10^{15} h_{70}^{-1} {\rm M}_\odot$] (*V*) | Bias ($b$) (*VI*) |
|---|---|---|---|---|---|
| 400dCS Chandra[(1)] | 8 | X-ray/WL | 0.39–0.80 | 0.13–0.57 ($M_{500}$) | no bias (3%) |
| 400dCS Scaled XMM[(2)] | 8 | X-ray/WL | " | " | 21±4% |
| CLASH-X[(3)] | 3 to 20 | X-ray/WL | 0.19–0.69 | 0.4–2.2 ($M_{2500}$) | 12±7% |
| WtG[(4)] | 22 | SZ/WL | 0.15–0.70 | 0.4–2.5 ($M_{500}$) | 31±7% |
| relaxed WtG[(5)] | 12 | X-ray/WL | 0.15–0.54 | 0.20–0.67 ($M_{2500}$) | no bias (-4%) |
| CCCP[(6)] | 37 | SZ/WL | 0.15–0.55 | 0.1–2.2 ($M_{500}$) | 24±7% |
| LoCuSS[(7)] | 50 | X-ray/WL | 0.15–0.30 | 0.4–1.7 ($M_{500}$) | no bias (5%) |

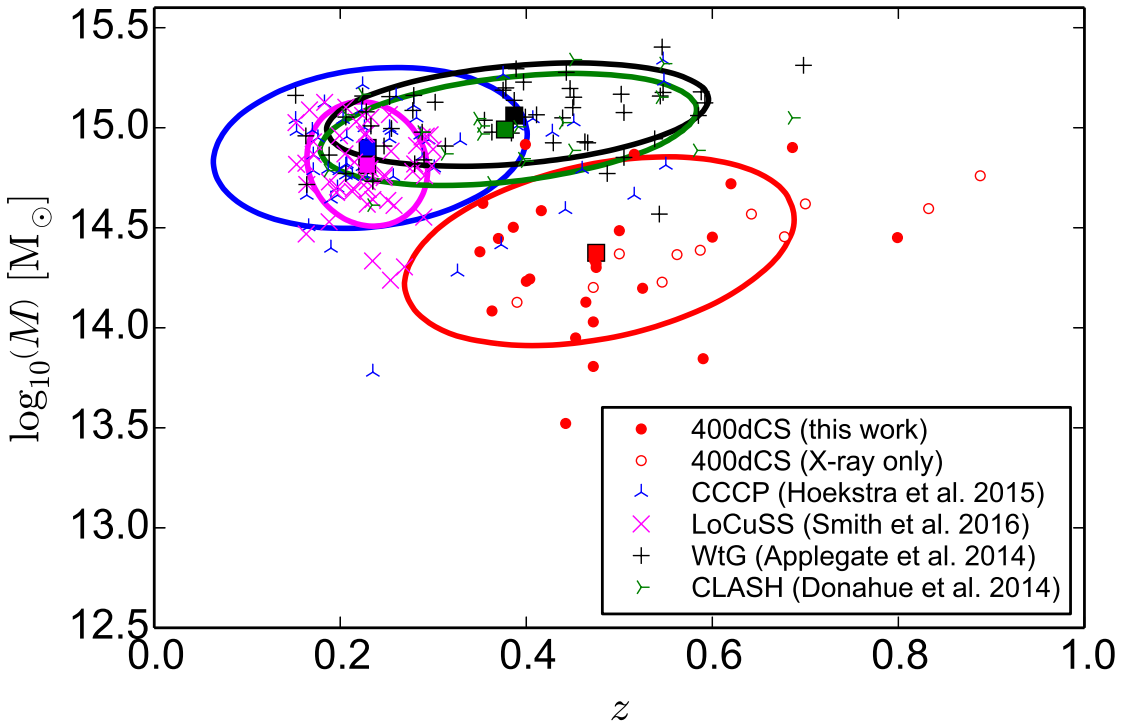


Figure 5.1: Extension in the mass-redshift space of the most studied cluster samples (see Table 5.1), compared with the *400dCS*. The clusters followed-up for this analysis are the filled red circles, while the open red circles are the few remaining *400dCS* clusters. All masses are $M_{500}$. The contours indicate the 68.3% probability of the gaussian kernel estimate on the grid of masses and redshifts for each sample. The squares at the center of the contours lay on the median values. The *400dCS* work covers a region of the parameter space which reaches more typical, for *eROSITA* and *surveys*, but also more challenging low-mass (few times $10^{14}$ $M_\odot$) clusters at higher redshift.

In their analysis, von der Linden et al. (2014a) claim that the two *Planck* results can be reconciled if one accounts for an underestimation of the X-ray masses due *(i)* to the difference in the temperature estimates between the two satellites *Chandra* and *XMM-Newton* (Schellenberger et al. 2015), since *Planck* masses are based on modeling of *XMM* data, and *(ii)* to the "hydrostatic mass bias" ($\langle M^{\rm X}/M^{\rm WL}\rangle = 1-b$) adopted by the *Planck* collaboration, i.e., the underestimation of the true cluster mass by 5-25%.

However, Israel et al. (2014), using a subsample of 8 clusters of the *400d Cosmological Sample* (Burenin et al. 2007; Vikhlinin et al. 2009a,b), show a fairly good agreement between WL and *Chandra* X-ray masses. Schellenberger et al. (2015) find that the shift on $\Omega_{\rm m}$ due to inconsistent calibration of *Chandra* and *XMM* is ∼8% and alone is not enough to justify the offset between *Planck* CMB anisotropy and SZ cluster counts. A recent update by Israel et al. (2015), the direct re-calibration of the *Chandra* masses on *XMM* masses for a small high-mass subsample of eight clusters, indicates that this would significantly ease the tension.

Various other studies in this direction have been performed recently on a variety of mass and redshift ranges using X-ray, optical or SZ as a selection method for compiling galaxy cluster samples. Table 5.1 summarizes the most recent works and the hydrostatic bias they find comparing WL masses either with X-ray or SZ measurements. The redshift and mass ranges of Table 5.1 are also reported in Figure 5.1 as density contours, where it is clear how our sample spans an unexplored region of the mass-redshift space (see Section 7.1.4 for a comparison with the literature).

Persistent disagreement between measurements of hydrostatic mass bias from various cluster samples (von der Linden et al. 2014a; Martino et al. 2014; Israel et al. 2015; Hoekstra et al. 2015) demonstrate that WL masses from a complete sample of clusters are required to make progress. Only a complete sample allows one to correct for Malmquist bias, which hinders the interpretation of the current samples, despite their large sample sizes and small statistical uncertainties.

### 5.0.2 This Project

The present work is based on the *400d Cosmological Sample* (*400dCS* hereafter, defined in Vikhlinin et al. 2009a): one of the highest redshift X-ray selected samples of galaxy clusters, which is statistically complete, homogeneous and flux limited ($1.4\times10^{-13}$ ergs$^{-1}$cm$^{-2}$ in the 0.5–2.0 keV range). It is equally divided into three redshift bins ($0.35 \le z < 0.45$, $0.45 \le z < 0.55$, $0.55 \le z < 0.90$) exploring the high-$z$ universe in a complementary way with other, more local, samples (e.g., *HIFLUGCS*, Reiprich & Böhringer 2002; *LoCuSS*, Smith et al. 2016).

In this study we bring further contribution to the work published by Israel et al. (2010, 2012, 2014, 2015, herafter: I10, I12, I14 and I15) on a subsample of eight clusters observed with the `MEGACAM` instrument at the MMT telescope (from here on named *MMT* clusters). Here we discuss the methods and the results of the weak lensing analysis of 18 additional objects of the *400dCS* observed with the *Inamori Magellan Areal Camera & Spectrograph* (*IMACS*, Dressler et al. 2003) on the Magellan telescope (see section 5.1.2), with the *MegaCam* instrument (Boulade et al. 2003) at the *Canada France Hawaii Telescope* (`CFHT`, see section 5.1.5) and with the *Wide Field Imager* (*WFI*, Baade et al. 1999) of the MPG/ESO telescope at La Silla (Section 5.1.4).

By adding the cluster masses from the present analysis to the initial *MMT* subsample we enhance the statistical significance in determining X-ray–WL scaling relations, using 25 objects. For consistency, for the four three-band *MMT* clusters of Israel et al. (2012) we also refine the background galaxies selection on the shear catalogs with our approach (described in Section 6.1), thus yielding updated but consistent masses.

We adopt a flat $\Lambda CDM$ universe with a Hubble parameter $h = 0.70$ and matter and dark energy densities of $\Omega_{\rm m} = 0.3$ and $\Omega_\Lambda = 0.7$, unless stated otherwise.

In Section 5.2 we report in detail the data reduction technique, similar to those used in Israel et al. (2010, 2012), but enriched with more checks and improvements in order to be completely automated and totally instrument-independent, usable also for challenging data reduction cases such as our *IMACS* data. After describing in Section 5.3 the galaxy ellipticity measurement, we show how the background galaxy selection is applied to all clusters with multi-band data in Section 6.1. The final mass estimates and the scaling relations are discussed in Sections 6.2 and 7.1.

## 5.1 Observations

### 5.1.1 The *400d Cosmological Sample*

The *400dCS* is a subsample of 36 high redshift ($0.35 \leq z < 0.90$) galaxy clusters of the *400 Square Degree Galaxy Cluster Survey* (also known as the *400d*, Burenin et al. 2007), a cluster catalog carefully derived through a well-known selection function, from *ROSAT PSPC* pointed observations. In the framework of the *Chandra Cluster Cosmology Project*, Vikhlinin et al. (2009a,b) obtained a complete coverage in the X-ray band for all the objects of the *400d* high redshift sample by dedicated *Chandra* pointings, as well as *XMM* observations for some of the clusters. Due to the high redshifts, Vikhlinin et al. (2009a, hereafter V09) derived X-ray masses by means of mass proxies: scaling relations between the mass and X-ray observables, i.e., the integrated gas mass $M_{\rm gas}$, the average temperature $T_{\rm X}$ excluding core and the Compton parameter $Y_{\rm X} = T_{\rm X} M_{\rm gas}$. Making use of the cluster mass function, they subsequently yield estimates for cosmological parameters (Vikhlinin et al. 2009b).

Subsequently, Israel et al. (2010, 2012) started the WL follow-up of the *400dCS* and completed the analysis of a subsample of 8 clusters, while a first comparison between the WL and X-ray work have been shown in Israel et al. (2014, 2015).

### 5.1.2 *IMACS*@Magellan Clusters

Table 5.2 contains a summary of the data observed with the *IMACS* wide-field camera of the 6.5m Magellan-Baade telescope, located at the Las Campanas Observatory in Chile. Data for four *400dCS* galaxy clusters have been collected in four observing runs between October 2005 and November 2011, with the characteristics listed in Table 5.3. Over the span of our long observation period, the settings of *IMACS* underwent few changes, which are summarized in Table 5.4. One of these was the introduction of a second mosaic camera (`Mosaic2`) fixed at the f/2 focus, while previously the first and only camera (`Mosaic1`) was allowed to be moved on either of the two foci.

### 5.1.3 *IMACS*@Magellan "Single-run Pre-processing"

Both *IMACS* cameras used in this work, `Mosaic1` and `Mosaic2`, are $8192 \times 8192$ pixels mosaics of eight CCDs equipped with Bessell ($U$, $B$, $V$, $R$, $I$) and Sloan ($u$, $g$, $r$, $i$, $z$) filters. Each of our four *400dCS* clusters is covered by three bands observations: $V$, $R$, $I$ or $g$, $r$, $i$ with `Mosaic1` and $V_2$, $R_2$, $I_2$ with `Mosaic2`. The `IMACS Mosaic1`, being the only CCD available during our first three runs (D, G, and H; see Table 5.3), has been used in both foci (f/2 and f/4) and with different read-out speed modes. Those differences affect the CCD gain, the pixel scale and consequently the field-of-view (f.o.v.) of the pointings. Frames obtained with the f/2 focus are $15\farcm4 \times 15\farcm4$ squares with a pixel scale of $0\farcs111\,\mathrm{pixel}^{-1}$. Using the f/2 focus, one yields a circular image of 15' of radius, with a pixel scale of $0\farcs200\,\mathrm{pixel}^{-1}$. In addition, the field-of-view at f/2 has a 9% vignetted area. As consequence, the unvignetted radius measures $12''$.

Table 5.2: Summary of the *IMACS* data. The seeing is estimated in a patch of $4000 \times 4000$ pixels around the center of the image. Details about the apparent duality of CL0328−2140 and CL0405−4100 observations is explained in Section 5.1.2. The listed coordinates indicate the X-ray center from *Chandra* observations, used in V09. The number of frames ($N_{exp}$), the exposure time ($T_{exp}$) and the seeing here indicated, are calculated after all quality checks and the whole cleaning and testing process are complete (see Section 5.1.3). The last columns indicates the *standards* coverage for each filter, which is run-dependent (see Table 5.3 and Section 5.2.1).

| Cluster | $\alpha$ (J2000) | $\delta$ (J2000) | Redshift | Run ID | Filter | $N_{exp}$ | $T_{exp}$ [s] | Seeing [″] | *Standards* |
|---|---|---|---|---|---|---|---|---|---|
| CL0328−2140_runD | 03:28:35.679 | −21:40:24.62 | 0.59 | D | Bessell-$V$ | 9 | 2700 | 0.74 | Stetson 2.0 |
| | | | | “ | Bessell-$R$ | 14 | 4200 | 0.74 | Stetson 2.0 |
| | | | | “ | CTIO-$I$ | 2 | 1200 | 0.89 | Stetson 2.0 |
| CL0328−2140_runP | 03:28:35.679 | −21:40:24.62 | 0.59 | P | Bessell-$V_2$ | 5 | 1500 | 0.84 | Stetson 2.0 |
| | | | | “ | Bessell-$R_2$ | 24 | 7200 | 0.84 | Stetson 2.0 |
| | | | | “ | CTIO-$I_2$ | 1 | 300 | 1.34 | Stetson 2.0 |
| CL0333−2456 | 03:33:10.596 | −24:56:31.73 | 0.48 | G | Bessell-$V$ | 11 | 6600 | 0.73 | SDSS |
| | | | | D | Bessell-$R$ | 22 | 6570 | 0.59 | Stetson 2.0 |
| | | | | G | CTIO-$I$ | 14 | 4200 | 0.67 | SDSS |
| CL0405−4100_13 | 04:05:24.306 | −41:00:16.95 | 0.69 | H | Sloan-$g$ | 8 | 4800 | 1.52 | SDSS |
| | | | | “ | Sloan-$r$ | 19 | 5700 | 1.02 | SDSS |
| | | | | “ | Sloan-$i$ | 17 | 5100 | 1.02 | SDSS |
| CL0405−4100_14 | 04:05:24.306 | −41:00:16.95 | 0.69 | H | Sloan-$g$ | 8 | 4800 | 1.52 | SDSS |
| | | | | “ | Sloan-$r$ | 22 | 4200 | 1.04 | SDSS |
| | | | | “ | Sloan-$i$ | 17 | 5100 | 1.02 | SDSS |
| CL0542−4100 | 05:42:50.494 | −41:00:04.16 | 0.64 | P | Bessell-$V_2$ | 20 | 6000 | 0.70 | Stetson 2.0 |
| | | | | G | Bessell-$R$ | 12 | 3600 | 0.67 | SDSS |
| | | | | “ | CTIO-$I$ | 19 | 5700 | 1.03 | SDSS |

Table 5.3: Detail on *IMACS* runs and relative configurations.

| Run ID | Start Date | End Date | Camera | Focus | Read-out Speed | Filters | Standards |
|---|---|---|---|---|---|---|---|
| D | 2005-10-29 | 2005-10-31 | Mosaic1 | f/2 | fast | $V$, $R$, $I$ | Stetson 2.0 |
| G | 2006-12-12 | 2006-12-13 | Mosaic1 | f/4 | slow | $V$, $R$, $I$ | SDSS |
| H | 2007-11-08 | 2007-11-10 | Mosaic1 | f/2 | slow | $g$, $r$, $i$ | SDSS |
| P | 2011-11-21 | 2011-11-22 | Mosaic2 | f/2 | slow | $V_2$, $R_2$, $I_2$ | Stetson 2.0 |

Table 5.4: Chronology of *IMACS* changes from first light to present (provided by *IMACS*' PI Alan Dressler in private communication). No data from Mosaic3 were used in this work.

| Period | Camera(s) | Comments |
|---|---|---|
| < March 2008 | SITe Mosaic1 | Movable to f/2 and f/4 |
| March 2008-February 2012 | SITe Mosaic1 @ f/4 | |
| | E2V Mosaic2 @ f/2 | |
| > 2012 February | E2V Mosaic3 @ f/4 | Not used in this work |
| | E2V Mosaic2 @ f/2 | |

In Table 5.2 the clusters CL0328−2140 and CL0405−4100 appear twice. For the former cluster, the reason is that it has been observed during two separate runs but with a difference of 90° in the rotation of the camera. Since the point spread function (PSF) pattern of an image vary with the position on the CCD, we prefer not to stack together differently orientated frames to avoid a contamination of the shear signal. We process separately the two runs as two distinct objects and for photometric reasons (see Section 5.2.1) we use CL0328−2140_runD for the complete lensing analysis. catalog. CL0405−4100, instead, has an unusually large seeing (> 1″) in the lensing band ($R$) due to bad weather conditions during the observations. To find a compromise between image quality and depth, we make two separate selections of the R-band frames to be co-added (i.e., stacked), using two upper limits for the image quality: seeing < 1.″3 for CL0405−4100_13 (19 frames) and seeing < 1.″4 for CL0405−4100_14 (22 frames).

Despite the data being heterogeneous for reasons beyond our control, we show in detail in Section 5.2 that, introducing differentiations in our data reduction procedure, we obtain high quality reduced data products for all of our *IMACS* clusters.

### 5.1.4 *WFI*@MPG/ESO Clusters

For six southern hemisphere galaxy clusters from our sample we obtain and analyze observations performed with the *WFI* at the 2.2m MPG/ESO telescope at the ESO facilities of the La Silla Observatory, Chile (Table 5.5). The field-of-view of *WFI* is a square of ∼30 arcminutes size, composed by eight 2000 × 4000 pixels rectangular chips. As shown in Table 5.6, the *WFI* observations were conducted during six runs. All of the *WFI* clusters have exposures in at least three Bessell bands ($B$, $V$, $R$), with the half of them being observed in the $I$-band as well. Our analysis on those 6 clusters is based on the $B$-, $V$-, and $R$-band. Since the highest quality and deepest observations are obtained with the $R$ filter, we pick this as the lensing band.

Table 5.5: The six *WFI* clusters observed in the *B*, *V*, *R* and *I* bands in six runs. Seeing estimated in a patch of 5000 × 5000 pixels around the center of the image.

| Cluster | $\alpha$ (J2000) | $\delta$ (J2000) | Redshift | Run ID | Filter | $N_{exp}$ | $T_{exp}$ [s] | Seeing [″] |
|---|---|---|---|---|---|---|---|---|
| CL0141−3034 | 01:41:32.670 | −30:34:42.80 | 0.44 | I | *BB#B*/123_*ESO*878 | 24 | 11518 | 1.27 |
| | | | | “ | *BB#V*/89_*ESO*843 | 13 | 3898 | 1.20 |
| | | | | K, L | *BB#Rc*/162_*ESO*844 | 27 | 13497 | 0.82 |
| | | | | “ | *BB#I*/203_*ESO*879 | 60 | 17995 | 1.11 |
| CL0302−0423 | 03:02:21.087 | −04:23:24.36 | 0.35 | I, K, L | *BB#B*/123_*ESO*878 | 22 | 10194 | 0.96 |
| | | | | K | *BB#V*/89_*ESO*843 | 14 | 4199 | 1.06 |
| | | | | K, L, N | *BB#Rc*/162_*ESO*844 | 36 | 17997 | 0.82 |
| CL0318−0302 | 03:18:32.949 | −03:02:55.62 | 0.37 | K, L, M, O | *BB#B*/123_*ESO*878 | 35 | 16797 | 1.32 |
| | | | | L | *BB#V*/89_*ESO*843 | 22 | 6598 | 1.01 |
| | | | | “ | *BB#Rc*/162_*ESO*844 | 17 | 8499 | 0.77 |
| CL0350−3801 | 03:50:40.896 | −38:02:13.07 | 0.36 | I | *BB#B*/123_*ESO*878 | 18 | 8639 | 1.49 |
| | | | | “ | *BB#V*/89_*ESO*843 | 15 | 4499 | 1.27 |
| | | | | “ | *BB#Rc*/162_*ESO*844 | 31 | 15497 | 0.84 |
| CL0355−3741 | 03:55:59.069 | −37:41:43.20 | 0.47 | I | *BB#B*/123_*ESO*878 | 21 | 10078 | 1.37 |
| | | | | “ | *BB#V*/89_*ESO*843 | 15 | 4499 | 1.68 |
| | | | | I, K, L | *BB#Rc*/162_*ESO*844 | 30 | 14998 | 0.84 |
| | | | | K, L | *BB#I*/203_*ESO*879 | 54 | 16195 | 1.11 |
| CL0522−3624 | 05:22:15.362 | −36:25:03.34 | 0.47 | I | *BB#B*/123_*ESO*878 | 20 | 9598 | 1.37 |
| | | | | “ | *BB#V*/89_*ESO*843 | 15 | 4499 | 1.18 |
| | | | | “ | *BB#Rc*/162_*ESO*844 | 27 | 13498 | 0.82 |
| | | | | L | *BB#I*/203_*ESO*879 | 89 | 26693 | 1.01 |

Table 5.6: Details on *WFI* runs and used filters.

| Run ID | Start Date | End Date | Filters |
|---|---|---|---|
| I | 2007-12-03 | 2007-12-15 | $B$, $V$, $R$ |
| K | 2008-09-27 | 2008-10-06 | $B$, $V$, $R$, $I$ |
| L | 2008-11-16 | 2008-12-05 | $B$, $V$, $R$, $I$ |
| M | 2009-10-10 | 2007-10-16 | $B$ |
| N | 2010-01-17 | 2010-01-25 | $R$ |
| O | 2010-10-01 | 2010-10-10 | $B$ |

### 5.1.5 *MegaCam*@CFHT Clusters

From the Canadian Astronomy Data Centre[1] we retrieve *MegaCam* publically available deep data in at least three bands for four of the *400dCS* galaxy clusters (Table 5.7). Also we combine shallow archival data in $g'$- and $r'$-band with our new excellent-quality observations in the $i'$-band with *MegaCam* for three more clusters (observing semester 2015A). Only one newly obtained observation (observing semester 2015B) does not have any complementary data: CL1212+2733. *MegaCam* is a wide-field camera of the 3.6m CFHT in Hawaii, consisting of a 36 CCDs mosaic of $2048 \times 4612$ pixels each. Its f.o.v. is a square of 1 deg$^2$ with a pixel scale of $0\farcs187\text{pixel}^{-1}$. For the present analysis we exploit the complete broad band $g'r'i'$ coverage and the high image quality.

Seven of the eight *MegaCam* fields have observations in all bands centered on the target cluster. Only CL1334+5031, in addition to few exposures in the $g'$-, $r'$- and $i'$-band centered on the cluster, has deeper and higher quality (seeing $< 0\farcs7$) $g'$ and $r'$ observations pointed on another object. This is Abell 1758, a lower-redshift cluster only $\sim 12'$ away from CL1334+5031. As a consequence of coadding frames centered on different objects but all containing our *400dCS* target, the f.o.v. of CL1334+5031 is shrunk to a $41' \times 60'$ rectangle, with the cluster center situated only $\sim 19'$ from the camera edge.

## 5.2 Data Reduction

Consistently with I10 and I12 work, the data reduction of the new 18 objects is executed with `THELI`[2], the optical/IR pipeline used in the *GaBoDS* (Erben et al. 2005; Schirmer 2013) and *CFHTLenS* weak lensing projects (Erben et al. 2009, 2013). We essentially follow the steps thoroughly described in Erben et al. (2005), also ameliorating the pipeline with: (*i*) further sanity checks at critical stages of the reduction (Section 5.2.1); (*ii*) a significant increase in the automation of the procedure (e.g., Section 5.2); (*iii*) universalizing it to be used in a highly automatic way for data from instruments with different characteristics. Furthermore, we incorporate in `THELI` a method (based on the tool `astrometry.net`[3] by David W. Hogg and Dustin Lang) for recovering a first approximate astrometry when orientation information in the headers is missing or corrupted. In Section 5.2 we show how this method is successfully employed for the challenging data reduction of the four *IMACS* clusters.

The *MegaCam* data are reduced following the method illustrated in Erben et al. (2009, 2013), while the *WFI* clusters undergo a procedure similar to the one used for *IMACS*. For all 18 clusters we finally obtain the co-added images in three bands and consequently compose *RGB* color images (see Appendix C).

[1] `http://www.cadc-ccda.hia-iha.nrc-cnrc.gc.ca/en/`
[2] `https://astro.uni-bonn.de/~theli/`
[3] `http://astrometry.net/`

Table 5.7: Data of the eight *MegaCam* clusters. Seeing is estimated in a patch of 7000 × 7000 pixels around the center of the image, except for CL1334+5031, in which the measure has been conducted over 4000 × 4000 pixels. Note that the filters i.MP9701, i.MP9702 and i.MP9703 have almost identical transmissions, therefore in the text we refer to all of them simply as $i'$.

| Cluster | $\alpha$ (J2000) | $\delta$ (J2000) | Redshift | Filter | $N_{exp}$ | $T_{exp}$ [s] | Seeing [″] |
|---|---|---|---|---|---|---|---|
| CL0853+5759 | 08:53:14.403 | +57:59:40.81 | 0.47 | u.MP9301 ($u'$) | 3 | 751 | 0.92 |
| | | | | g.MP9401 ($g'$) | 15 | 600 | 0.84 |
| | | | | r.MP9601 ($r'$) | 5 | 900 | 0.86 |
| | | | | i.MP9703 ($i'$) | 2 | 15996 | 0.62 |
| CL1003+3253 | 10:03:04.734 | +32:53:38.96 | 0.42 | g.MP9401 ($g'$) | 7 | 1760 | 0.85 |
| | | | | r.MP9601 ($r'$) | 15 | 8300 | 0.79 |
| | | | | i.MP9701 ($i'$) | 5 | 1200 | 0.86 |
| | | | | z.MP9801 ($z'$) | 2 | 720 | 0.62 |
| CL1120+4318 | 11:20:06.790 | +43:18:08.23 | 0.60 | g.MP9401 ($g'$) | 13 | 3560 | 0.94 |
| | | | | r.MP9601 ($r'$) | 12 | 7170 | 0.60 |
| | | | | i.MP9701 ($i'$) | 5 | 1200 | 0.88 |
| | | | | z.MP9801 ($z'$) | 5 | 2000 | 0.83 |
| CL1212+2733 | 12:12:18.626 | +27:33:02.28 | 0.35 | i.MP9703 ($i'$) | 6 | 3692 | 0.64 |
| CL1222+2709 | 12:22:01.795 | +27:09:32.15 | 0.47 | g.MP9401 ($g'$) | 3 | 480 | 0.98 |
| | | | | r.MP9601 ($r'$) | 5 | 1341 | 0.81 |
| | | | | i.MP9703 ($i'$) | 9 | 5538 | 0.60 |
| CL1312+3900 | 13:12:18.274 | +39:00:56.62 | 0.40 | g.MP9401 ($g'$) | 9 | 1442 | 1.16 |
| | | | | r.MP9601 ($r'$) | 3 | 780 | 0.88 |
| | | | | i.MP9703 ($i'$) | 7 | 4307 | 0.59 |
| CL1334+5031 | 13:34:20.054 | +50:31:02.92 | 0.62 | g.MP9401 ($g'$) | 4 | 1800 | 0.68 |
| | | | | r.MP9601 ($r'$) | 8 | 4800 | 0.66 |
| | | | | i.MP9702 ($i'$) | 3 | 480 | 0.73 |
| CL1524+0957 | 15:24:40.049 | +09:57:50.99 | 0.52 | g.MP9401 ($g'$) | 4 | 2400 | 0.60 |
| | | | | r.MP9601 ($r'$) | 17 | 9600 | 0.77 |
| | | | | i.MP9702 ($i'$) | 3 | 600 | 1.11 |

In the following sections we exhaustively describe the reduction of the *IMACS* data, separating the single-run pre-processing where data is analyzed in separate runs (Section 5.1.3), from the single-cluster processing where all calibrated frames of a given cluster field are treated together (Section 5.2.1).

The *IMACS* frames present different characteristics depending on the focus used during each run. As noticeable in Figure 5.2, observations conducted with the camera at the f/2 position suffer from few peculiarities. The f/2 f.o.v. is a circle with a radius of 15′ with the outermost 3′ heavily vignetted. Furthermore, the four corners of the camera are totally darkened by the telescope structure. Finally, the moving guiders encroach the field, shadowing it with a $\sim 1 - 2'$ arc, which does not have a fixed position w.r.t. the camera, badly affecting the flat-fielding at the camera borders.

Because of those issues, we would lose roughly the 60% of the information contained in each of the four corner-chips if we try to mask all vignetted and dark areas. Also, the strong distortions noted in those chips would make our astrometry matching difficult and would cause more problems in our later analysis. Especially, heavily masking the corner-chips would also contribute in deteriorating the quality of the final co-added images.

For this, in all observing runs where the focus f/2 is used (D, H and P) we discard the four corner-chips from the very beginning of our data reduction process, but we still mask manually the moving shadows which fall on the remaining chips. In terms of area in the f.o.v., the choice of discarding the four corner-chips is not really expensive. Instead of analyzing a circle with a radius of 15′ (or 12′ if only the unvignetted area would have been considered), we use a rectangle $\sim 14' \times 27'$ (blue rectangle in Figure 5.2). This choice is more reasonable for weak lensing studies, since we neither lose significant area nor contaminate the good data in the inner four chips with the distorted images coming from the corners.

### First Rough Astrometry

The first issue of our *IMACS* data reduction is to recover the right astrometry, the orientation of the telescope at the moment of the observation, and the correct arrangement of the CCD chips, as theis information is missing from the headers of the single frames.

Our raw data consist of `fits` files with no indication about the CCD chip orientation and its relative position w.r.t. the other chips. To recover the orientation (`CD` matrix) and a first rough astrometric solution for each chip, we compare the few brightest stars in the single chips of the mosaic separately with a reference catalog. This is applied on only one frame for each run by means of `astrometry.net` using `SExtractor` (Bertin & Arnouts 1996) (to give a customized configuration file) as the source detection tool and *USNO-B1* as the external catalog. As at this step we want to quickly set up only an approximate astrometry, we choose *USNO-B1* because despite it has a low astrometric accuracy, includes a large number of objects. Then we calculate the rotation and the scaling between the just obtained `CD` matrices of all eight *IMACS* chips, obtaining the exact position of the chips in the mosaic camera. Finally, we transcribe all the recovered information in a configuration file which is subsequently used by `THELI` for updating the headers of all `fits` files of all frames.

Running `astrometry.net` works fine for all runs and chips with the exception for chip 7 in run D which still presents some problems related to rotation. We investigate and solve this issue in three steps. First, we create a catalog running `SExtractor` over the chip 7. We need a fair number of non-saturated objects which correspond to the objects seen in the *USNO-B1* catalog. This is not an easy task to achieve in a f.o.v. of only $\sim 7' \times 14'$ from a 6.5m-class telescope such as Magellan, which reaches saturation very early for the brightest objects. In addition, the photographic plates of *USNO-B1* do not contain many faint stars. Then, we overlay the *USNO-B1* catalog on a *R*-band exposure of the chip 7 and we discard manually all bad detections (e.g., saturated stars and false detections) which are not eventually flagged by `SExtractor`. In the last step, we give this clean catalog to `astrometry.net`, which is now able to

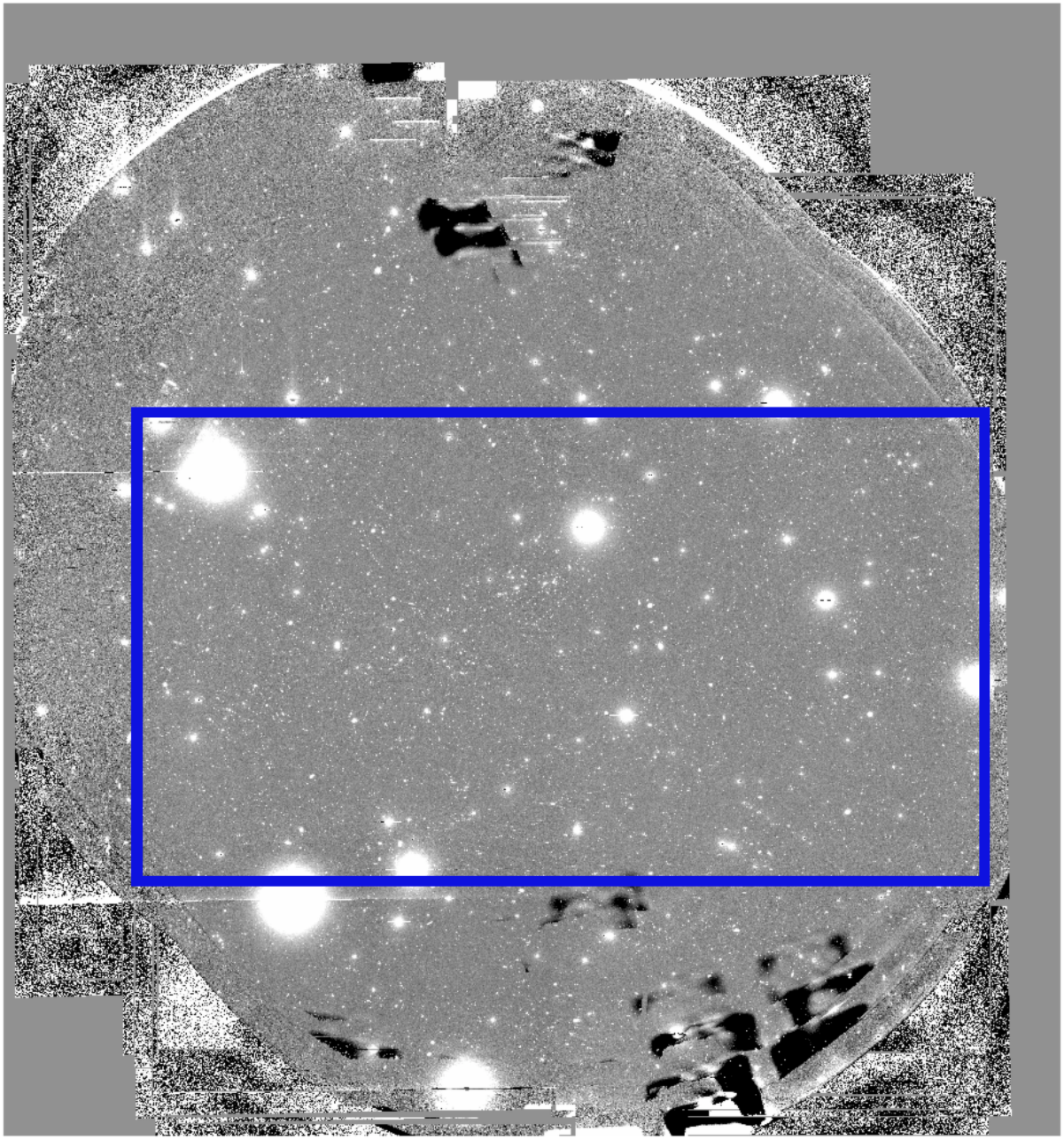

Figure 5.2: Complete 8-chips *R*-band co-added image of the CL0333−2456 field obtained with `Mosaic1` at the f/2 focus. All the problematic features described in the text are easy to spot. The blue rectangle of $\sim 14' \times 27'$ indicates the actual f.o.v. after discarding the four corner-chips.

retrieve a better, but still approximate, astrometric solution.

This new `astrometry.net` feature is now integrated in the structure of `THELI` and works for any multi-chip instrument, retrieving information and updating the `fits` headers in a single step.

### Overscan, *Bias* and *Dark* Correction

Since an offset is added electronically to each pixel value during the read-out of digital cameras, it is needed to subtract a zero-time exposure, called *bias*. This is done by, first, using overscan regions to calculate a mean bias to be subtracted from each single frame. Second, by subtracting from each science and flat-field frame a *master bias*, i.e. the median of all *bias* exposures within the observing run. Overscan regions are unexposed areas, such as chip gaps, which are generally small. For the *IMACS* cameras, `Mosaic1` has chip gaps of ~62 pixels, while `Mosaic2` has gaps of ~92 and ~57 along the long and the short sides, respectively. After having set-up the reference orientation for the CCD, it is easy to trim the chips and subtract the overscans.

Shutter-closed images with exposure times comparable with that of science frames, called *darks*, are also taken during the observing night. As for the *bias* frames, a *master dark* is created in order to spot dead or hot pixels and bad columns on the CCD.

### Flat-fielding and De-fringing

Inhomogeneities in the illumination of the focal plane due to camera properties, defects and dust grains are common features of digital astronomical cameras, as well as pixel-wise variations of the chip response. To correct for these issues, exposures towards a uniformly-illuminated background (e.g. dawn/twilight sky or dome flat-field screen) have to be acquired and *bias*-subtracted for all bands: the *flat* frames. Also in this case a *master flat* is obtained through the stacking of the median of the single *flats*. In the runs where both *domeflats* and *skyflats* are available, we prefer the latter ones after testing that they produce "flatter" science frames. All science frames are then divided by the *master flats* to balance the different pixel sensitivity.

In a following step, we correct for residual inhomogeneities and for the chip-wide sensitivity variations through a *superflat*, usually composed by stacked images of "empty fields" (areas with no or very few objects) captured during the observing night. Given that the f.o.v. of wide-field cameras such as *IMACS* and *MegaCam* is much larger than the extension of our high redshift clusters, we can consider our science images as "empty fields" after having masked out all sources and image defects detected by `SExtractor`, paying particular attention to bright stars and their surrounding halos. If the dithering is sufficiently large or different sky areas have been observed during the night (e.g. *standards*, see Section 5.2.1), the smoothed *superflat* will contain only a diffuse background. The *superflat* is then used as an additional *master flat*.

Finally, from the *superflat* it is possible to extract the fringing patterns of the camera, in order to correct for fringes due to interferences of the light between the CCD layers. We apply the so-called "de-fringing" only to the reddest band ($I$, $I_2$, $i$ for *IMACS* and *MegaCam* and $R$ for *WFI*) data which are however only moderately affected. The fringe pattern is ultimately subtracted from the science frames.

### Single Frame Masking

The passage of artificial satellites during the exposure of the CCD leaves its print on the final image in the form of long thick trails. So, together with other small defects (e.g. reflections on the CCD) satellite tracks have to be removed from the single frames. This yields better quality final stacks than using the outlier rejection method during the co-addition.

To speed up the procedure, we add in THELI the additional feature of the automatic trail and asteroid detection through Hough transforms (Erben et al. 2009). However, we double-check visually inspecting each single-chip image and mask manually eventual unmasked defects, such as the shadows of the moving guiders.

#### Flags and Weights

As done in Erben et al. (2005), we create automatically a weight image for each exposure, which maps the noise (due mainly to the inhomogeneous illumination) in the field thanks to the information contained in the *flat* and *bias* frames processed in the previous steps.

Furthermore, making use of the *master dark*, we generate flag images as well, in order to map dead and hot pixels. The flag images constitute a catalog which will be automatically matched with the lensing catalog extracted from the co-added field. Weight and flag frames are crucial for determining the accuracy of the flux of the objects in the final co-added image.

### 5.2.1 *IMACS*@Magellan "Cluster Processing"

From this step on, we process together all the observations of a given cluster from different nights and runs.

#### Final Astrometric Solution

We use the TERAPIX software SCAMP (Bertin 2006) for matching at the sub-arcsecond level all the exposures of the same cluster. We adopt the *Two Micron All Sky Survey* (2MASS) catalog (Skrutskie et al. 2006) as the astrometric reference. To improve the precision of the astrometry and to have consistency between the astrometric solutions in different bands, SCAMP is run on all frames in all filters for a given cluster at the same time.

The typical internal accuracy (between the frames of the same field) for the *IMACS* clusters is $\sim 0\farcs05$; while the external astrometric accuracy (matching our frames with 2MASS) is $\sim 0\farcs2$.

#### Photometry

Once the positions of the sources in the cluster fields are matched with the astrometric reference catalog, we need to estimate the relative photometric zero-point[4] (ZP) in all frames. This is done using the catalog obtained by SCAMP in the astrometry calibration step.

At this stage we want to obtain an absolute photometric solution, which can be obtained either through a direct (field overlaps with a photometric catalog) or a indirect (using *standard* fields) procedure. Given the position in the southern hemisphere of the four *IMACS* cluster, it is not possible to compare the internally-calibrated fluxes with a reference catalog that covers the same area, such as the *Sloan Digital Sky Survey* (SDSS). For this reason, our strategy has been to set up observations also for *standard* fields covered by the Stetson 2.0 and the SDSS catalogs, depending on the run (see Table 5.3). By means of the indirect method we can constrain the zero-point $Z$, the atmospheric extintion $A$ and the airmass $a$, useful for the calibration of the source magnitudes by the relation:

$$m_{\rm field} = m_{\rm ref} + \alpha c + Aa + Z, \tag{5.1}$$

[4] We adopt the common definition of the magnitude zeropoint as the magnitude of an object that produces 1 count per second in a given band.

where $c$ is the color in the reference catalog and $\alpha$ is the color term. $\alpha$ encloses the difference in filters and instrumental characteristics w.r.t. the reference, but we consider it negligible.

Photometric ZPs are estimated performing a fit of the airmass vs. the $mag_{\rm ref} - mag_{\rm obs}$ distribution of the *standard* fields observations, each night. In a three-parameter fit, the color term is neglected

By means of the indirect method, we can calibrate the ZP as a function of the airmass and the color term, following the method of Hildebrandt et al. (2006). The final ZP in a given band is the average of the ZPs of all photometric nights in a run (see Figure 5.3).

Our *run D* shows non-photometric conditions in the $R$- and $I$-bands, while run P is non-photometric for the $V_2$ and $R_2$ filters. As a consequence, it is not possible to obtain the absolute photometry calibration for the lensing band of the clusters CL0328−2140_runD, CL0328−2140_runP and CL0333−2456. For this reason, we use the galaxy number as an alternative method for calibrating the magnitudes for those two fields.

Additionally, the non-photometric lensing band of CL0328−2140_runP cannot be calibrated with this method since this field is the only one observed with the $R_2$ filter. Consequently, we decide to keep only the CL0328−2140_runD observations for our analysis.

In Figure 5.3 we show the calibration of the $R$-band for CL0328−2140_runD and CL0333−2456 using as reference the good photometry of CL0542−4100. After plotting the number density of galaxies, we apply a linear fit ($\log(x) = mx + b$) in the magnitude range $20 < R < 24$ [5], which is fairly complete in our observations, and does not include saturated stars (upper panel of Figure 5.3). Given the relation

$$R_{\rm cal} m_{\rm cal} + b_{\rm cal} = R_{\rm uncal} \cdot m_{\rm uncal} + b_{\rm uncal} \quad , \tag{5.2}$$

where the subscripts *cal* and *uncal* stand for "calibrated" and "uncalibrated", while $b$ and $m$ are the intercept and the slope in the fit equation, since $R_{\rm cal} = R_{\rm uncal} + \Delta R$, we find the shift we have to employ to the uncalibrated magnitudes as:

$$\Delta R = \frac{R_{\rm uncal} \cdot (m_{\rm uncal} - m_{\rm cal}) - b_{\rm cal} + b_{\rm uncal}}{m_{\rm cal}} \quad . \tag{5.3}$$

Once the shift $\Delta R$ is applied, the fits of all three fields agree very well, as shown in the lower panel of Figure 5.3 and we update the ZP of the two lensing band co-added images.

### Single Frame Sanity Check

Before proceeding to the co-addition of the cluster field, we want to assure homogeneous conditions for the collection of frames we will consider. The quality of the final image relies on the stability of the image characteristics, and on the regularity of the average ellipticity $(e)$[6] pattern over all science images.

Despite in the case of *IMACS* observations we do not need to stack frames from different runs, nevertheless it is important to monitor the variation of the features between the various exposures. We define criteria based on the sky relative zero-point and the seeing condition for filtering the frames. As for our weak lensing study we rely on the shapes of faint and small background galaxies, we fix an upper limit of $1''$ to the seeing of the $R$-band (Figure 5.4), while for the supporting bands we accept seeing conditions up to $1''.5$ at worse.

[5] We estimate the magnitude in the flexible elliptical aperture `AUTO` in `SExtractor`

[6] Here we define the ellipticity in polar quantities as $|e| = (1 - r^2)/(1 + r^2)$ (with $r$ being the minor-over-major axis ratio) and as a complex number with cartesian components $e = e_1 + ie_2$. We express $r$ in terms of second-order brightness moments, as $e = (Q_{11} - Q_{22} + 2iQ_{12})/(Q_{11} + Q_{22})$.

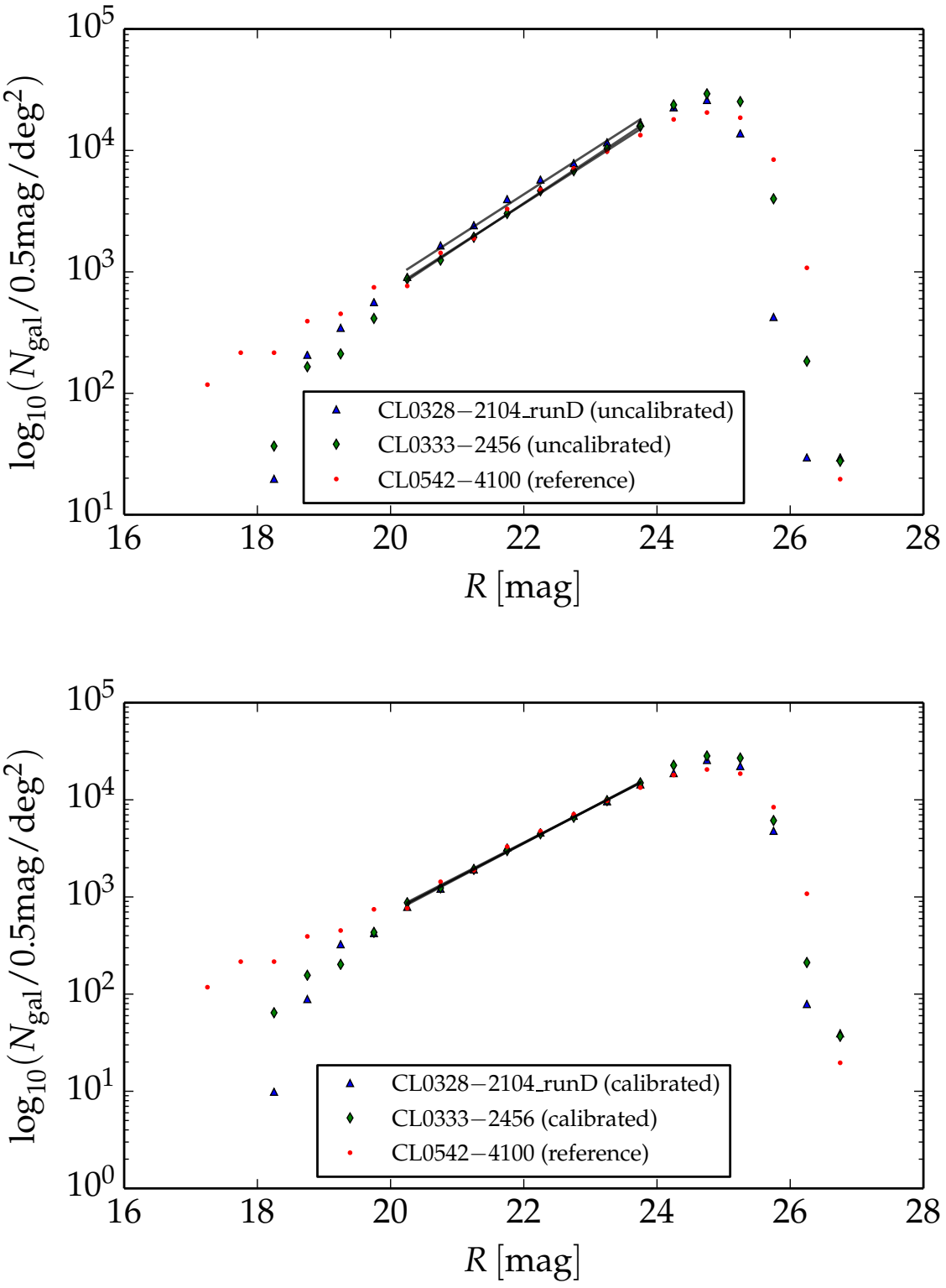


Figure 5.3: Galaxy number method for lensing band photometric calibration. Each distribution of number density is fitted in the range $20 < R < 24$ (*upper panel*). Here the $R$ zeropoints for the uncalibrated catalogs are set to a dummy value of 27.1. A shift between the uncalibrated and calibrated fields is estimated and applied as described in the text. As a result, all the fits overlay each other (*lower panel*).

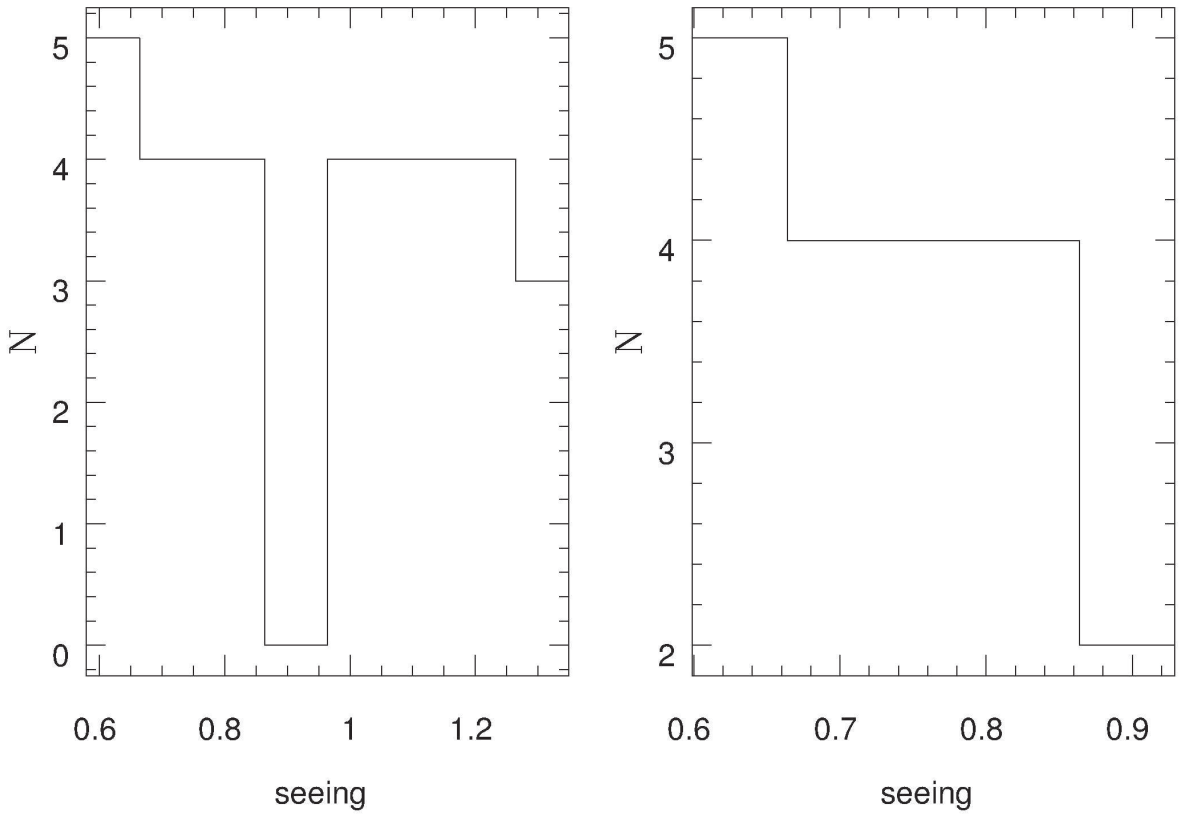


Figure 5.4: Example of sanity check plots for the *R*-band of a single "set". The two histograms represent the seeing distribution (in arcseconds) before (*upper panel*) and after (*lower panel*) the filtering described in Section 5.2.1.

Furthermore, to preserve the photometric accuracy we filter also for the sky relative zero-point. The relative photometric ZPs should stay nearly constant for similar observing conditions. To keep low the noise while co-adding together frames from photometric and non-photometric nights, we discard any frame whose relative ZP is less than 0.2 from the median value of the relative ZPs of all observations of the clusters in a given band.

Those frames which do not meet our seeing and relative ZP criteria, are then rejected and not included in the final co-addition.

We apply a further filtering of the single frames by analyzing the variation of stellar anisotropies. Although the images of stars are not subject to distortions due to the presence of the intervening cluster, it is possible to find a highly anisotropic distribution of the PSF independently from poor seeing conditions. Selecting unsaturated stars of the stellar locus in the lensing band magnitude ($m$) vs. half-light radius ($\theta$) plots (e.g., as shown in Figure 5.5), we estimate a median PSF size of $\theta = 2.2$ pixel for our four *IMACS* cluster fields. For the selected stars in the field we measure the second-order brightness moments

$$Q_{ij} = \int W_{r_g}(|\vec{\theta}|)\theta_i\theta_j I(\vec{\theta})\,\mathrm{d}^2\theta \quad i,j \in \{1,2\} \tag{5.4}$$

where $\theta_i$ and $\theta_j$ are defined w.r.t. the point where the first-order moments of the light distribution ($I(\vec{\theta})$) in the lens plane vanish. We use the typical PSF size of the instrument (median PSF size of all fields) as the radius $r_g$ of the Gaussian weight function $\mathrm{W}_{r_g}$. In Figure 5.6 we show the spatial distribution of

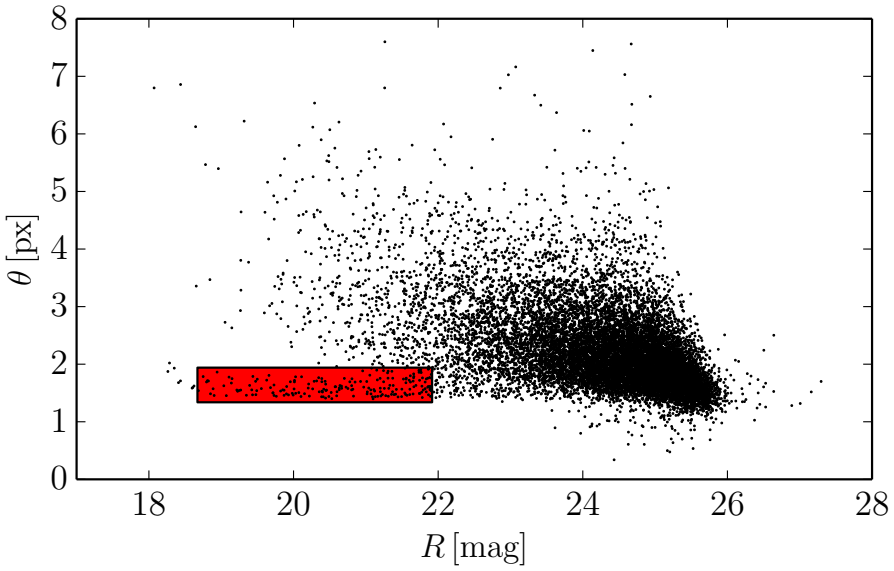


Figure 5.5: Magnitude vs. object size ($\theta$, i.e. `SExtractor`'s `FLUX_RADIUS` or $r_g$ in Section 5.3.1) for the sources in the field of CL0333−2456. In this case, the lensing band is the $R$-band, so $m = R$. The stars of the stellar locus (stars occupy a constant half-light radius region) we consider are included in the red box, with a half-light radius of $\theta = 3.57$, defined as $(\theta^*_{\rm max} + \theta^*_{\rm min})/2$. Here the asterisked quantities define the stellar locus limits. Our selection in this case is based on the following values: $\theta^*_{\rm min} = 1.33$, $\theta^*_{\rm max} = 1.94$, $m^*_{\rm min} = 18.67$, $m^*_{\rm max} = 21.92$. As we want to strictly select only stars, we do not extend our selection to fainter magnitudes, where it would be contaminated by the presence of small faint galaxies. We do it at later stage, after our KSB analysis.

the anisotropy of stars, comparing a good low-anisotropy example (*upper panel*) with one of the few bad cases (*lower panel*) of the same field. The huge anisotropy in the latter case is likely due to tracking or focusing problems during the observation. It is evident that stacking frames with extremely different anisotropies as those shown in Figure 5.6, would counterfeit the shape signal.

Figure 5.7 shows that the average star ellipticity ($\langle e^* \rangle$) of some exposures can behave as outlier w.r.t. the median of the average star ellipticity of all single frames of the same fields. After having computed the mean ellipticity for each frame, we estimate the median for the whole ensemble of exposures and reject those fields which deviate too much from this ellipticity value. We find that a good compromise between the total depth of the good frames using this selection, and the tolerable anisotropy difference, is reached by employing the upper limit of 0.075 (green circle in Figure 5.7).

### Co-addition

Before stacking all the frames which successfully pass our checks, the background sky level has to be modeled and subtracted from those exposures. This is generally done by smoothing each single frame after having masked out all sources detected with `SExtractor`.

The single images and their weights (produced as described in Section 5.2) are then resampled and co-added by `SWarp` (Bertin et al. 2002), making use of the astrometric solution computed by `SCAMP` (Section 5.2.1). The final coaddition is done on a grid where each "new" pixel contains a weighted mean of the corresponding pixels of the single frames.

There is a small complication for two clusters, CL0333−2456 and CL0542−4100, which have at least

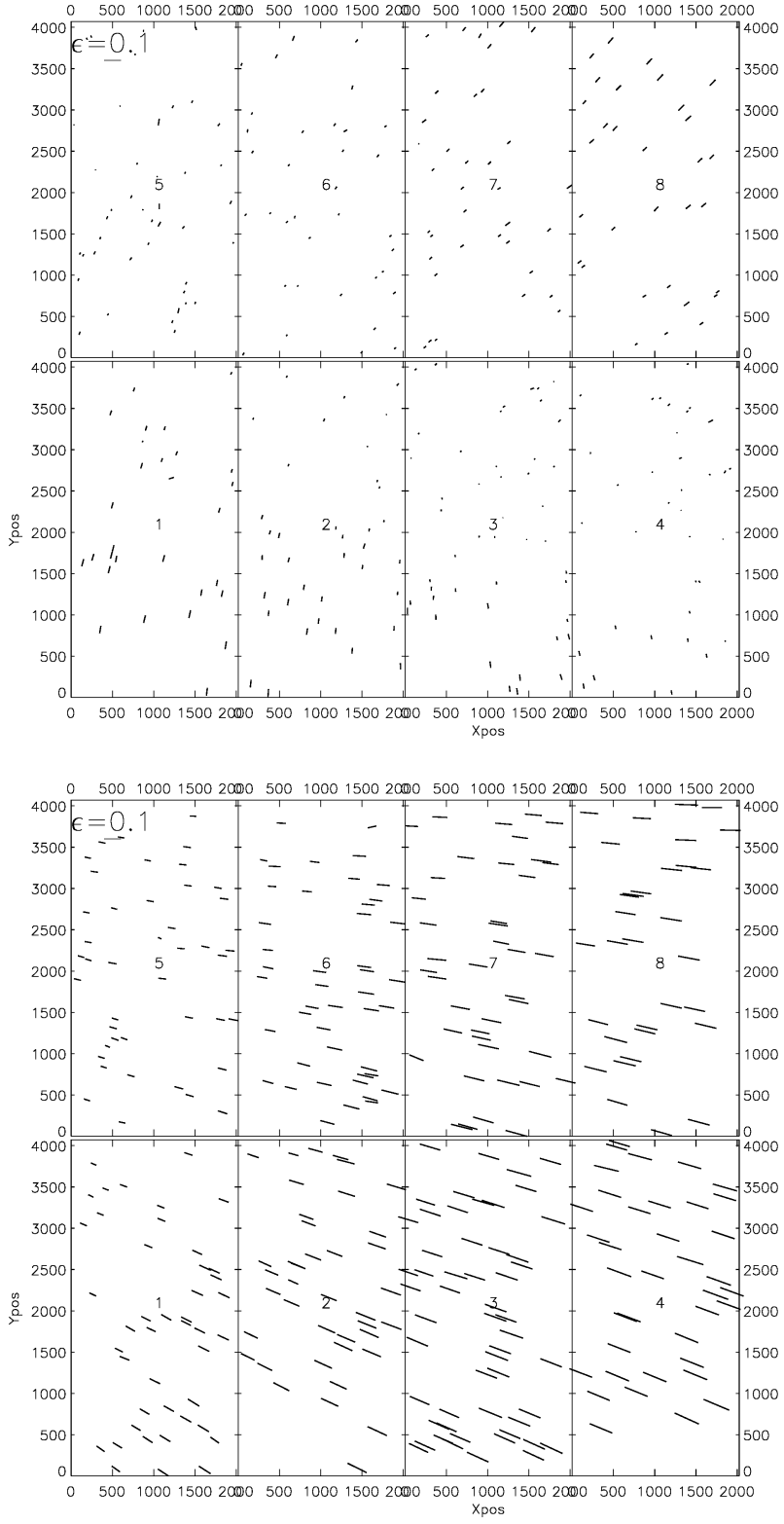


Figure 5.6: Stellar anisotropy check. The stick alignments represent the orientation of the ellipticities of the stars ($e^*$) and their magnitude in a single low-anisotropy (*upper panel*) and a high-anisotropy (*lower panel*) *R*-band frame. The plotted stars fall into the selection criteria of the red box in Figure 5.5.

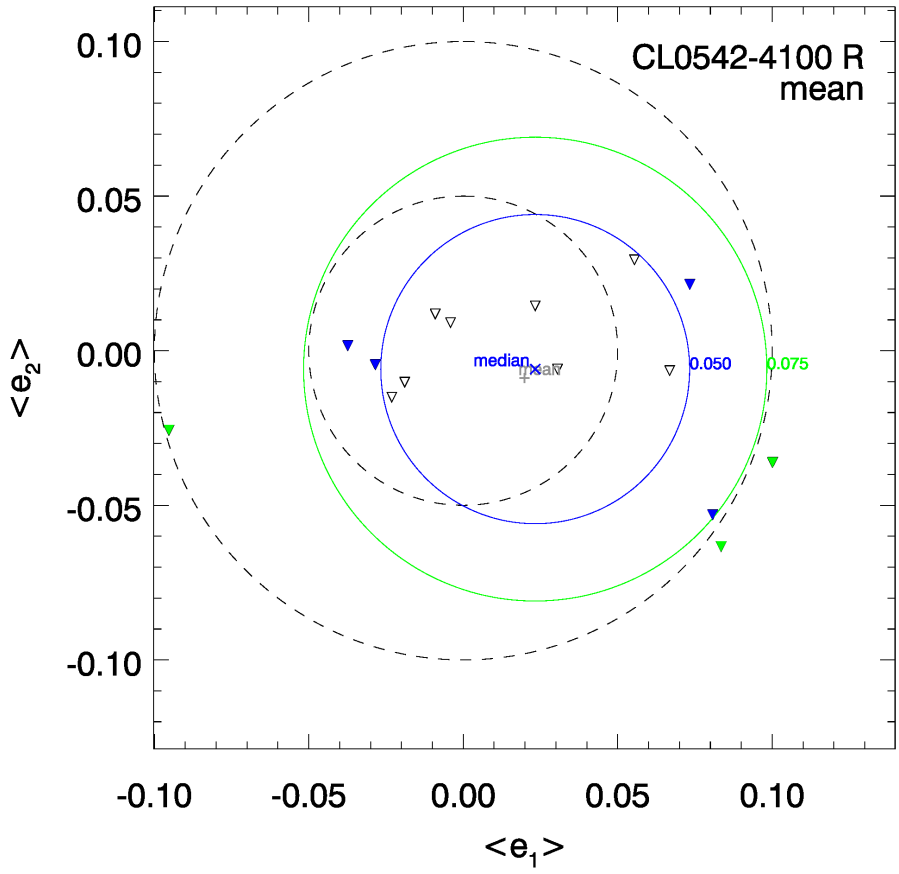


Figure 5.7: Average anisotropies for each exposure of the observation of CL0542−4100 in the *R*-band. Each triangle indicates the mean ellipticity of stars in a single frame. All frames with an ellipticity within the blue and the green circles, respectively 0.050 and 0.075 from the median value of all frames, are considered for co-addition. In this case, only the three green triangles are excluded. The inner and outer dashed black circles indicates a $\langle |e^*| \rangle$ of 0.05 and 0.10 and are only a visual aid.

one of the three bands observed during *run G* with `Mosaic1` used at the focus f/4 (Table 5.2). This means that the pixel scale of the frames observed at this focus is nearly half of those acquired at the focus f/2. When co-adding these two fields, we decide to resample all the frames on a grid whose properties (such as the pixel scale) are based on the lensing band, i.e. *R* or *r* or $R_2$.

Finally, for each cluster we produce co-added images in three bands to be used for background selection (see Section 6.1) making also possible to yield color images. Also flag and weight co-added maps are generated (Figure 5.8). A mosai

### 5.2.2 Pre-KSB "Make-up"

Once the data reduction stage is completed, we prepare all co-added images of all 18 clusters that are analyzed for obtaining the catalogs that will be used for the selection of background galaxies (Section 6.1).

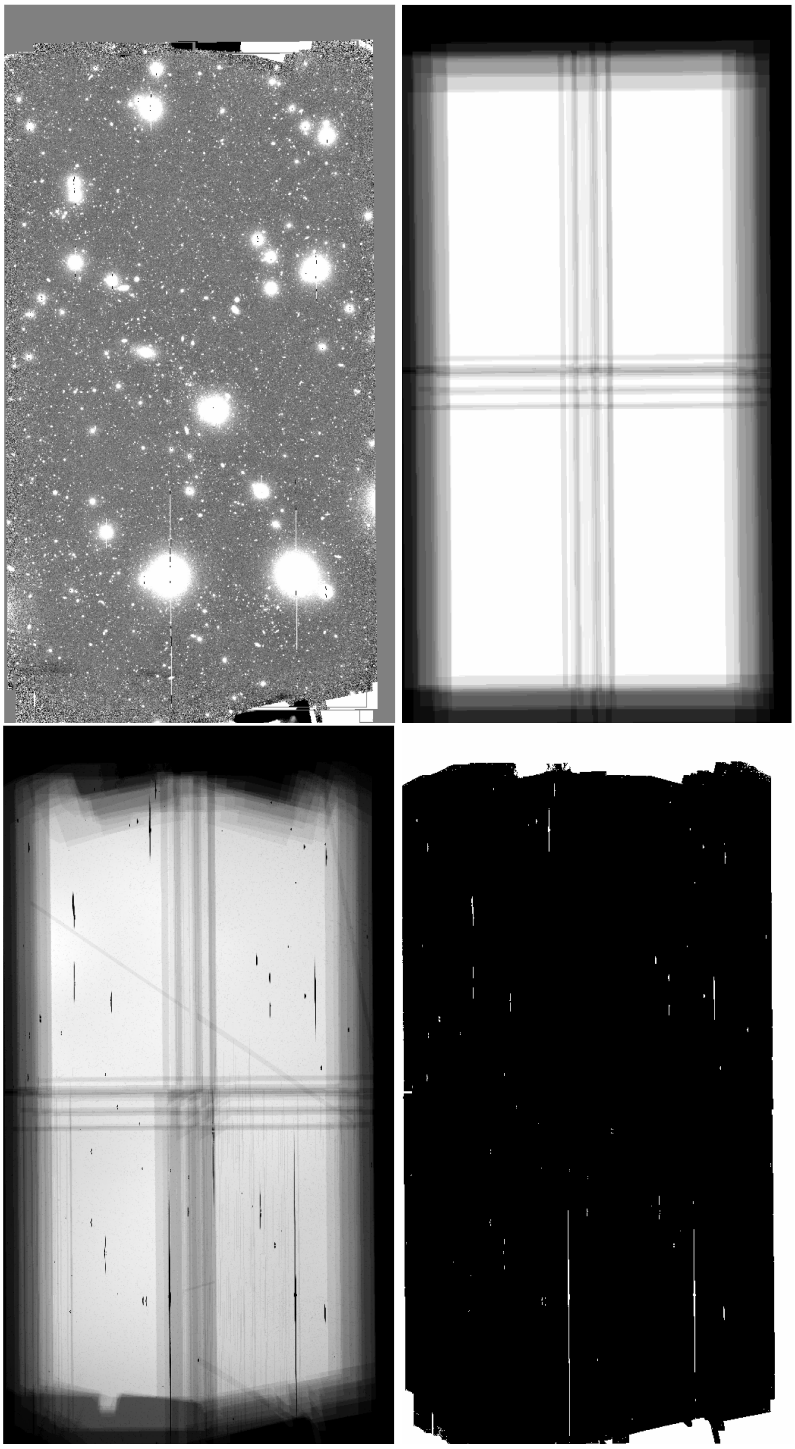

Figure 5.8: Products of co-addition for the *r*-band of CL0405−4100. *Upper panels:* lensing image obtained co-adding only the four central CCD chips (left). The right panel shows the sum of the co-added single frames which is used for selecting the area to be used for the following analysis (see Section 5.2.2). *Lower panels:* the corresponding weight (left) and flag map (right). In the former are well visible the masked "bad" features of the single frames.

### Convolution to the Worst Seeing

To produce reliable colors we need to estimate the photometric quantities in all bands securing an aperture of the same size in all stacked images of the same field. For this, we downgrade all bands to the poorest seeing.

As a first step, we determine the seeing in all bands, defined as the width of the PSF (assumed Gaussian) $\sigma$. Then, `SExtractor` is run for detecting stars and measuring their ellipticity. The convolution to the worst seeing ($\sigma^2_{\rm worst}$) is done through

$$\sigma^2_{\rm worst} = \sigma^2_{\rm orig} + \sigma^2_{\rm kernel} \quad , \tag{5.5}$$

where $\sigma^2_{\rm orig}$ is the seeing of the image to be convolved and $\sigma^2_{\rm kernel}$ is the Gaussian kernel we use for the convolution (see details in Erben et al. 2009).

### New Image Masking

With `THELI` it is possible to mask additional features that would generate fake detections or wrong magnitude estimates in the stacked images. For this purpose instrument-specific `ds9` [7] region templates are automatically adapted to the size and the magnitude of faint and bright stars, including their halos. In addition, also saturated stars and over-/under-dense regions are masked out. Finally, asteroids which are difficult to spot on a single frame image are masked at this stage too, because they appear on the final co-added image as a series of small bright in-line dashes. An example of final masks is shown in Figure 5.9.

The final masks are visually inspected and given as an input to the tool `weightwatcher`[8] together with the co-added weight and flag maps. This tool create new weight and flag maps by applying the masks on the old maps. The new `weightwatcher` weight and flag maps are then used in the following shape measurement analysis.

### Co-added Image Cropping

The three co-added images of each cluster are cut together, accounting for a reasonable overlap of the single frames. The top right panel of Figure 5.8 shows the "sum" image which helps us in this task. It is obtained by co-adding the exposed areas of the CCDs and it well describes the used dithering pattern. In the sum image, each pixel has a value equal to the number of frames covering it. We applied a minimum threshold of 3 to take that pixel into account. This assures identical dimensions for all frames and the same reference values which are used for detecting one object at the same pixel position on all images.

## 5.3 KSB Shear Measurement

We base our shear measurement on the KSB method conceived by Kaiser et al. (1995) and successively revised by Luppino & Kaiser (1997) and Hoekstra et al. (1998). As in I10 and I12, we adopt the "TSfma" implementation presented in Heymans et al. (2006) and thoroughly tested in Schrabback et al. (2007) and Hartlap et al. (2009). In this work we use the formalism described in Schrabback et al. (2007).

[7] `ds9.si.edu/`
[8] `http://www.astromatic.net/software/weightwatcher`

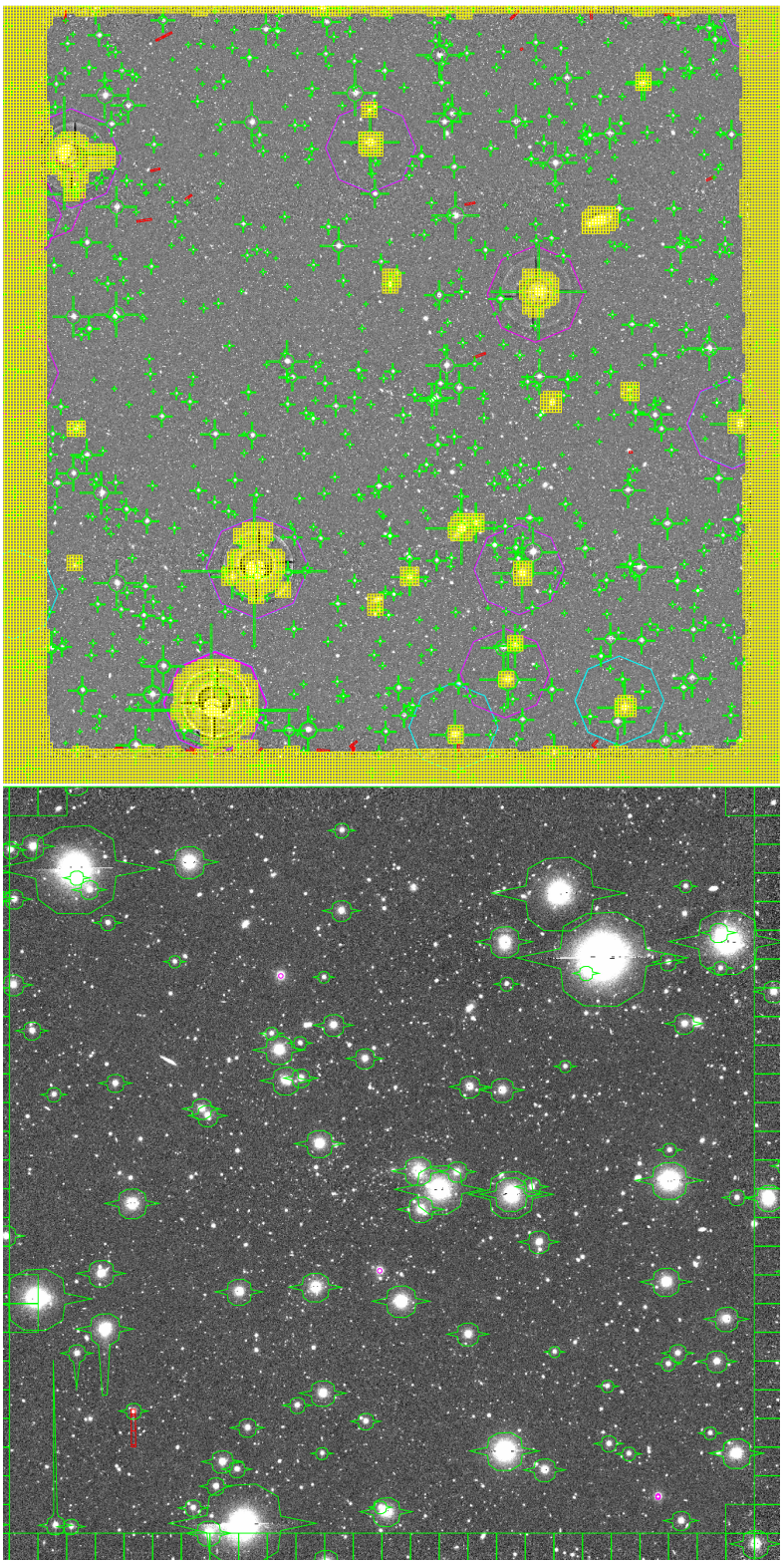

Figure 5.9: Pre-KSB for the *MegaCam* cluster CL1003+3253 (*left panel*) and the cluster CL0542−4100 observed with *IMACS* at the focus f/4 (*right panel*). Here are shown the co-added $r'/R$-band with the various types of masks discussed in Section 5.2.2.

The KSB method recovers the *shear*, i.e. the ellipticity distortion of background galaxy images imparted by the galaxy cluster gravitational potential. This distortion extends the galaxy image shapes in a perpendicular direction w.r.t. the cluster center of mass.

The shear is entangled to other altering effects such as the PSF pattern and the intrinsic ellipticity of galaxies. Exploiting the immunity of stars to intrinsic ellipticity and the lensing effect, we can use their PSF properties to disentangle shear and PSF contributions.

In the limit of small PSF anisotropy ($q^* \ll 1$) and small reduced shear ($g \ll 1$), Kaiser et al. (1995) invert the relation between these two quantities and the intrinsic and observed ellipticities, providing the shear estimator:

$$\epsilon_\alpha = (P^g)^{-1}_{\alpha\beta} e^{\rm ani}_\beta \quad , \tag{5.6}$$

where the PSF-corrected ellipticity has the form of $e^{\rm ani}_\beta = e_\beta - P^{\rm sm}_{\beta\gamma} q^*_\gamma$. Starred quantities indicate properties measured from stars while $e_\beta$ is the observed ellipticity and the tensors $P^{\rm g}$ and $P^{\rm sm}$ describe the transformation of ellipticities under the influence of the cluster gravitational potential and an anisotropic PSF, respectively. This shear estimator is unbiased under the assumption of a random intrinsic ellipticity orientation of the sources.

### 5.3.1 PSF Properties

In our KSB pipeline we run `SExtractor` in "double detection mode": the sources are detected and their shapes measured in the lensing band image, while their photometry is estimated in the three images convolved with the worst seeing. Magnitudes are measured at the position and withing the apertures of the detection band. This ensures that all objects will have a consistent photometry area in order to be able to measure trusty colors.

The clean output catalog contains multi-band merged information only about the sources which have a reliable magnitude estimate in all photometric bands[9]. Also, all deblended sources, or bright neighbouring galaxies are excluded from the original `SExtractor` catalog.

In Figure 5.10 we show the correction for the PSF anisotropy that we apply on CL1003+3253's source catalog. For finding $e^{\rm ani}_\beta$ (Equation 5.6) we need to model the PSF stellar anisotropy $q*$ of the lensing band field and subtract it from the observed ellipticity $e_\beta$.

For each cluster we plot the lensing band magnitude distribution of detected objects vs. their half-light radii, and we select stars[10] from the stellar locus, as shown in Figure 5.5. At this point, the star selection ($\theta^*_{\rm min}$, $\theta^*_{\rm max}$, $m^*_{\rm min}$ and $m^*_{\rm max}$) is performed conservatively with the purpose of avoiding both saturated stars (for $m > m^*_{\rm max}$) and faint small galaxies (at $m > m^*_{\rm max}$). However, for the steps following the KSB shape measurement, we choose more relaxed values which are those contained in Table 5.8.

#### PSF Anisotropy Correction and Lensing Catalogs

The second-order brightness moments of the stars in our selection are estimated using different combinations for the Gaussian window function ($\mathrm{W}_{r_g}$ in Equation 5.4) and for the aperture applied on stars, i.e. the stellar integration limit ($\ell_{\rm SIL}$; see Erben et al. (2001) for details). We model the distribution of the ellipticity of stars by fitting a polynomial. Adopting different polynomial orders ($d_{\rm APO}$), from the first to the seventh order, we find the most accurate correction.

[9] Due to an oversight at this step in I12 paper, we update the masses of the eight *MMT* clusters in the Appendix A. However, as we apply a different background selection method to all 26 clusters, we do not use those updated masses, rather the ones listed in Table 6.2 and discussed in Section 6.2.

[10] We adopt the quick tool `findstars.f90` by C. Heymans and L. Van Waerbeke (Heymans et al. 2006).

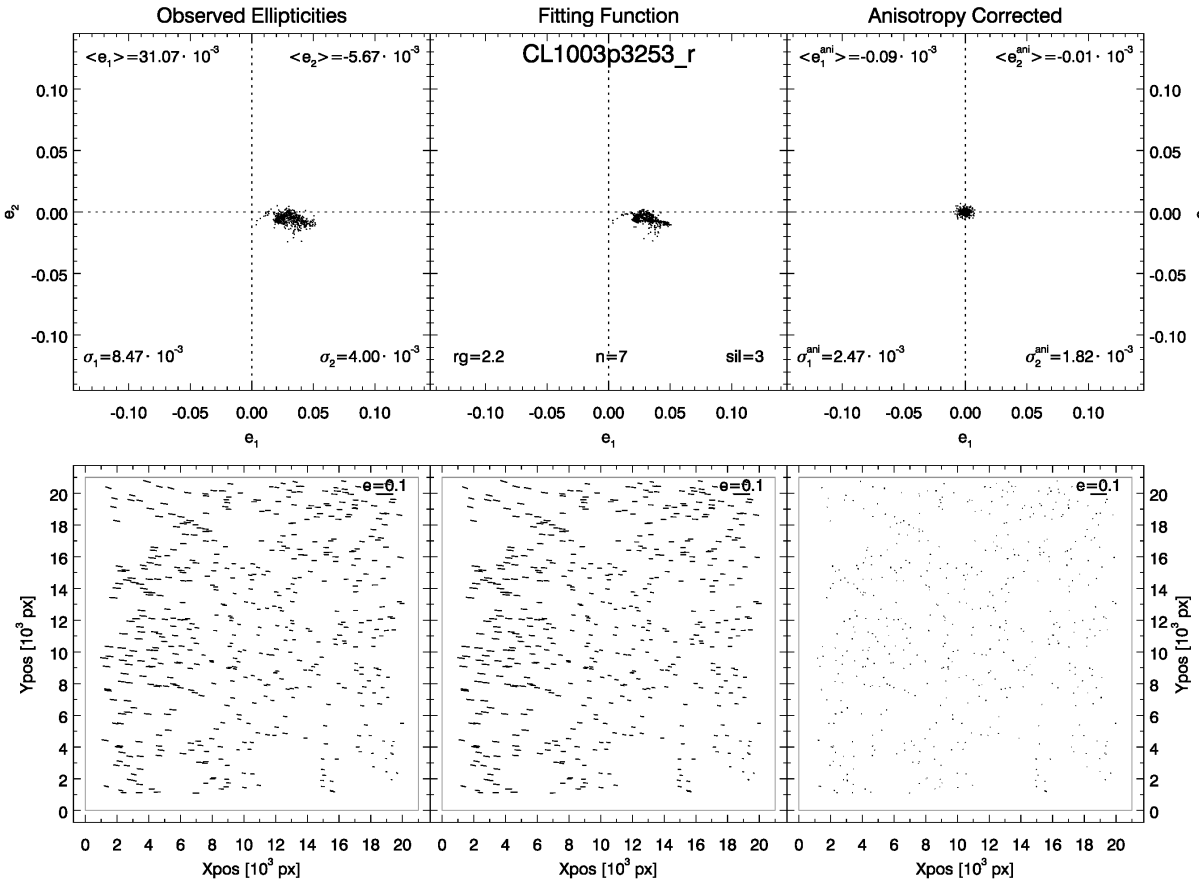


Figure 5.10: Diagnostics of the PSF anisotropy correction for CL1003+3253 using a 7th order polynomial ($d_{\rm APO} = 7$) with $r_{\rm g} = 2.2$ and stellar integration limit $\ell_{\rm SIL} = 3$. *Top panels:* ellipticity components ($e_1$,$e_2$) of all stars with the indicated mean ellipticity $\langle e \rangle$ and standard deviation $\sigma$ values before (leftmost plot) and after PSF correction (rightmost plot). *Bottom panels:* spatial distribution of the stellar anisotropies in the *MegaCam* field-of-view. *From left to right:* the original ellipticities in the field, the modeled ellipticities, the residuals after the PSF correction.

To decide the best value for $d_{\rm APO}$ and $\ell_{\rm SIL}$ we exploit once again the stars' immunity to WL effects by exploring the correlation of the stellar ellipticity. We use an $r_{\rm g} = 2.2$ as the typical PSF size for all clusters. For each combination of $d_{\rm APO}$ and $\ell_{\rm SIL}$ we produce illustrative plots as those in Figure 5.10. Then we choose the model which yields the lowest residual mean anisotropy ($\langle e^{\rm ani} \rangle$) and anisotropy dispersion ($\sigma^{\rm ani}$).

In a well-corrected shape catalog it is expected that the distortions of stars do not correlate with themselves. In Figure 5.11 we show the tests performed running `Athena`[11] (Schneider et al. 2002) for finding eventual residual correlations after correction. In the upper panel we find that, as expected, the PSF anisotropy induces some correlation in the non-corrected stellar catalog, while for our higher order polynomial corrections this correlation disappears completely.

In addition, we show the PSF-corrected stellar ellipticity vs. the uncorrected stellar ellipticity in the lower panel of Figure 5.11). As illustrated in our case, am good polynomial model should not produce a significant anticorrelation, which would be interpreted as an overfitting. Finally, for each catalog we use

[11] `http://www.cosmostat.org/software/athena/`

its best model for correcting the galaxy shapes from PSF anisotropy.

From the KSB step, all the information of all sources fainter than the brightest non-saturated point sources ($m > m^*_{\rm min}$) and larger than the stellar PSF ($\theta > 0.95\theta^*_{\rm max}$), compose our galaxy catalog.

As a final output of our KSB pipeline guided by our choices, we obtain the PSF-corrected galaxy shape catalog. Table 5.8 contains the best values for $\ell_{\rm SIL}$ and $d_{\rm APO}$ and all the thresholds of the selection in the magnitude–flux-radius plane.

Table 5.8: PSF properties of the whole subsample of eighteen clusters for which we perform the KSB analysis in this work. For the eight *MMT* clusters we adopt the values of Table 2 in I12. The objects are grouped on an instrument-basis: *IMACS*, *MegaCam*, *WFI*. $\theta^*_{\rm min}$, $\theta^*_{\rm max}$, $m^*_{\rm min}$ and $m^*_{\rm max}$ are the stellar locus parameters selected after the KSB analysis and that will be used in all the following steps. $n_{gal}$ is the galaxy density of the definitive catalog obtained after background selection (Section 6.1). Note that here we list only one catalog for CL0328−2140 and CL0405−4100 because we dropped the other two catalogs (CL0328−2140_runP and CL0405−4100_14, see details in the text) in the previous steps.

| Cluster | $\theta^*_{\rm min}$ [pixel] | $\theta^*_{\rm max}$ [pixel] | $m^*_{\rm min}$ | $m^*_{\rm max}$ | $n_{\rm gal}$ [gal/arcmin$^2$] | $d_{\rm APO}$ | $\ell_{\rm SIL}$ |
|---|---|---|---|---|---|---|---|
| CL0328−2140 | 1.23 | 1.97 | 17.8 | 24.3 | 22.37 | 7 | 5 |
| CL0333−2456 | 1.34 | 1.80 | 18.5 | 24.5 | 29.76 | 7 | 3 |
| CL0405−4100 | 2.50 | 3.30 | 17.4 | 24.5 | 21.54 | 7 | 4 |
| CL0542−4100 | 3.10 | 4.04 | 17.6 | 24.5 | 20.63 | 6 | 4 |
| CL0853+5759 | 1.59 | 2.06 | 18.4 | 24.0 | 20.96 | 7 | 3 |
| CL1003+3253 | 2.10 | 2.70 | 17.8 | 23.0 | 33.27 | 7 | 3 |
| CL1120+4318 | 1.65 | 2.05 | 17.8 | 23.0 | 38.95 | 7 | 4 |
| CL1212+2733 | 1.73 | 2.15 | 17.5 | 24.0 | 47.35 | 7 | 3 |
| CL1222+2709 | 1.60 | 2.20 | 18.2 | 23.5 | 30.43 | 7 | 4 |
| CL1312+3900 | 1.97 | 2.05 | 18.6 | 23.3 | 30.29 | 7 | 3 |
| CL1334+5031 | 1.60 | 2.25 | 17.7 | 23.2 | 32.50 | 7 | 4 |
| CL1524+0957 | 2.11 | 2.71 | 17.1 | 23.1 | 25.50 | 7 | 3 |
| CL0141−3034 | 1.69 | 2.19 | 17.0 | 23.5 | 28.05 | 5 | 3 |
| CL0302−0423 | 1.58 | 2.20 | 17.0 | 23.6 | 24.98 | 5 | 5 |
| CL0318−0302 | 1.48 | 2.16 | 16.8 | 23.5 | 20.07 | 5 | 4 |
| CL0350−3801 | 1.59 | 2.21 | 16.9 | 23.5 | 25.06 | 6 | 3 |
| CL0355−3741 | 1.73 | 2.16 | 17.0 | 23.7 | 24.60 | 7 | 3 |
| CL0522−3624 | 1.57 | 2.19 | 16.7 | 23.5 | 21.80 | 7 | 5 |

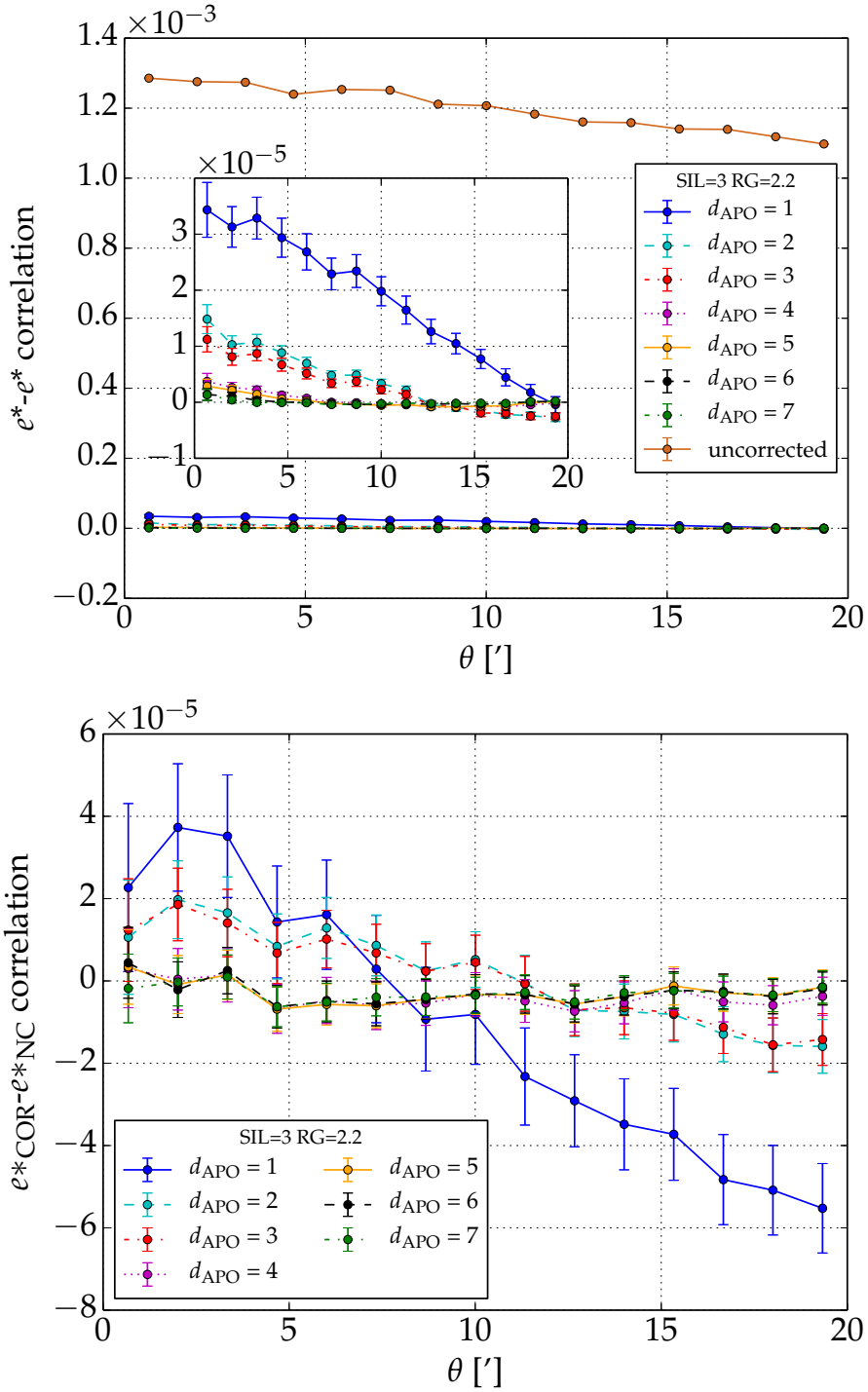


Figure 5.11: *Upper panel:* autocorrelation of the stellar ellipticity of CL1334+5031 as function of the distance from the cluster center. In the larger plot it is noticeable the difference before and after correction. In the sub-plot is shown in details the behavior of the different polynomial corrections, hinting that the highest ones correct the shear catalog in the best way. *Lower panel:* correlation between non-corrected (NC) and corrected (COR) stellar shear. Our highest polynomials do not show a negative trend, thus excluding an eventual overfitting.

CHAPTER 6

# Weak Lensing Analysis

## 6.1 Background Galaxy Selection

While direct spectroscopic or well-calibrated photometric redshifts would be the best approaches to select background sources, it has been shown that color-color diagram methods are sufficient for the same task (e.g., Israel et al. 2010; Medezinski et al. 2010; High et al. 2012; Klein 2013; Medezinski et al. 2016), consequently requiring observations in fewer filters than photometric redshifts. For the selection of the background galaxies in our lensing catalog we adopt the approach of Klein (2013, Chapter 7). This method aims to assign a lensing depth to all galaxies in a cluster field $\beta_{\rm g}$, by comparing its photometry with the photometry of a reference catalog. The lensing signal for a lens at redshift $z_{\rm d}$ is expressed in terms of the angular distance ratio

$$\frac{D_{\rm d}(z_{\rm d})D_{\rm ds}(z_{\rm s},z_{\rm d})}{D_{\rm s}(z_{\rm s})} = D_{\rm d}(z_{\rm d}) \times \beta(z_{\rm s},z_{\rm d}) \tag{6.1}$$

where the subscripts $d$ and $s$ indicate deflector and source position respectively, while $ds$ stands for the distance between them. $\beta(z_s, z_d)$ is the angular diameter distance ratio.

The key point of this method is to assign $\beta_{\rm g}$ to each single galaxy as it has a lower noise than using the mean lensing depth $\langle\beta\rangle$ of the observed cluster field. This increases the accuracy and reduces the scatter in cluster mass measurements. This is done in two steps: first, we calibrate the photometry of the sources in our catalog using a reference catalog with photometric redshifts estimated for all sources. Secondly, we apply a filtering to our calibrated KSB catalogs, selecting only objects that fall into the limits of our selection criteria in a color-color-magnitude (CCM) diagram (see details in Section 6.1.2). Then, to each of our sources, we assign a redshift and a corresponding *purity* value which indicates its level of reliability.

As we include in our final results also the *MMT* galaxy clusters, we homogenize our analysis by treating I12's KSB catalogs with the same method we use in this work.

### 6.1.1 COSMOS as Reference Catalog

Our choice of the reference catalog falls on COSMOS (Ilbert et al. 2009), which provides photometric redshifts exploiting 30 filter bands for 2 square degrees. We use COSMOS redshift distribution as proxies for the redshift probability distribution for our cluster fields.

From the COSMOS catalog we extract sub-catalogs of different combinations of three bands: $Vr^+i^+$ for 3 *IMACS*, $BVr^+$ for all *WFI* clusters, and $g^+r^+i'$ for *MegaCam*, *MMT* observations and for the *IMACS*

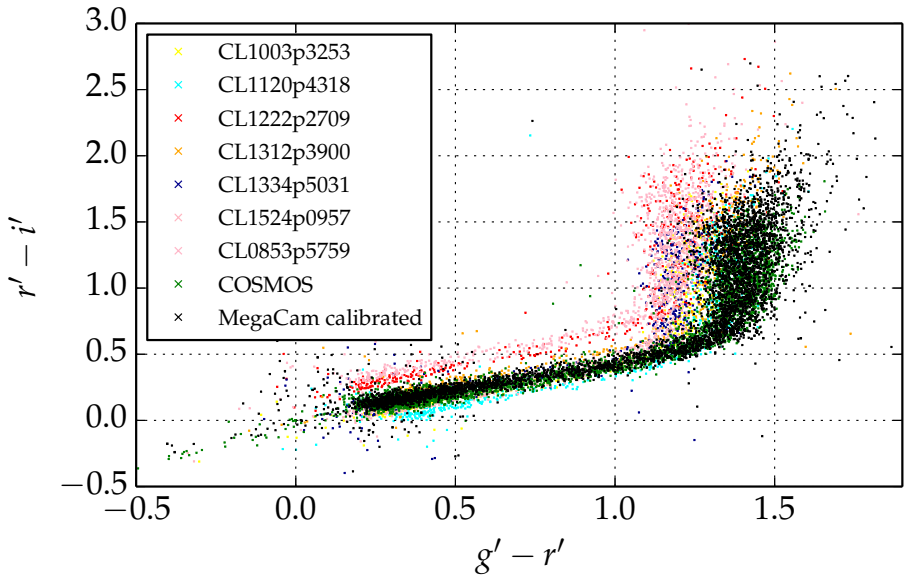


Figure 6.1: Color-color calibration for *MegaCam* clusters for which we have multi-band information. The black dots indicate the global stellar locus (including all seven fields) after matching with COSMOS (green dots). Other coloured dots indicate the stellar loci of each single cluster field before color-shifts are applied.

CL0405−4100, where $V$, $g^+$, $r^+$ and $i^+$ are Subaru filters, while $i'$ is a CFHT/*MegaCam* filter.

In the COSMOS catalog, detections in all bands have been run using a 3″ aperture photometry ($i^+_{3''}$). However, $i^+$-band observations are also available in the `MAG_AUTO` photometry: $i^+_{\rm AUTO}$. Since we want to precisely compare our lensing band `MAG_AUTO` photometry of our fields with the $r^+_{\rm AUTO}$ photometry from the reference catalog, we compute $r^+_{\rm AUTO}$ by using:

$$r^+_{\rm AUTO} = r^+_{3''} - i^+_{3''} + i^+_{\rm AUTO} \quad . \tag{6.2}$$

From each sub-catalog we construct two other catalogs, separating stars from galaxies. The former is useful for the photometric calibration by means of the stellar locus regression method, and the latter for assigning the redshifts (Section 6.1.2). All catalogs do not include objects which in COSMOS are flagged and undergo a cut in the lensing band magnitude limit at 22.5.

The COSMOS catalog provides solid photometric redshifts for $i^+_{\rm AUTO} > 25.0$, a value that corresponds to the typical magnitude limit of our observations. We correct for the mismatch between the photometric system used by *IMACS* and *WFI* (*Vega*) and the one used by COSMOS and all instruments we used for this work (*AB*). extinction using the respective Schlegel et al. (1998) map values.

COSMOS has a small volume probed at low-$z$: it does not include clusters or massive groups below $z = 0.15$. As shown by Ziparo et al. (2015), this could introduce a small bias on the single galaxy lensing depth estimate $\beta_{\rm g}$ and red sequence finding, but the mass estimates of high-$z$ clusters as those in the *400dCS* are not affected.

### 6.1.2 Color-Color Calibration and Redshift Allocation

As in High et al. (2009), we apply a stellar locus regression method in the color-color (CC) plane: $V - R$ vs. $V - B$ for *WFI*, $R - I$ vs. $V - R$ for 3 *IMACS* clusters and $r' - i'$ vs. $g' - r'$ for all the others. Using

plots such as Figure 5.5 as a tool for selecting stars on the stellar locus feature, we create star catalogs from our KSB catalogs. The star disposition on the CC plane shows a distinct shape, which we exploit for calibrating the photometry of our cluster fields with COSMOS. We show in Figure 6.1 the case of the 7 *MegaCam* clusters which are covered by at least 3 filter bands. Both the refence star catalog and the star catalog of each cluster field are investigated for prominent features at the center, the low-, the high-end of the $g' - r'$ color, so that matching them gives us a shift and a stretch in the CC plane. Moving the cluster field stellar locus on top of the COSMOS data makes it possible to have a reliable comparison of the two catalog in the CC plane.

Subsequently, we add the magnitude of the lensing band as a third dimension, thus considering a color-color-magnitude space. In this CCM space, on each galaxy of our catalog, we center an elliptic cylinder whose height is given by the lensing band magnitude uncertainties and base (in the CC plane) is given by the color uncertainties. elliptic cylinder centered on a catalog galaxy, and having its height given by the lensing band magnitude uncertainties and the base (in the CC plane) given by the color uncertainties. The mean $D_{\rm ds}/D_{\rm s}$ of all the galaxies of the COSMOS catalog which are included in this cylinder becomes the $\beta_{\rm g}$ of our galaxy. For having a good statistics, we set the minimum number of reference galaxies included in the cylinder to 50. With this approach, each galaxy in the cluster field with good color estimates, obtains its own lensing depth.

Similarly, to each cluster field galaxy we assign a *purity* value $p$ which is estimated as the ratio between the number of COSMOS sources with $z_{\rm phot} > z_{\rm d}$ and the overall number of galaxies which fall into the elliptic cylinder regardless of their redshift.

To obtain a clean lensing catalog we separate background from foreground galaxies by including in our lensing catalog only galaxies at higher redshift than the cluster. For each cluster we define a $\beta_{\rm cut}$, i.e. a threshold for the highest $\beta_{\rm g}$ to be incorporated in the lensing catalog. We determine $\beta_{\rm cut}$ with the help of signal-to-noise maps, as shown in Section 6.1.3.

### 6.1.3 Signal-to-Noise Maps and Lensing Signal

To assess the cluster lensing signal and, at the same time, to enhance the goodness of the background galaxies selection, we maximize a weighted adaptation of the *S-statistics*, i.e. the discretized version of the of the aperture mass estimator proposed by Schneider (1996). This is described under the form of a signal-to-noise ratio (S/N):

$$S(\vec{\theta_{\rm c}};\theta_{\rm out}) = \frac{\sqrt{2}}{\sigma^*_\epsilon}\frac{\Sigma_j \epsilon_{{\rm t},j} F(|\epsilon_{{\rm t},j}|) Q_j(|\vec{\theta_j} - \vec{\theta_{\rm c}}|/\theta_{\rm out})}{\sqrt{\Sigma_j Q_j^2(|\vec{\theta_j} - \vec{\theta_{\rm c}}|/\theta_{\rm out})}} \quad , \tag{6.3}$$

where the weighted source intrinsic ellipticity intended as a noise term is

$$\sigma^*_\epsilon = \sqrt{\frac{1}{N}\Sigma_j |\epsilon_{{\rm t},j}|^2 F^2(|\epsilon_{{\rm t},j}|)} \quad , \tag{6.4}$$

while $Q_j = (|\vec{\theta_j} - \vec{\theta_{\rm c}}|/\theta_{\rm out})$ is the filter function of (Schirmer et al. 2007) with outer radius $\theta_{\rm out}$, and $\epsilon_{\rm t,j} = {\rm Re}[\epsilon\, {\rm e}^{-2{\rm i}\phi}]$ is the tangential component of the ellipticity of the galaxy at position $\vec{\theta_j}$ which has a phase angle $\phi$ with respect to the point $\vec{\theta_{\rm c}}$. Unlike I10 and I12, we do not apply the cut $\max(|e|) = 0.8$ to our ellipicity distribution, but we weight the S/N by $F(|\epsilon_{{\rm t},j}|)$, a function which models the distribution of of the ellipticities in each field. In this way, although we expect a sharp decline in the lensing signal at very high ellipticities (because they carry more noise), they will be underweighted but still included in our lensing catalog.

For exploring the S/N around the cluster position, when possible, we consider only the galaxies within a few arcminutes around the cluster center. The S/N peak is usually found close to the *Chandra* X-ray peak when there are no foreground clusters in the vicinity of the analyzed cluster. neighboring clusters within 15′ from the considered objects. The presence of big masked areas, e.g. near bright stars, can influence the determination of our S/N maps. For each catalog, we vary the $\beta_{\rm cut}$, $p$ and $\theta_{\rm out}$ thresholds one at the time while keeping the others fixed.

Moreover, as we want to avoid sources brighter than the stars and with the size smaller than them (see Figure 5.5), we apply at the same time the cuts listed in Table 5.8 (from the second to the fourth column) based on the stellar locus choice discussed in Section 5.2.1. In particular, exploring $\beta_{\rm cut}$ and the minimum of *purity* singularly for each field, shows us how different cuts affect the S/N at the cluster position. We pick the thresholds which are a good compromise between the central S/N and the number of galaxies with $\beta > \beta_{\rm cut}$ and $purity > min(purity)$.

Furthermore, we use the S-statistics maps as sanity checks for our lensing catalogs. In addition to the usual map, we compute the S-statistics for the complementary lensing catalog, veryfing that it does not contribute to the signal or does not present strong peaks.

#### Special cases: CL0328−2140 and CL0542−4100

The observations in the I-band for CL0328−2140 (Table 5.2) too shallow, thus letting the S/N drop to a non-detection level. In this case, we decide to use only the lensing band (i.e., R) catalog which, after applying a magnitude cut (as done in I12), shows a strong signal at the cluster coordinates.

Furhtermore, despite exploring different thresholds for the S/N maximization in the case of CL0542−4100, we cannot recover a strong signal at its postion. Trying a single-band approach does not yield better results, as well. Therefore we treat it as a non-detection ($S/N < 3\sigma$) and we exclude this cluster field from the following steps of our analysis, reducing the sample to a number of 25 galaxy clusters.

### 6.1.4 Mass Bias Investigations

#### S/N-Dependent Shear Bias

Consistent with the work of I12, as we lack of ad hoc shape measurement simulations, we multiply our shear estimates by the fiducial global shear calibration factor ($f_0 = 1.08$) from Hartlap et al. (2009). Furthermore, since the depth of observations taken with different instruments varies a lot, it is needed to understand more in detail how the shear depends on the S/N of the catalog sources, determined by the KSB+ pipeline.

For this purpose, we estimate the mass of all clusters (with the method described in Section 6.2) using different cuts on the minimum S/N of galaxy detection and we show in Figure 6.2 (top-left panel) the respective $r_{200}$ normalized by the median of the $r_{200}$ values of a given cluster at all the min(S/N). The median over all clusters and its standard deviation are represented by the thick black line. In the top-right plot of Figure 6.2 we isolate the median and show the standard error of its mean (red line and red errorbars) to have a visual aid for the choice of the threshold for the S/N. For our conservative model we pick min(S/N) = 5.25, as this implies small scatter, and from that value on the trend behaves consistent with zero bias.

#### Bias from $\beta_{\rm cut}$ choice

As described in Section 6.1, we assign a $\beta_{\rm cut}$ value to all galaxies of our lensing catalog to separate between background sources and cluster galaxies. Taking a common $\beta_{\rm cut}$ for all clusters, e.g. the

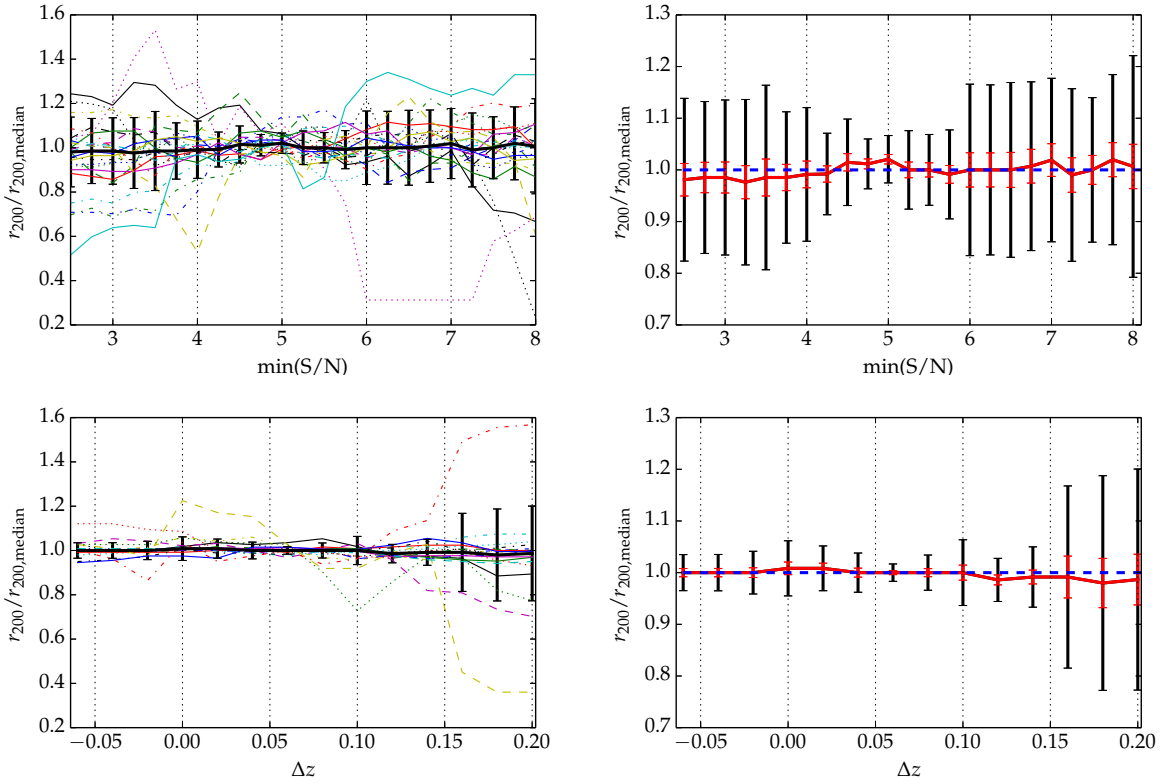


Figure 6.2: Investigation on the mass bias for the whole sample, considering $\Delta z$ (*lower panels*) and the minimum of the galaxy detection S/N (*upper panels*). *Left panels:* the thin colored lines describe the normalized $r_{200}$ for all clusters, while the thick black line indicates the median of the normalized $r_{200}$ for all clusters at each $\Delta z$ (or min(S/N)) step. We consider all 25 clusters for the investigation of min(S/N), while for the $\Delta z$ case, are excluded the 6 single-band clusters. The errorbars indicate the standard error of the median. *Right panels:* the median and the standard deviation of the left panels are here reproduced alone, by the red line and the black errorbars, respectively. The small red errorbars indicate the standard error from the mean. The dashed blue line represents a constant fit at the value of $\Delta z = 0.04$ for the bottom panel, and min(S/N)=5.25 for the top one, which we adopt for our conservative model.

mean of all the S/N-weighted $\beta_{\mathrm{cut}}$ of the clusters, would introduce a shear signal dilution in the case of $\beta_{\mathrm{cut,mean}} < \beta_{\mathrm{cut}}$. On the other hand, for $\beta_{\mathrm{cut,mean}} > \beta_{\mathrm{cut}}$, it would push down the cluster S-statistics as the catalog becomes more pure but smaller. Consequently, the $\beta_{\mathrm{cut}}$ threshold holds the balance of power between a clean-but-smaller and larger-but-diluted catalog.

With the same method used for the S/N-dependent shear bias (Section 6.1.4) in Figure 6.2, using the just chosen $S/N = 5.25$ threshold, we study the normalized $r_{200}$ behavior with different thresholds for $\beta_{\mathrm{cut}}$. We conveniently convert $\beta_{\mathrm{cut}}$ to a $z_{\mathrm{cut}}$ for each cluster and then calculate $\beta_{\mathrm{cut}} + \Delta\beta$ in terms of $z_{\mathrm{cut}} + \Delta z$, where $\Delta z$ is the shift we apply uniformly to all the single cluster $z_{\mathrm{cut}}$ values. As shown in the bottom panels of Figure 6.2, the normalized $r_{200}$ is overestimated by 1% and 0.5% at $\Delta z = 0$ and $\Delta z = 0.02$ respectively. Thus, for our conservative model, we pick the value $\Delta z = 0.04$.

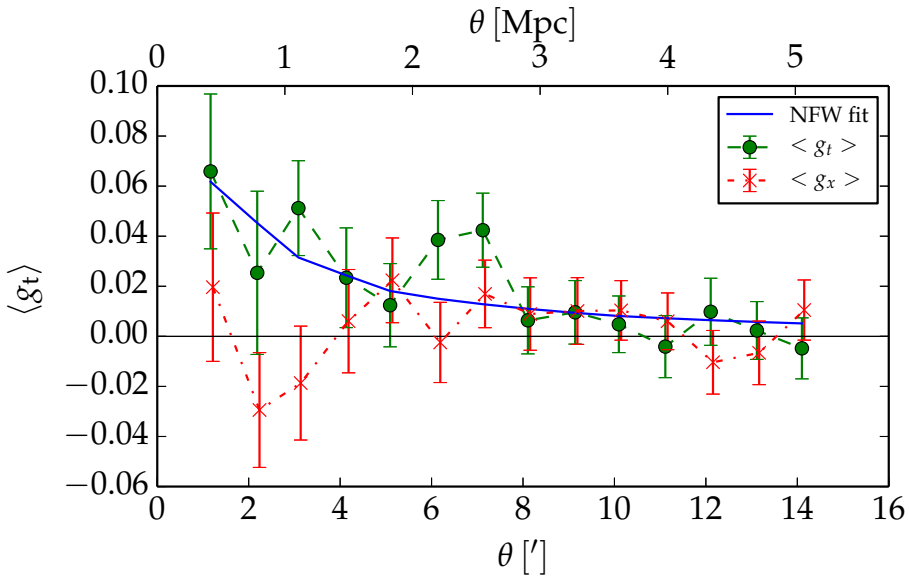


Figure 6.3: Shear profile fitting with an NFW model (blue solid line) for the cluster field of CL1003+3253. Only for illustration purpose here we use a binning of 1 arcminute. The green cirles indicate the values for the reduced tangential shear, while the red crosses indicate the cross component of the reduced shear.

## 6.2 Mass Estimates

Weak lensing mass reconstruction relying only on the shear information suffers from a limitation: the surface mass density can only be constrained up to a constant. This problem is known as the mass-sheet degeneracy. To break this degeneracy, in our mass estimates, we calculate the reduced shear at each galaxy position ($g(\theta; r_{200}, c_{\rm NFW})$) and fit to it the halo-model, well-described by a Navarro-Frenk-White (NFW) profile (Navarro et al. 1997). Furthermore, we use the Wright & Brainerd (2000) expressions for the lensing quantities of the NFW halo. A regular grid of values in the ($c$, $r_{200}$) plane is explored to find the best-fit parameters that minimize the $\chi^2$ function:

$$\chi^2 = \sum_i^N \frac{\left|g_i(\theta_i; r_{200}, c_{\rm NFW}) - \tilde{\epsilon}_{{\rm t},i}\right|^2}{\tilde{\sigma}_i^2(\theta_i)\left(1 - \left|g_i(\theta_i; r_{200}, c_{\rm NFW})\right|^2\right)^2} \quad . \tag{6.5}$$

To preserve the weak lensing assumption and avoid the strong regime, we exclude the central region of the cluster from the NFW fit. Our fitting range extends from 0.2 to 5.0 Mpc from the cluster center determined by the *Chandra* X-ray observations (the coordinates of all centers are listed in the Tables 5.2, 5.7, 5.5 and 6.1). Note that for CL0333−2456 and CL0542−2456 we are limited by the small angular coverage as some of the observations were taken using the f/4 position (see Tables 5.2 and 5.3). Thus, for those two objects we restrict the outer limit of the fitting range to 3 Mpc and 3.5 Mpc respectively.

In Table 6.2 we report the $M_{200}$ masses with the relative best-fit values of the radius $r_{200}$ and the concentration parameter $c_{\rm B13}$, obtained using the Bhattacharya et al. (2013) concentration-mass relation (see Section 7.1). All the values at $r_{200}$ are also converted to $r_{500}$ for a better comparison with the X-ray results (Section 7.1).

For the 6 single-band clusters (see Table 6.2) for which it is impossible to recover $\beta_g$ for the individual

Table 6.1: Centers for the *MMT* clusters from X-ray *Chandra* observations. Further details about the data reduction of these clusters and their *ROSAT* centers can be found in (Israel et al. 2012).

| Cluster | $\alpha$ (J2000) | $\delta$ (J2000) | Redshift |
|---|---|---|---|
| CL0030+2618 | 00:30:34.275 | +26:18:07.36 | 0.50 |
| CL0159+0030 | 01:59:17.203 | +00:30:14.08 | 0.39 |
| CL0230+1836 | 02:30:26.271 | +18:36:29.69 | 0.80 |
| CL0809+2811 | 08:09:39.901 | +28:11:59.80 | 0.40 |
| CL1357+6232 | 13:57:16.461 | +62:32:49.35 | 0.53 |
| CL1416+4446 | 14:16:27.823 | +44:46:45.76 | 0.40 |
| CL1641+4001 | 16:41:53.511 | +40:01:43.66 | 0.46 |
| CL1701+6414 | 17:01:23.852 | +64:14:11.94 | 0.45 |

galaxies, we determine the $\langle\beta\rangle$, by fitting the redshift distribution of our reference catalog following the method described in I10. For consistency with the previous steps in our work, we use the COSMOS catalog.

In Figure 6.3 a typical reduced shear profile is shown. While the tangential shear is well fitted by the NFW model corresponding to the best-fit values of $r_{200}$ and $c_{\rm NFW}$, the cross component of the shear is consistent with zero. As gravitational lensing is not expected to create cross components, a $g_{\rm x}$ close to zero throughout the radial range represents a further confirmation that our lensing catalogs are clean.

Four clusters in our sample (cross symbols in Table 6.2) show a very flat shear profile, due to a visually confirmed presence of a neighboring cluster. For those objects, we explore the 4-dimensional parameter space for $c_{\rm m,NFW}$, $r_{\rm m,200}$, $c_{\rm s,NFW}$ and $r_{\rm s,200}$ (with the subscripts $m$ and $s$ indicating respectively the main and the secondary cluster) in the ranges that go from 1 to 17 for $c_{NFW}$ and from 0.5 to 2.9 for $r_{200}$. As in I12 we consider the shear components of two close clusters are additive, so we use a modified version of the $\chi^2$ of Eq. 6.5 where $g(\theta; r_{200}, c_{\rm NFW})$ becomes $g_{{\rm add},\alpha}(\tilde{\theta}) = {\rm g}_{{\rm m},\alpha}(\tilde{\theta}; r_{\rm m,200}, c_{\rm m,NFW}) + {\rm g}_{{\rm s},\alpha}(\tilde{\theta}; r_{\rm s,200}, c_{\rm s,NFW})$.

The cluster field of CL0328−2140 ($z = 0.59$) shows two S-statistics peaks, with the strongest being $\sim 5\farcm5$ far from the X-ray center of the *400d* cluster. Figure 6.4 shows both the S-statistics map and the optical image. It is striking that those detections are two distinct clusters. CL0328−2140 (on the right in the figures) has a the lowest significance of $3.4\sigma$. The neighboring cluster behind a saturated star, has a S/N of $4\sigma$ and shows strong lensing features. Nevertheless, it does not appear in any public catalogs. Its larger extent in the S/N map could be due to the big masks placed on the two closeby saturated stars, well visible in the optical image (lower panel, Figure 6.4).

From archival *Chandra* X-ray images (see Appendix C.6) we find that the second cluster is brighter than CL0328−2140 at high energy. In order to fit the shear profile of the CL0328−2140 field with a double NFW profile, we first recover the redshift of the neighbor with a Markov chain Monte Carlo (MCMC) method. The results show that the secondary cluster has the same redshift of CL0328−2140 within $2\sigma$ confidence level.

### 6.2.1 Mass-Concentration Relation

Due to the low density of background galaxies in the lensing catalogs, it is not possible to properly constrain the concentration parameter through cluster weak lensing. The little constraining power WL data have, comes from source galaxies with a small projected separation from the cluster center. For these reasons, we prefer to fix $c_{\rm NFW}$ to the value derived from the Bhattacharya et al. (2013) mass-concentration

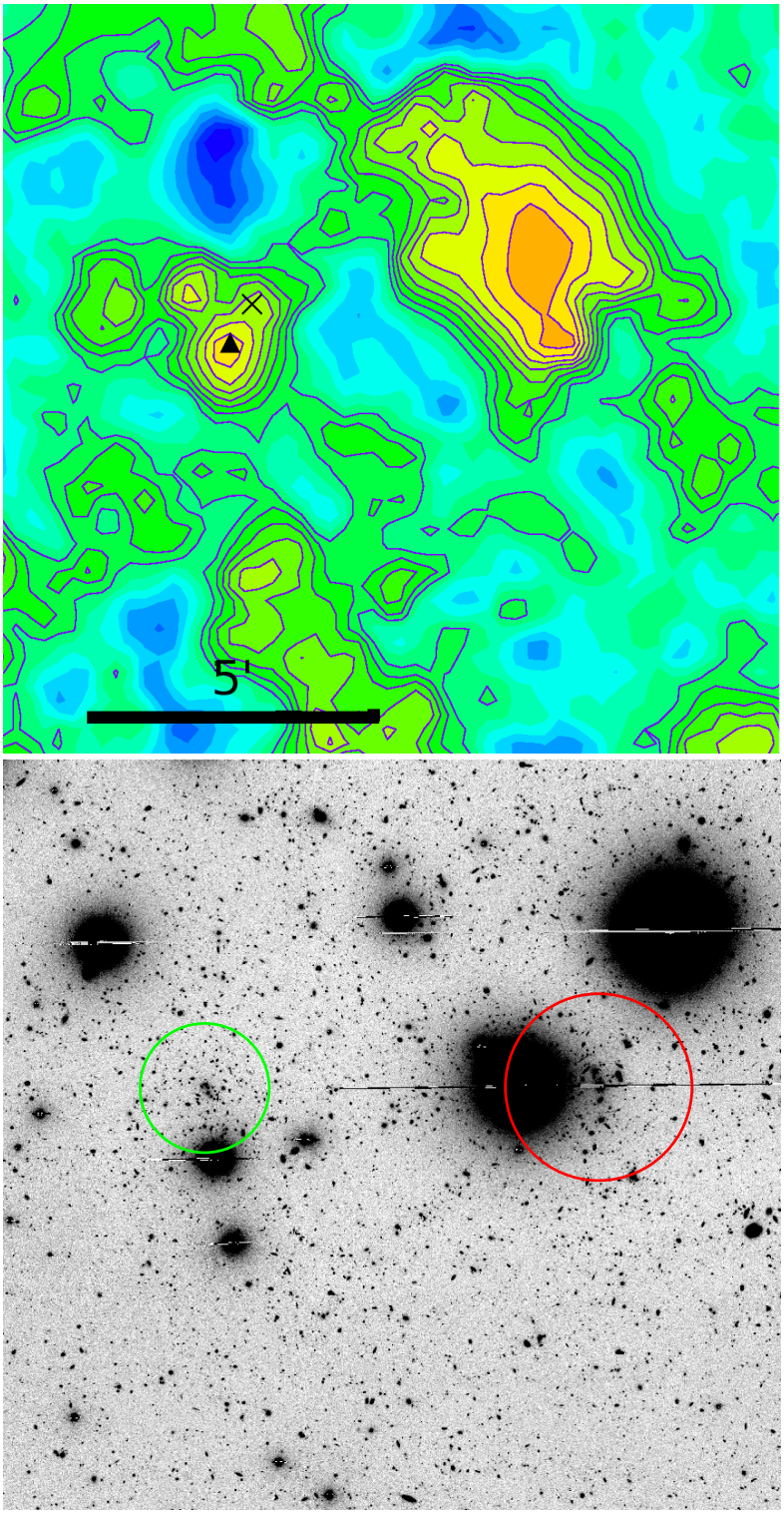


Figure 6.4: Detail of the cluster field of CL0328−2140. The S-statistics map (*upper panel* shows two S/N peaks separated by ~5′.5. The lowest peak (3.4$\sigma$, indicated by the black triangle) is close to the position of the X-ray peak of CL0328−2140 (black cross). The second peak has a higher significance (4$\sigma$). The optical image in inverted colors of the *lower panel* shows the position of the two clusters. The green circle denotes CL0328−2140, while the red one indicates the position of its neighbor. A further zoom into the second cluster, shows strong lensing features.

relation. The Bhattacharya et al. (2013) relation we use is obtained with their full sample, as a function of the *peak height parameter* $\nu$ and it is defined as:

$$c_{200,\mathrm{B13}}(\nu) = D(z)^{0.5} 5.9 \nu^{-0.35} \quad , \tag{6.6}$$

where $D(z)$ is the $\Lambda CDM$ linear growth factor and $\nu = \delta_c(z)\sigma(M,z)$ with $\delta_c(z)$ being the collapse threshold in the linear theory of structure formation, and $\sigma(M,z)$ is the variance of the matter fluctuations over the scale $\propto M^{1/3}$ at redshift $z$. In their simulations the distribution of the concentrations has a Gaussian shape with variance $\sigma_c = 0.33 c_{200,\mathrm{B13}}$.

Following I12, we apply to the values of $\Delta\chi^2$ of all clusters a Gaussian prior, marginalizing over the $c_{\mathrm{NFW}}$ direction. All values are reported in Table 6.2, including those of the non-detection CL0504−4100, despite we do not use this cluster in the computation of the scaling relations.

Table 6.2: Masses of all 26 clusters obtained using the concentration–mass relation by Bhattacharya et al. (2013), with statistical errors from the computation of the $\Delta\chi^2$ on the grid in $r$ and $c_{\rm NFW}$. The symbols indicate: ★ single-band clusters; ✠ Double-NFW clusters; ◇ non-detection (discarded from the scaling relation studies).

| Cluster | $z$ | $r_{200}$ [Mpc] | $c_{\rm NFW,200}$ | $M_{200}$ [$10^{14}\mathrm{M}_\odot$] | $r_{500}$ [Mpc] | $c_{\rm NFW,500}$ | $M_{200}$ [$10^{14}\mathrm{M}_\odot$] |
|---|---|---|---|---|---|---|---|
| CL0328−2140✠★ | 0.59 | $0.78^{+0.25}_{-0.36}$ | $3.70^{+1.22}_{-1.22}$ | $1.03^{+1.34}_{-0.87}$ | $0.51^{+0.16}_{-0.23}$ | $2.40^{+0.85}_{-0.85}$ | $0.70^{+0.91}_{-0.59}$ |
| CL0333−2456 | 0.48 | $1.16^{+0.25}_{-0.31}$ | $3.55^{+1.17}_{-1.17}$ | $2.97^{2.37}_{-1.80}$ | $0.75^{+0.16}_{-0.20}$ | $2.29^{+0.81}_{-0.81}$ | $2.00^{+1.59}_{-1.21}$ |
| CL0405−4100 | 0.69 | $1.72^{+0.31}_{-0.38}$ | $2.90^{+0.96}_{-0.96}$ | $12.45^{+8.02}_{-6.56}$ | $1.09^{+0.20}_{-0.24}$ | $1.84^{+0.66}_{-0.66}$ | $7.96^{+5.13}_{-4.20}$ |
| CL0542−4100◇ | 0.64 | $0.50^{+0.54}_{-0.30}$ | $3.95^{+1.30}_{-1.30}$ | $0.29^{+2.30}_{-0.27}$ | $0.33^{+0.35}_{-0.20}$ | $2.57^{+0.91}_{-0.91}$ | $0.20^{+1.60}_{-0.19}$ |
| CL0853+5759★ | 0.47 | $1.18^{+0.19}_{-0.22}$ | $3.60^{+1.19}_{-1.19}$ | $3.09^{+1.75}_{-1.43}$ | $0.76^{+0.12}_{-0.14}$ | $2.33^{+0.82}_{-0.82}$ | $2.09^{+1.18}_{-0.96}$ |
| CL1003+3253 | 0.42 | $1.48^{+0.17}_{-0.18}$ | $3.45^{+1.14}_{-1.14}$ | $5.76^{+2.22}_{-1.86}$ | $0.95^{+0.11}_{-0.12}$ | $2.22^{+0.79}_{-0.79}$ | $3.85^{+1.48}_{-1.24}$ |
| CL1120+4318 | 0.60 | $1.25^{+0.18}_{-0.21}$ | $3.30^{+1.09}_{-1.09}$ | $4.29^{+2.13}_{-1.82}$ | $0.80^{+0.12}_{-0.13}$ | $2.12^{+0.75}_{-0.75}$ | $2.84^{+1.41}_{-1.20}$ |
| CL1212+2733★ | 0.35 | $1.56^{+0.14}_{-0.15}$ | $3.55^{+1.17}_{-1.17}$ | $6.22^{+1.83}_{-1.63}$ | $1.01^{+0.09}_{-0.10}$ | $2.29^{+0.81}_{-0.81}$ | $4.19^{+1.23}_{-1.10}$ |
| CL1222+2709 | 0.47 | $0.94^{+0.23}_{-0.32}$ | $3.80^{+1.25}_{-1.25}$ | $1.56^{+1.45}_{-1.12}$ | $0.61^{+0.15}_{-0.21}$ | $2.47^{+0.87}_{-0.87}$ | $1.07^{+0.99}_{-0.76}$ |
| CL1312+3900✠ | 0.40 | $1.14^{+0.15}_{-0.17}$ | $3.75^{+1.24}_{-1.24}$ | $2.57^{+1.15}_{-0.99}$ | $0.74^{+0.10}_{-0.11}$ | $2.43^{+0.86}_{-0.86}$ | $1.75^{+0.79}_{-0.67}$ |
| CL1334+5031 | 0.62 | $1.53^{+0.20}_{-0.24}$ | $3.10^{+1.02}_{-1.02}$ | $8.06^{+3.59}_{-3.23}$ | $0.98^{+0.13}_{-0.15}$ | $1.98^{+0.70}_{-0.70}$ | $5.24^{+2.34}_{-2.10}$ |
| CL1524+0957 | 0.52 | $1.78^{+0.20}_{-0.22}$ | $3.15^{+1.04}_{-1.04}$ | $11.26^{+4.24}_{-3.68}$ | $1.14^{+0.13}_{-0.14}$ | $2.01^{+0.72}_{-0.72}$ | $7.36^{+2.77}_{-2.41}$ |
| CL0030+2618 | 0.50 | $1.33^{+0.16}_{-0.18}$ | $3.40^{+1.12}_{-1.12}$ | $4.59^{+1.86}_{-1.62}$ | $0.86^{+0.10}_{-0.11}$ | $2.19^{+0.78}_{-0.78}$ | $3.06^{+1.24}_{-1.08}$ |
| CL0159+0030 | 0.39 | $1.40^{+0.24}_{-0.30}$ | $3.60^{+1.19}_{-1.19}$ | $4.70^{+2.86}_{-2.42}$ | $0.91^{+0.16}_{-0.19}$ | $2.33^{+0.82}_{-0.82}$ | $3.18^{+1.93}_{-1.64}$ |
| CL0230+1836 | 0.80 | $1.16^{+0.36}_{-0.54}$ | $3.05^{+1.01}_{-1.01}$ | $4.35^{+5.44}_{-3.69}$ | $0.74^{+0.23}_{-0.34}$ | $1.94^{+0.70}_{-0.69}$ | $2.82^{+3.53}_{-2.39}$ |
| CL0809+2811 | 0.40 | $1.93^{+0.20}_{-0.21}$ | $3.30^{+1.09}_{-1.09}$ | $12.47^{+4.29}_{-3.65}$ | $1.24^{+0.13}_{-0.13}$ | $2.12^{+0.75}_{-0.75}$ | $8.25^{+2.84}_{-2.41}$ |
| CL1357+6232★ | 0.53 | $1.05^{+0.24}_{-0.32}$ | $3.55^{+1.71}_{-1.71}$ | $2.34^{+2.00}_{-1.55}$ | $0.68^{+0.15}_{-0.21}$ | $2.29^{+0.81}_{-0.81}$ | $1.57^{+1.35}_{-1.05}$ |
| CL1416+4446★ | 0.40 | $1.13^{+0.17}_{-0.20}$ | $3.75^{+1.24}_{-1.24}$ | $2.50^{+1.31}_{-1.11}$ | $0.73^{+0.11}_{-0.13}$ | $2.43^{+0.86}_{-0.86}$ | $1.71^{+0.89}_{-0.76}$ |
| CL1641+4001★ | 0.46 | $1.02^{+0.26}_{-0.36}$ | $3.70^{+1.22}_{-1.22}$ | $1.97^{+1.93}_{-1.44}$ | $0.66^{+0.17}_{-0.23}$ | $2.40^{+0.85}_{-0.85}$ | $1.34^{+1,31}_{-0.98}$ |
| CL1701+6414✠★ | 0.45 | $0.89^{+0.20}_{-0.26}$ | $3.85^{+1.27}_{-1.27}$ | $1.30^{+1.09}_{-0.84}$ | $0.58^{+0.13}_{-0.17}$ | $2.50^{+0.88}_{-0.88}$ | $0.89^{+0.74}_{-0.58}$ |
| CL0141−3034 | 0.44 | $0.64^{+0.31}_{-0.44}$ | $4.15^{+1.37}_{-1.37}$ | $0.48^{+1.08}_{-0.46}$ | $0.42^{+0.20}_{-0.29}$ | $2.71^{+0.95}_{-0.95}$ | $0.33^{+0.75}_{-0.32}$ |
| CL0302−0423 | 0.35 | $1.29^{+0.20}_{-0.22}$ | $3.75^{+1.24}_{-1.24}$ | $3.52^{+1.90}_{-1.51}$ | $0.84^{+0.13}_{-0.14}$ | $2.43^{+0.86}_{-0.86}$ | $2.40^{+1.30}_{-1.03}$ |
| CL0318−0302✠ | 0.37 | $1.35^{+0.24}_{-0.28}$ | $3.65^{+1.20}_{-1.20}$ | $4.12^{+2.61}_{-2.07}$ | $0.87^{+0.16}_{-0.18}$ | $2.36^{+0.83}_{-0.83}$ | $2.79^{+1.77}_{-1.40}$ |
| CL0350−3801 | 0.36 | $1.02^{+0.25}_{-0.33}$ | $3.95^{+1.30}_{-1.30}$ | $1.76^{+1.64}_{-1.21}$ | $0.66^{+0.16}_{-0.21}$ | $2.57^{+0.91}_{-0.91}$ | $1.21^{+1.13}_{-0.84}$ |
| CL0355−3741 | 0.47 | $1.20^{+0.13}_{-0.15}$ | $3.55^{+1.17}_{-1.17}$ | $3.25^{+1.91}_{-1.59}$ | $0.77^{+0.13}_{-0.15}$ | $2.29^{+0.81}_{-0.81}$ | $2.19^{+1.29}_{-1.07}$ |
| CL0522−3624 | 0.47 | $0.79^{+0.35}_{-0.59}$ | $3.95^{+1.30}_{-1.30}$ | $0.93^{+1.86}_{-0.91}$ | $0.51^{+0.23}_{-0.38}$ | $2.57^{+0.91}_{-0.91}$ | $0.64^{+1.29}_{-0.63}$ |

CHAPTER 7

# Scaling Laws: X-ray vs. Weak Lensing

## 7.1 WL–X-ray Scaling Relations

Accurate cosmology through the cluster mass function relies on accurate cluster of galaxies mass estimates. Those objects have the advantage of showing different physical features at various wavelengths, which allows us to cross-check diverse mass proxies for whole samples. In particular, the complete, homogeneous and flux-limited sample *400dCS* profits from an exhaustive study in the X-ray band (V09), which resulted in important cosmological constraints based on galaxy cluster mass estimates (Vikhlinin

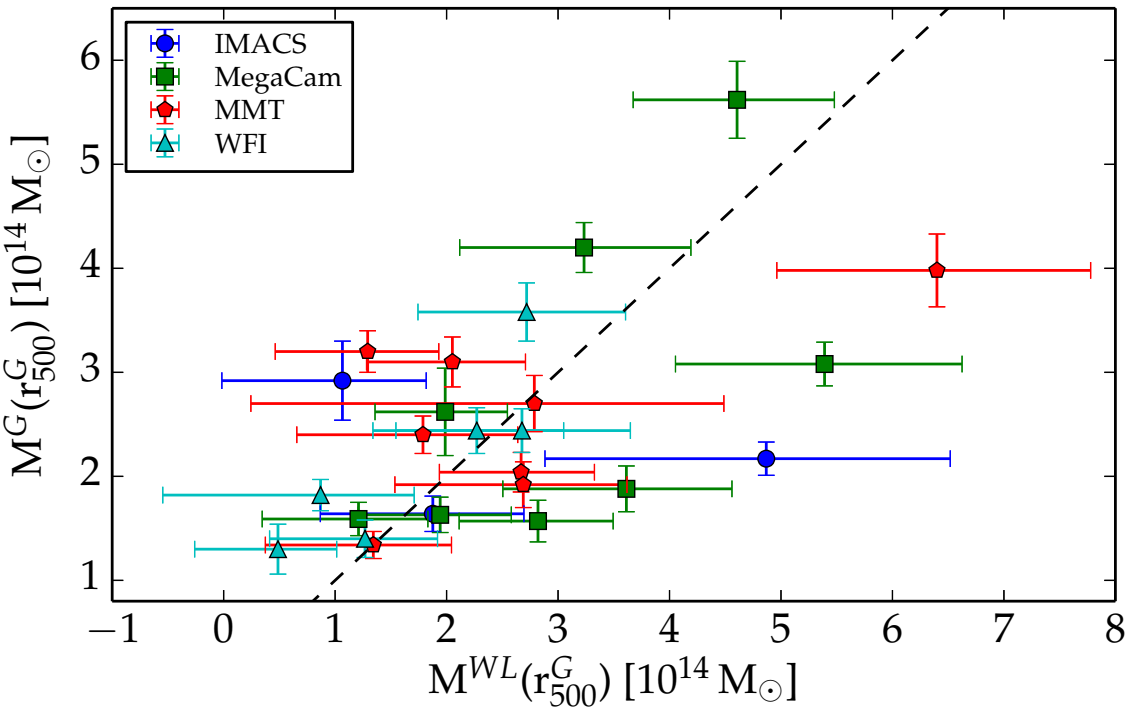


Figure 7.1: Comparison between X-ray total mass estimated from the integrated gas mass from V09 and our weak lensing mass measurements. The dashed line is the identity line.

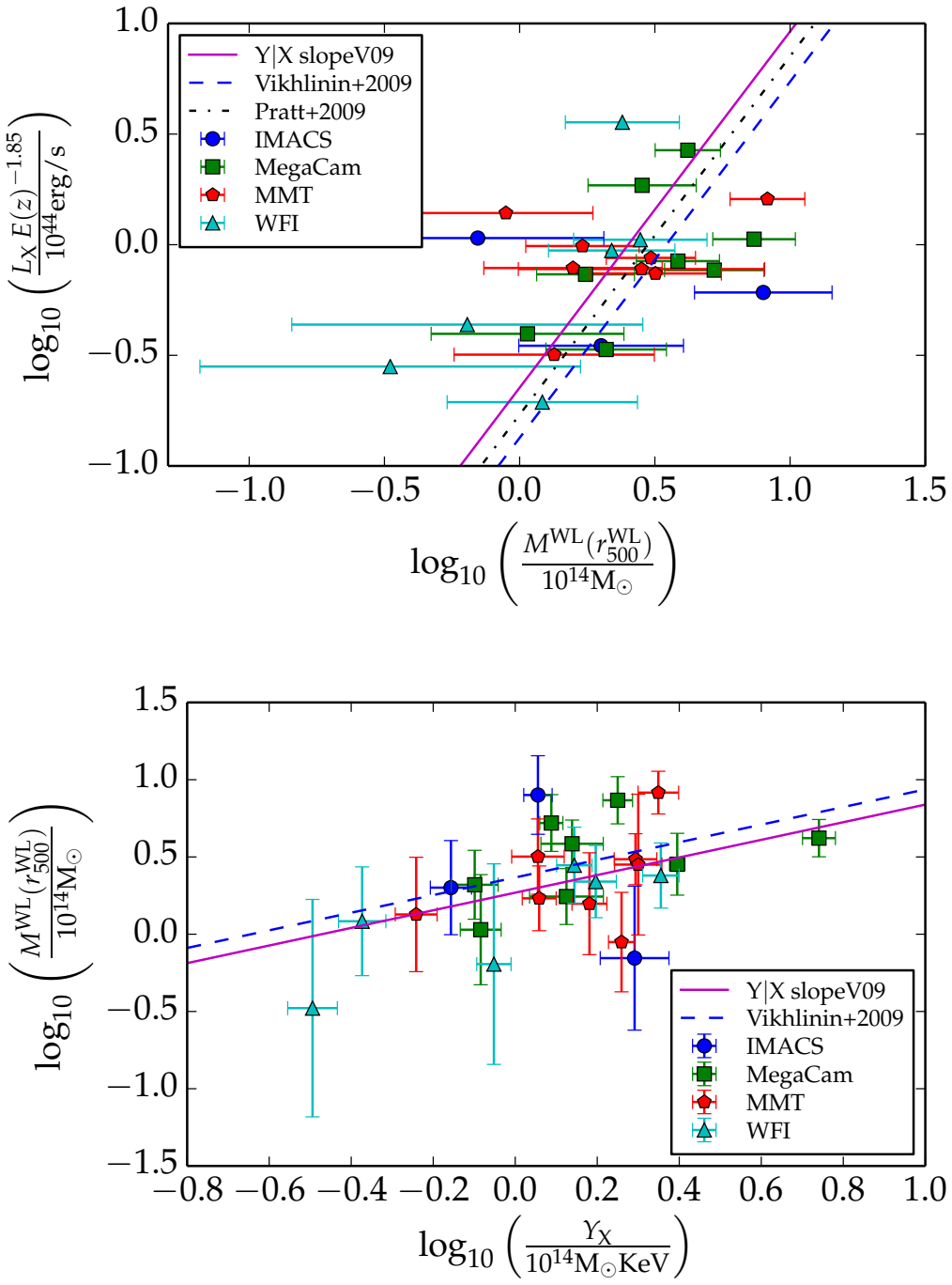


Figure 7.2: X-ray–Weak Lensing scaling laws obtained with the BCES Y|X minimization method with slope fixed to the Vikhlinin et al. (2009a) slope (solid magenta line) are compared with the V09 relation (blue dashed line). All the quantities other than the weak lensing masses are taken from V09. The relations dependent on the evolution are given for $z = 0.47$, the median redshift of our sample. The different shapes and colors of the data points indicate the various instruments. *Top:* scaling of the $L_X$–$M_{500}^{WL}$ relation. The blue dashed line and the black dot-dashed line indicate respectively the V09 and P09 relations, corrected for selection effects. Both works use 0.5-2.0 KeV X-ray luminosities. Our BCES fit (with slope fixed to the value of V09) lies at higher masses w.r.t. the V09 and P09 relations, after correcting for Malmquist bias by applying the method described in V09. *Bottom:* weak lensing mass against $Y_X$ parameter.

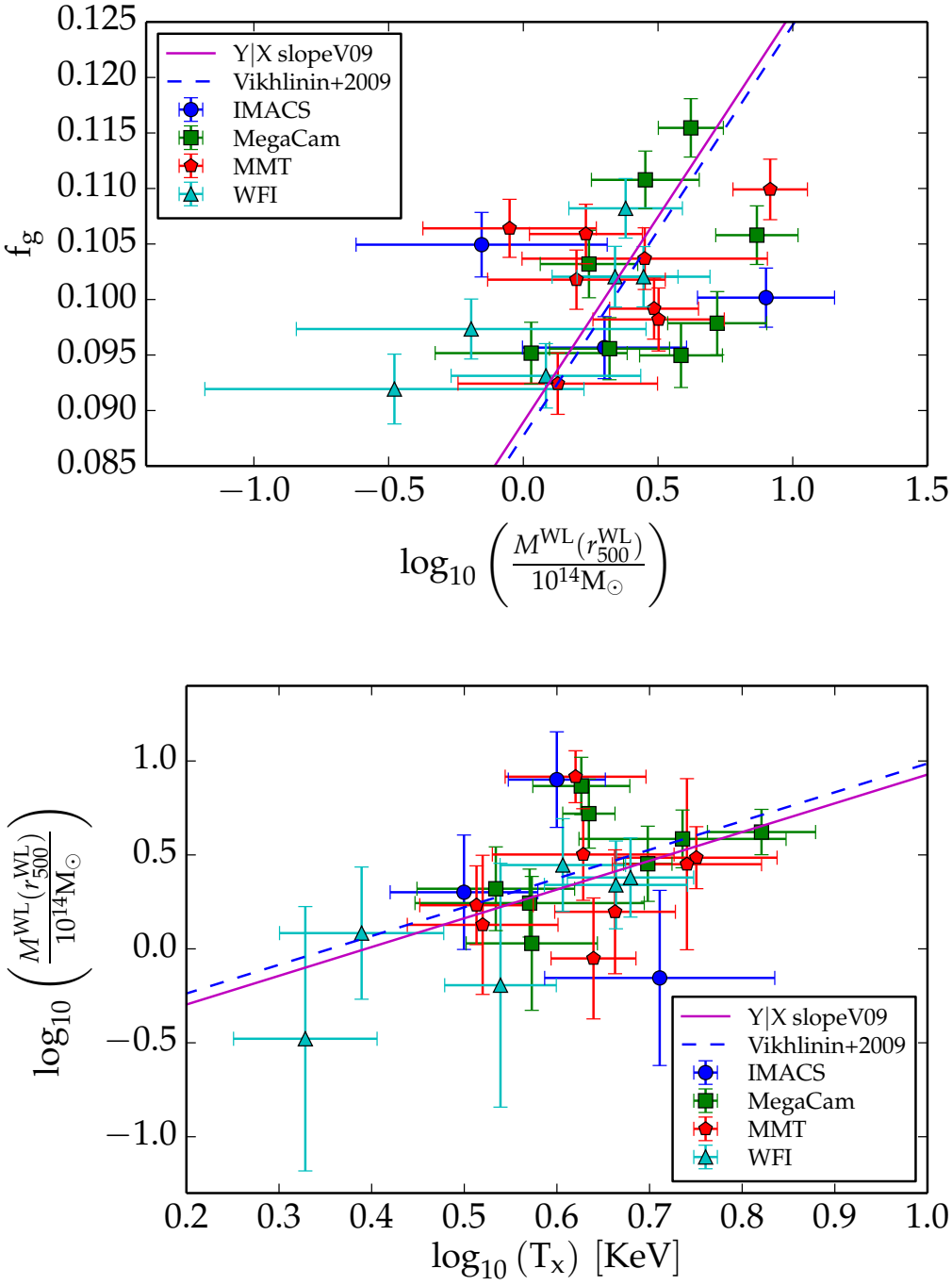


Figure 7.3: Continuation of Figure 7.2. *Top:* scaling of lensing mass with the hot gas mass fraction ($f_g$). *Bottom:* the weak lensing mass plotted against the X-ray temperature.

et al. 2009b).

Here we discuss how the weak lensing masses obtained for 25 *400dCS* clusters, analyzed in the previous sections, scale with the masses derived by V09 by means of X-ray mass proxies. Specifically, they are $M^{\rm G}$, $M^{\rm Y}$ and $M^{\rm T}$, namely for the proxies: hot gas mass, total thermal energy, and core-excised average temperature.

Figure 7.1 shows the total mass, $M^{\rm G}$, as estimated from the *Chandra* gas mass plotted against the weak lensing mass $M^{\rm WL}$. As the cosmological results from the X-ray study of the *400dCS* (Vikhlinin et al. 2009b) have been obtained considering the mass derived from the cluster gas mass, we choose $M^{\rm G}$ as our default X-ray mass. For a fair comparison we re-estimate the $M^{\rm WL}$ at the radius of the gas mass, $r^{G}_{500}$. Moreover, in a flux limited sample, the average X-ray luminosity of the observed sample is biased-high compared to the average of the parent population: this is known as the Malmquist bias. As this effect offsets the normalization of the $L_{\rm X}$–$M$ relation, for a more direct comparison with V09 and Pratt et al. (2009, P09) results (top panel of Figure 7.2), which are already corrected for Malmquist bias, we use $L_{\rm X}$ values appropriately corrected using the method suggested in V09.

The evolution term in the scaling laws we explore, follows the self-similar prediction for each case (Kaiser 1986). When we compare the relations between different components with other works, we calculate the evolution factor for the median redshift of our subsample ($z_{\rm med} = 0.47$), which corresponds to $E(z) = 1.286$.

### 7.1.1 Mass-dependent Bias

Simulations show that the hydrostatic equilibrium assumption in the X-ray mass estimates introduces a mass bias which underestimates the X-ray mass by a 10-30% level (w.r.t. the true mass), depending on the gas heating and cooling assumptions (e.g., Battaglia et al. 2012; Rasia et al. 2012).

Measuring this hydrostatic mass bias for our sample, we want to assure that the mean ratio between the X-ray and WL masses is unchanged taking its reciprocal. For this, we adopt its base 10 logarithm as an unbiased estimator for the mass ratio. Since we assume that WL masses should be unbiased on average, we estimate the bias

$$1 - b = 10^{f_{\log}} \quad , \tag{7.1}$$

calculating the logarithmic bias as:

$$f_{\log} = \langle \log_{10} M^{\rm G} - \log_{10} M^{\rm WL} \rangle \quad . \tag{7.2}$$

In Figure 7.4 we plot the logarithmic ratio of the total mass from the gas mass proxy measurements of V09 ($M^{\rm G}$) over our WL estimates ($M^{\rm WL}$) measured at the same X-ray radius $\rm r^{G}_{500}$ against our WL masses. The horizontal dashed line indicates the zero logarithmic bias. The yellow shaded area and the corresponding dot-dashed line show the overall $f_{\log}$, consistent with zero within its standard error of the mean. Splitting the whole sample at its median weak lensing mass ($2.27 \times 10^{14}\,\rm M_{\odot}$, pointed by the vertical dashed line), we obtain the logarithmic bias and its standard error on the mean for the low- and high-mass end, highlighted by the green shaded areas. The dot-dashed lines within the green boxes indicate $f_{\log}$ for those subsamples.

While the logarithmic bias is consistent with zero within its standard error of the mean ($f_{\log} = 0.029 \pm 0.043$), the sample hints to a mass-dependent bias when split around the median mass. X-ray masses are biased-high compared to WL masses in the low-mass subsample ($\langle M^{\rm G} \rangle = (1.477 \pm 0.174) \langle M^{\rm WL} \rangle$), while the high-mass end shows the opposite trend where X-ray masses are underestimated w.r.t. lensing masses ($\langle M^{\rm G} \rangle = (0.794 \pm 0.078) \langle M^{\rm WL} \rangle$). The trend in Figure 7.4 resembles the overall results of I15 (their Figure 2).

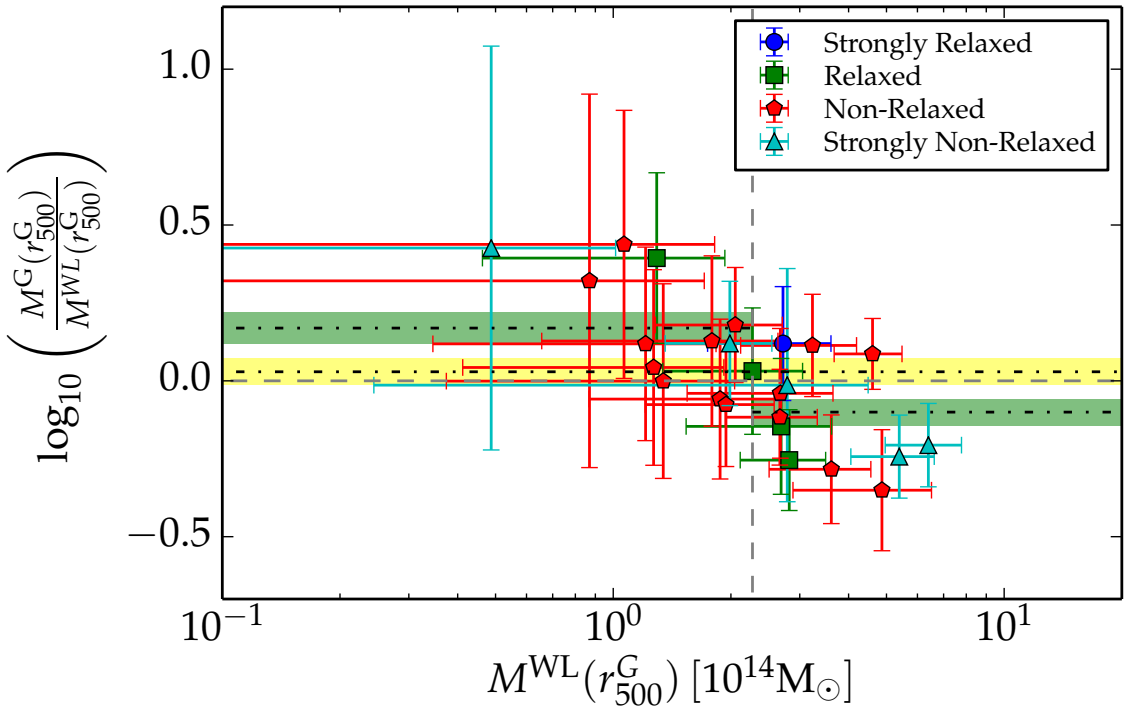


Figure 7.4: Logarithmic ratio between the total X-ray mass ($M^{G}$) and the weak lensing mass vs. the WL mass. All masses are estimated at the radius of the first ($r^{G}_{500}$). The gray horizontal dashed line indicates the zero logarithmic bias. The three dot-dashed lines and their corresponding colored boxes indicate the overall logarithmic bias (long dot-dashed lines with yellow shades) and the logarithmic bias for the two parts of the split sample (green shades and short dot-dashed lines) . The different symbols indicate the dynamical states suggested by (Parekh et al. 2015). See text and Table 7.1 for further details.

Adopting the morphological classification studied in Parekh et al. (2015) for the *400dCS*, we divide the clusters in four states (different colors and symbols in Figure 7.4): strongly relaxed, relaxed, non-relaxed and strongly non-relaxed. The distribution of the different dynamical states does not appear clustered towards a preferential mass regime. Thus, we find no indication for correlation with dynamical state. At low redshift, similar findings have been obtained before (e.g., Mahdavi et al. 2013). We notice that our sample is composed of 80% by dynamically disturbed clusters (15 non-relaxed and 5 strongly non-relaxed), being statistically consistent with the fraction (83%) of the whole sample of 36 clusters analyzed by Parekh et al. (2015). This corroborates the assumption that we study here an unbiased, random subsample.

For completeness, we perform the same analysis on the two other V09 mass proxies, $M^{T}$ and $M^{Y}$, finding the same trend as with $M^{G}$ (all values are summarized in Table 7.1).

### 7.1.2 The Luminosity-Mass Relation

The *eROSITA* satellite (Predehl et al. 2010; Merloni et al. 2012) will conduct an X-ray census of the sky with unprecedented depth, yielding new cluster catalogs which will span up to $z \sim 1.5$ (Pillepich et al. 2012; Borm et al. 2014). The luminosity-mass scaling law $L_{X}$–$M$ obtained for the high-$z$ sample

Table 7.1: List of mass-dependent mass bias (1-$b$) for all the investigated mass proxies. The values of $M^{\rm G}$, $M^{\rm Y}$ and $M^{\rm T}$ are taken from Table 1 of V09. The indicated uncertainties are the standard error of the mean.

| Proxy | Global | | $M^{\rm WL} < M^{\rm WL}_{\rm median}$ | | $M^{\rm WL} \geq M^{\rm WL}_{\rm median}$ | |
|---|---|---|---|---|---|---|
| $\langle \log_{10} \rangle$ | $\log_{10}(f)$ | $f$ | $\log_{10}(f)$ | $f$ | $\log_{10}(f)$ | $f$ |
| $M^{\rm G}/M^{\rm WL}$ | 0.029±0.043 | 1.069±0.105 | 0.169±0.051 | 1.477±0.174 | −0.100±0.043 | 0.794±0.078 |
| $M^{\rm Y}/M^{\rm WL}$ | 0.072±0.040 | 1.182±0.109 | 0.201±0.049 | 1.588±0.178 | −0.046±0.041 | 0.899±0.084 |
| $M^{\rm T}/M^{\rm WL}$ | 0.057±0.039 | 1.141±0.102 | 0.173±0.047 | 1.491±0.160 | −0.050±0.043 | 0.892±0.088 |

analyzed in this work represents a crucial support for *eROSITA*-like missions, as it reaches unprecedented low masses and high redshifts (Figure 5.1).

For cosmological purposes (e.g., fitting the cluster mass function to the data), the survey volume as a function of mass is needed. From the X-ray survey strategy we can easily calculate the volume as a function of luminosity. V09 show an X-ray $L_{\rm X}$–$M$ scaling relation, where they correct for the Malmquist bias assuming that the evolution of the $L_{\rm X}$–$M$ is negligible, which is true for the *400d* low-$z$ sample. For the high-$z$ sample, instead, the $E(z)$ term cannot be neglected, so they estimate the Malmquist bias for individual clusters (modeling the effects of selection trough the likelihood function).

In the top panel of Figure 7.2 we show $M^{\rm WL}_{500}$ as a function of the X-ray luminosity estimated in the 0.5-2.0 keV energy range ($L_{\rm X}$ values from Vikhlinin et al. 2009a). In our $L_{\rm X}$–$M$ we used the X-ray luminosities corrected for the Malmquist bias using the same method shown in V09. We consider the errors in $L_{\rm X}$ to be negligible and we fit using the BCES (Akritas & Bershady 1996) method and the Bayesian approach of Kelly (2007), which performs a linear regression accounting for intrinsic scatter. As in our case the mass is the fundamental property and the X-ray luminosity is the dependent variable, we prefer to show the minimization in the *y-axis* ($L_{\rm X}$) direction as the best choice for the BCES fitting, called the $Y|X$ fit.

The $L_{\rm X}$–$M$ scaling relation from V09 comes from the combined low-$z$ and high-$z$ sample, assuming the same slope at all redshifts. The slopes of Vikhlinin et al. (2009a) and Pratt et al. (2009, P09) are not significantly different (1.61 and 1.62 respectively), so we safely assume a common slope of 1.61 in the comparison. Therefore, we fix the slope to 1.61 and focus on the high-$z$ normalization. As shown in Figure 7.2 (upper panel), our fit gives a ∼38% lower mass than V09 (for a fixed luminosity). Their published relation comes from the mass proxy deriving from $Y_{\rm X}$, and we find that the overall bias between $M^{\rm Y}$ and the lensing masses is ∼18% (see Table 7.1). As a consequence, the disagreement between the magenta and blue lines in the top panel of Figure 7.2 cannot be entirely explained by the bias between the two mass estimate methods as there would be a ∼20% residual bias. Nevertheless, while V09 *assumed* the normalization evolution for their high-$z$ mass proxies, in this work we provide a factual verification.

In addition, the P09 fit (black dot-dashed line in the top panel Figure 7.2) normalization deviates by ∼19% from our fit. However the P09 is a different sample which covers a different mass and redshift range.

### 7.1.3 $Y_{\rm X}$, Temperature and Gas Fraction

For a complete comparison with V09, we correlate other relevant X-ray observables with our weak lensing masses. Those scalings are shown in the lower panel of Figure 7.2 and in Figure 7.3, for respectively: $Y_{\rm X}$, $T_{\rm X}$ and $f_{\rm g}$.

Kravtsov et al. (2006) proposed the X-ray equivalent of the Sunyaev-Zel'dovich (SZ) signal ($Y_{\rm X}$) as the most robust X-ray mass proxy, since it shows a very weak dependence on redshift and a small scatter with the total mass. For this reason, we compare our lensing masses with $Y_{\rm X}$ from V09, which is given

Table 7.2: Summary of the scaling relations we investigated in our work. All relations are in the linear form $y = \alpha x + \delta$ and are plotted in Figures 7.2 and 7.3. The normalization errors come from $10^5$ bootstrap realizations. As it is not possible to constrain at the same time the slope and the normalization, we fix the slope to the value used in V09.

| Relation ($x$–$y$) | Normalization $\delta$ | Slope $\alpha$ [from V09] | V09 Normalization |
|---|---|---|---|
| $\log_{10}(M/10^{14})$–$\log_{10}(L_X/10^{44})$ | −0.646±0.099 | 1.61±0.14 | −0.873±0.037 |
| $\log_{10}(Y_X/10^{14})$–$\log_{10}(M/10^{14})$ | 0.269±0.058 | 0.57±0.03 | 0.367±0.015 |
| $\log_{10}(M/10^{14})$–$f_g$ | 0.089±0.002 | 0.037±0.006 | 0.088±0.004 |
| $\log_{10}(T_X$–$M/10^{14})$ | −0.602±0.059 | 1.53±0.08 | −0.546±0.016 |

by the product of the X-ray temperature and the gas mass obtained from the X-ray spectrum and image, respectively.

Consequently, we also investigate the one-to-one relations of the WL masses with the gas mass fraction ($f_g$) and the X-ray temperature, taken from the X-ray analysis of V09.

The results for all relations are listed in Table 7.2 and are obtained fixing our slope to the V09 values. Comparing the normalizations with V09, we also find strong agreement within the 68.3% confidence level uncertainty range for the $M$–$f_g$ and $M$–$T_X$ relations. However, as expected from the 18% bias between $M^Y$ and WL mass, our $Y_X$–$M^{WL}$ relation (obtained from the V09 $M_{500}$–$Y_X$ scaling law) shows a lower normalization w.r.t. the V09 fit, giving ∼25% lower masses for fixed $Y_X$.

### 7.1.4 Comparison to other WL Samples

We find an overall mass bias consistent with zero, confirming the results of the first study on the *400dCS* sample pursued with 8 clusters by Israel et al. (2014). Also, our analysis upholds their indication for a mass-dependent bias with more significant evidence.

In Table 5.1 we have summarized the latest works which compare WL mass estimates with those obtained from X-ray or SZ. Differently from other samples, the survey strategy of the *400d* project focuses on covering a small sky area with a greater depth. This allows us to select lower mass clusters at higher redshift w.r.t. other works, as shown in Figure 5.1. This region in $M$–$z$ parameter space is much more typical and, therefore, much more important for upcoming cluster surveys like the one expected for *eROSITA* (Figure 15 in Borm et al. 2014).

It is worth to notice that in Figure 5.1, only the *LoCuSS* contour is based on the actual WL data of the 50 clusters (from Okabe & Smith 2016) that are consequently used in the hydrostatic bias investigation (Smith et al. 2016). For the *Weighing the Giants* project (*WtG,* von der Linden et al. 2014a; Kelly et al. 2014; Applegate et al. 2014) we plot the whole *WtG* sample, being aware that the two subsequent mass comparison studies, von der Linden et al. (2014b) and Applegate et al. (2016), use only a subsample of 22 and 12 clusters respectively. For the same reason, we consider the whole *Canadian Cluster Comparison Project* (*CCCP*, Hoekstra et al. 2015) sample. Finally, while the X-ray/WL comparison work of the *Cluster Lensing And Supernova survey with Hubble* (*CLASH*, Postman et al. 2012) studies 25 clusters, Donahue et al. (2014) present hydrostatic mass bias estimates for various subsamples which include from 3 up to 20 clusters. In Figure 5.1 we plot all 25 objects of their parent sample. For consistency in the comparison, in Figure 5.1 we consider the *400dCS* clusters not yet included in our follow-up project (empty circles) adopting their X-ray masses Vikhlinin et al. (2009a), as well as our WL estimated masses (filled circles). In our case, the difference of the median mass and the median redshift of the followed-up subsample of 25 *400dCS* clusters w.r.t. to the whole sample is < 1%, again supporting the assumption that the WL sample is a representative subsample.

Smith et al. (2016) find a redshift-dependent bias in the comparison between X-ray (Martino et al.

2014) and weak lensing (Okabe & Smith 2016) mass measurements of the 50 clusters of the *Local Cluster Substructure Survey* (*LoCuSS*). In their latest work they claim a redshift-dependent bias in their ratio between Planck masses (Planck Collaboration et al. 2015a) and Okabe & Smith (2016) weak lensing masses. Applying our definition of logarithmic bias (Eq. 7.2) on their WL and X-ray data, we find a hint for mass-dependent bias in their sample, as well (see Figure B.4 in Appendix). The *LoCuSS* mass bias we measure is $f = 1.01 \pm 0.06$ which, after splitting the sample around its median WL mass ($M_{500}^{\mathrm{WL}} = 6.5 \times 10^{14}\,\mathrm{M}_{\odot}$), becomes $f_{\text{low-}M} = 1.09 \pm 0.08$ and $f_{\text{high-}M} = 0.94 \pm 0.08$ for the subsamples below and above the median, respectively, so qualitatively consistent with the trend we find (although note the different covered mass ranges).

Simet et al. (2015) provide an estimate for the hydrostatic mass bias with a stacked analysis of 166 clusters of the *REFLEX+BCS+CIZA* X-ray catalog (e.g., Hajian et al. 2013). In particular they also split their sample in two mass bins: $0.6 - 4 \times 10^{14}\,h_{70}^{-1}\mathrm{M}_{\odot}$ and $4 - 15 \times 10^{14}\,h_{70}^{-1}\mathrm{M}_{\odot}$. Considering the 50 clusters of their high mass range, they show good agreement with our finding ($f = 0.84 \pm 0.09$). However, in contrast to our results, their low mass bin does not show an opposite trend ($f = 0.87 \pm 0.16$), but this could be due to the fact that our low mass bin probes roughly half of their low mass interval.

In the framework of the *WtG* project, von der Linden et al. (2014b) and Applegate et al. (2016) obtain a $M_{500}^{\mathrm{Planck}}$ to $M_{500}^{\mathrm{WL}}$ and a $M_{2500}^{\mathrm{X}}$ to $M_{2500}^{\mathrm{WL}}$ ratio, respectively, yielding opposite results. The study of von der Linden et al. (2014b) includes 22 clusters which are in common between the *WtG* sample and the *Planck* cluster cosmology analysis, finding an X-ray-to-lensing mass ratio $f = 0.688 \pm 0.072$, giving a hydrostatic bias of 31%. They also find a hint for a mass-dependent mass bias with a turnover point at $M > 6 \times 10^{14}\,\mathrm{M}_{\odot}$ which follows our trend. They justify their finding by pointing at the *Chandra/XMM* ~30% temperature discrepancy (Schellenberger et al. 2015), as *Planck* masses were calibrated with *XMM-Newton* observations (Arnaud et al. 2010). On the other hand, Applegate et al. (2016) compare 12 relaxed *WtG* clusters (selected with morphological indicators) with *Chandra* X-ray masses. Using updated masses ($M_{2500}$) w.r.t. their original sample (of Applegate et al. 2014), they obtain a mass ratio completely consistent with unity ($f = 0.967^{+0.063}_{-0.092}$) and they do not find any mass related bias.

The *CCCP* aperture masses find excellent agreement with the *WtG* results. Their analysis results in similar findings to von der Linden et al. (2014b) work, with a mass ratio $f = 0.76 \pm 0.11$.

It is important to note that the *CCCP* and *WtG* study of von der Linden et al. (2014b) compare their WL masses with Planck masses which are calibrated with X-ray masses, in particular from *XMM-Newton*. Thus, the relation to the X-ray hydrostatic mass bias is not straightforward (as shown in more detail by Israel et al. 2015). However, as their samples include very few low-mass objects, their results are in excellent agreement with our massive end ($M^{\mathrm{WL}} > 2.27 \times 10^{14} M_{\odot}$) subsample mass bias ($f = 0.794 \pm 0.078$).

A comparison of WL mass profiles to *Chandra* and *XMM-Newton* mass estimates is performed by Donahue et al. (2014) (*CLASH-X* project) for 25 of the *CLASH* clusters. They examine WL profiles from a joint analysis of magnification and shear (Umetsu et al. 2014) together with X-ray data, and also compare with combined strong and weak lensing results (Merten et al. 2015). In Donahue et al. (2014) are provided mass ratio quantities for a plethora of combinations of masses, apertures, analysis options and sample sizes. Considering the results extrapolated at $r_{500}$, they find a significant mass bias for *XMM* hydrostatic mass measurements (~44% with sample size of 16), more than what is resulting from the comparison with *Chandra* (~22% with sample size of 20).

CHAPTER 8

# Summary and Outlook

Galaxy clusters have become a cornerstone in cosmology, playing also an important role as an independent probe for cross-checking other cosmological experiments. The comparison of X-ray and weak lensing observations bring significant knowledge about the weak lensing unbiased mass and the X-ray observables, which will be precious for the forthcoming missions and for *eROSITA* in particular.

## 8.1 Summary of Results

In this thesis we have completed the weak lensing follow-up of eighteen high redshift galaxy clusters of the *400d Cosmological Survey*. We have estimated their weak lensing masses and compared them with a series of X-ray observables, such as X-ray luminosity, gas mass fraction, X-ray temperature and X-ray Compton parameter. For the first time, such a work has been done on a statistically complete, homogeneous and flux limited X-ray sample: very suitable for precise cosmology thanks to its well-known selection function.

The clusters studied in this work are a subsample of the *400d Cosmological Sample*: a high redshift ($0.35 \leq z < 0.90$) ensemble of galaxy clusters selected from serendipitous *ROSAT PSPC* X-ray observations (Vikhlinin et al. 2009a). The X-ray studies of Vikhlinin et al. (2009b) on these *400dCS* objects have yielded important results on cluster cosmology.

The weak lensing follow-up of the *400d cosmological sample* project, finds its origin in the work of Israel et al. (2012), which analyzed eight clusters with targeted observations at the *MMT* telescope. In this thesis we accurately measure galaxy shears for four *IMACS* clusters, eight *MegaCam* clusters and six *WFI* clusters. The heterogeneous data deriving from those ground-based observations is processed via a modified version of the `THELI` pipeline (Erben et al. 2005). In particular, the *IMACS* data reduction is particularly challenging, because of the not optimal raw data format and the unreported changes in the telescope set-up. To cope with this issue, we implemented in `THELI` a method to recover the astrometry, based on the position of stars in single CCDs. In addition, we introduce new tests for the quality of the shear measurement.

We use the photometric method of Klein (2013) to create catalogs of background galaxies, which is applicable on the large majority of our clusters as it requires only three bands. The lensing catalogs are matched to a reference catalog with photometric redshifts (COSMOS in our case), in order to attribute a redshift to the single galaxies.

By fitting the clusters shear profile with an NFW profile, we provide lensing masses for all of them,

also updating the ones for the 8 *MMT* clusters of Israel et al. (2012) in order to rely on a homogeneous analysis. We make use of S-statistics maps to identify other neighboring clusters and to assess the significance of the cluster detection. Thanks to this, we find that four of our objects need a double NFW fit. As an example, we notice that CL0328−2140 is situated next to a previously unknown cluster at its same redshift. Furthermore, one of our clusters, CL0542−4100, does not show a significant detection, therefore it is excluded from the following analysis.

Using a final subsample of 25 clusters, we study the scaling relations between the weak lensing mass and the X-ray observables, testing for the first time the low mass and high redshift regime, which is more typical for *eROSITA*-like surveys, but at the same time more challenging for lensing studies.

We compare our weak lensing masses $M^{\mathrm{WL}}$ with X-ray observables and X-ray masses from Vikhlinin et al. (2009a) estimated from the gas mass ($M^{\mathrm{G}}$), from the X-ray temperature ($M^{\mathrm{T}}$) and by means of the $Y_{\mathrm{X}}$ Compton parameter ($M^{\mathrm{Y}}$).

- We show a hint for a mass-dependent mass bias. Low-mass clusters (w.r.t. the median mass of our sample) have their X-ray masses biased-high compared to the weak lensing masses ($\langle M^{\mathrm{G}}\rangle = (1.45 \pm 0.07)\langle M^{\mathrm{WL}}\rangle$), while high mass cluster masses are biased low ($\langle M^{\mathrm{G}}\rangle = (0.79 \pm 0.03)\langle M^{\mathrm{WL}}\rangle$). The logarithmic bias in both mass-ranges does not overlap with the no-bias regime. Furthermore, the mass bias does not show any dependence on the dynamical state of the cluster gas, in agreement with other works. However, the hydrostatic bias measured by considering the whole mass range is consistent with zero.

- The overall mass bias is consistent with zero: $\langle M^{\mathrm{G}}\rangle = (1.069 \pm 0.105)\langle M^{\mathrm{WL}}\rangle$. This results does not show any indication for a cluster mass bias significant enough to alleviate the tension between *Planck* CMB results and *Planck* cluster cosmology.

- Our analysis of the correlations between our WL masses and the X-ray observables from V09 denotes a good agreement between our scaling relations with our weak lensing masses and the ones from V09 derived from their X-ray study. In the case of the $L_{\mathrm{X}}$–$M$ scaling relation, where our fit gives ∼33% lower masses, even considering that the $M^{\mathrm{Y}}$ masses (used in V09 for their relation) overestimates the weak lensing masses by ∼18%, the discrepancy remains. However, this difference would be reduced to ∼20%.

- The scalings of gas mass fraction and X-ray temperature, obtained by keeping the slope fixed to the V09 value, agree with their X-ray study within the 68.3% of confidence level. On the other hand, our $M^{\mathrm{WL}}$–$Y_{\mathrm{X}}$ relation is inconsistent with the respective fit in V09. However, this reflect the bias between our WL masses and the X-ray $M^{\mathrm{Y}}$. Finally, while V09 *assumes* the redshift evolution in their work, in this work we verify this empirically.

## 8.2 Future Perspectives

The excellent suitability of the *400dCS* for precision cosmology offers great perspectives of improvements for the current status of the analysis. A few more tests for addressing known problematics in cluster weak lensing mass estimates are needed.

A source of uncertainty in the mass estimation is the contamination by cluster members. Although the photometric method we adopt discards foreground members, still remaining cluster galaxies might dilute the lensing signal. We plan to account for the dilution of remaining foreground and cluster galaxies by

applying a boosting factor to the ellipticity. As the number of galaxies with $z \geq z_d$ increases at small radii from the cluster center, this factor can be modeled as a $1/r$ function (Hoekstra et al. 2012).

At large radii from the cluster core, the large-scale structure (LSS) introduces noise in the lensing signal, reducing the accuracy of weak lensing masses. Using simulated clusters, Hoekstra (2003) finds that $M_{200}$ uncertainties due to the LSS (uncorrelated with the cluster) increase with redshift, as the WL signal is sensitive to any matter along the line of sight. Their results are obtained for masses higher than ours and at a lower redshift ($z = 0.3$). The understanding of the LSS effect on the mass estimates would benefit by ad hoc weak lensing simulations for $M$ and $z$ closer to our sample values. Furthermore, an additional source of noise in the lensing estimation with the NFW fitting method are given by the triaxiality of the halos and the correlated LSS. Becker & Kravtsov (2011) find that the intrinsic scatter in the WL masses goes from the ∼20% for high mass to ∼30% for low mass clusters.

In our current analysis we use a shear calibration factor of $1.08 \pm 0.05$ as in I12, for all clusters. We plan to study the S/N dependence of the shear calibration bias by investigating the behavior of the shear measurements with the depth of observation, for each single instrument of our follow-up. This will better characterize the shear calibration on instrument- and S/N-based criteria.

Once having in hand robust weak lensing masses with a deep understanding of all uncertainties for the sample of 25 clusters, all selection effects have to be taken into account for updating the WL-X-ray scaling relations. Furthermore, as shown by Mantz et al. (2015, 2016), cosmological models and predictions from scaling relation observations, cross-influence each other. For this, it is needed to constrain that simultaneously for more accurate results. In our work, we make a crude correction for the Malmquist bias by making use of individually-corrected X-ray luminosities. However, other sources of uncertainty have to be addressed. Completing the follow-up of the whole *400dCS* sample will allow us to have a detailed account of selection effects. As recently pointed out by Sereno & Ettori (2015), the combination of selection effects and intrinsic scatters could yield a trend for the mass bias which is similar to what we find.

In Table D.1 we list the 11 clusters excluded from our subsample (including our non-detection case CL0542−4100).

We have demonstrated how important it is to cross-check cluster masses using different methods, especially with the weak lensing approach which is assumed to provide unbiased masses. The future looks exciting with new X-ray cluster surveys which will push the observable border to high redshift, providing tighter constraints on cosmological parameters, further unveiling the early Universe and shedding some light on its evolution.

APPENDIX A

# Updated MMT Masses

For the three-band cluster fields in I12, the `SExtractor` catalogs of the "double detection" mode at the KSB step were merged together in a single main catalog. Also the `FLAG` key of the detection band ($i'$) was transferred to the main catalog, in order to point out objects that do not have a reliable estimate of their flux. However, the `FLAG` keys for the three supporting bands ($g'$, $r'$ and the convolved $i'$) were not copied.

From this catalog were then discarded all objects with `FLAG` $> 0$, which means that flagged objects in the supporting bands were still included in the main catalog. This means that incorrect fluxes were allowed to enter in the KSB analysis. To these incorrect fluxes correspond apparently reasonable magnitudes, but their flux and magnitude errors had a zero value.

We solve this problem by substituting all the wrong magnitudes pointed by a non-zero `FLAG` value, with a dummy value. This yields a completely clean final catalog, due to the subsequent filtering in magnitudes.

We repeat exactly the same analysis of I12 for the four *MMT* three-band clusters, using correctly filtered catalogs. In Table A.1 we show both the I12 and the updated results of the NFW fitting. The masses do not change significantly. We remark that we do not use these new values for the *MMT* masses in our analysis, as in this work we use updated methods described in Section 6.1.

Table A.1: Updated masses and relative parameters ($r_{200}$, $c_{\mathrm{B12,NFW}}$) for the four *MMT* clusters of I12 observed in three bands. The values are obtained using the Bhattacharya et al. (2013) mass-concentration relation. Note that for consistency with I12, we use $h = 0.72$ while the NFW fitting has been fixed to the *ROSAT* X-ray peak.

| | Israel et al. (2012) | | | Updated | | |
|---|---|---|---|---|---|---|
| Cluster | $r_{200,\mathrm{B12}}$ [Mpc] | $c_{\mathrm{B12}}$ | $M_{200,\mathrm{B12}}$ [$10^{14}\mathrm{M}_\odot$] | $r_{200,\mathrm{B12}}$ [Mpc] | $c_{\mathrm{B12}}$ | $M_{200,\mathrm{B12}}$ [$10^{14}\mathrm{M}_\odot$] |
| CL0030+2618 | $1.45^{+0.13}_{-0.15}$ | 3.4 | $6.23^{+1.87}_{-1.76}$ | $1.43^{+0.14}_{-0.15}$ | 3.3 | $5.98^{+1.90}_{-1.69}$ |
| CL0159+0030 | $1.31^{+0.22}_{-0.27}$ | 3.6 | $4.10^{+2.46}_{-1.76}$ | $1.33^{+0.23}_{-0.28}$ | 3.6 | $4.27^{+2.56}_{-2.16}$ |
| CL0230+1836 | $1.51^{+0.27}_{-0.32}$ | 2.9 | $10.23^{+6.59}_{-5.18}$ | $1.49^{+0.28}_{-0.33}$ | 2.9 | $9.68^{+6.46}_{-5.15}$ |
| CL0809+2811 | $1.71^{+0.19}_{-0.22}$ | 3.4 | $9.24^{+3.46}_{-3.14}$ | $1.57^{+0.21}_{-0.25}$ | 3.5 | $7.11^{+3.36}_{-2.90}$ |

APPENDIX **B**

# Scaling Relations Details

## B.1 Mass Bias

Here are presented some further checks we have performed in our scaling relation analysis such as the investigation of the mass bias with $M_{\rm Y}$ and $M_{\rm T}$ and the dependency of the mass bias with redshift.

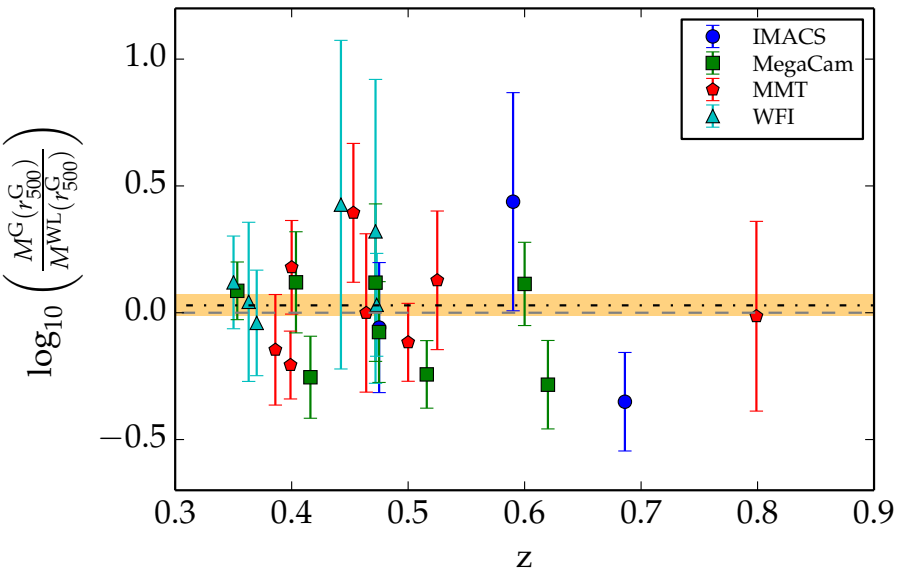


Figure B.1: Logarithmic ratio dependency with the redshift. The gray dashed line is the zero logarithmic bias, while the black dot-dashed line and the orange shadowing indicate the standard error of the mean. The logbias has a value of $\log 10(f) = 0.029$, while $f = 1.069 \pm 0.105$, showing no indication for any redshift dependent mass bias.

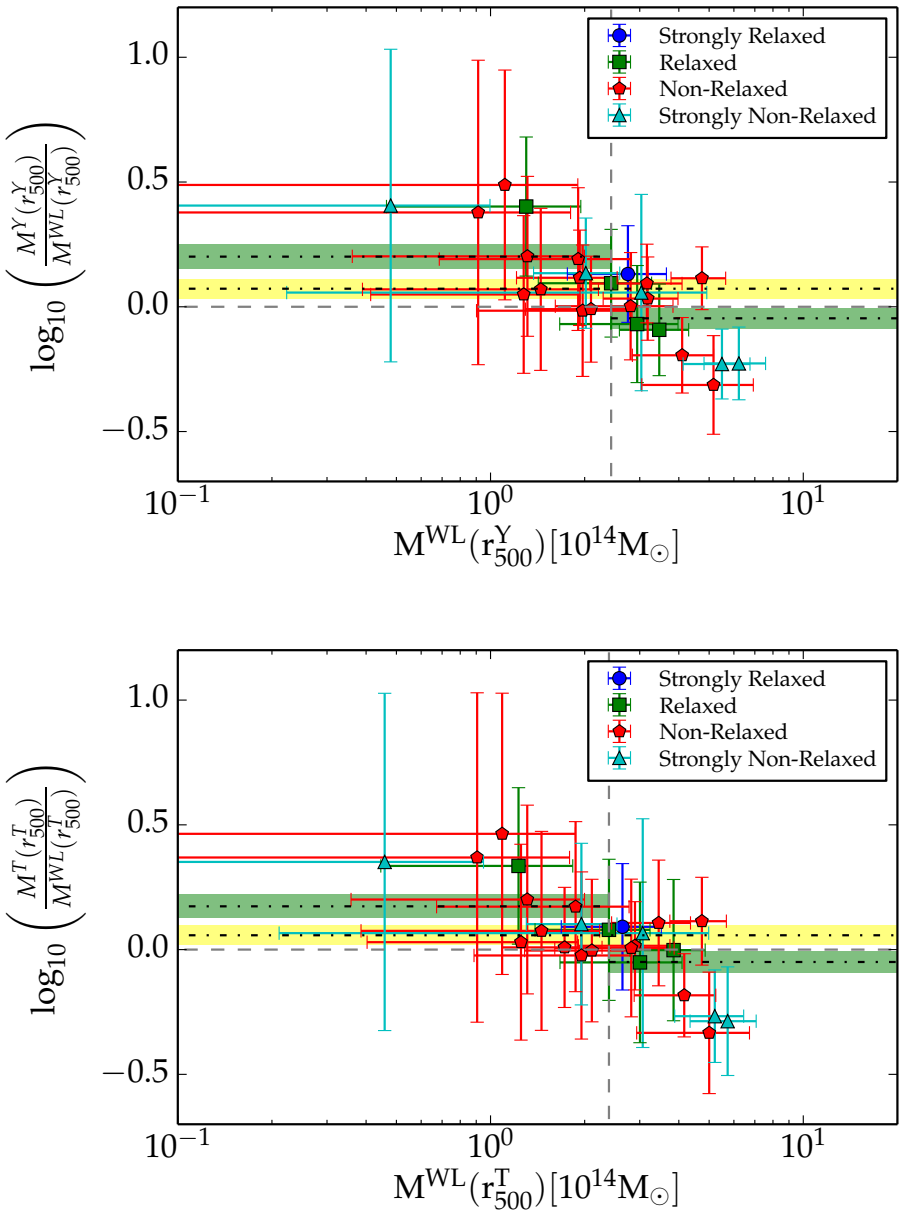


Figure B.2: Logarithmic ratio between the total mass estimated with an X-ray proxy and the weak lensing mass estimated at the radius of the first, as in Figure 7.4. In the *upper panel* it is shown for $M^{Y}$, while in the *lower panel* $M^{T}$. The gray horizontal dashed line indicates the zero logarithmic bias. The three dot-dashed lines and their corresponding colored boxes indicate the overall logarithmic bias (long dot-dashed lines with yellow shades) and the logarithmic bias for the two parts of the split sample (green shades and short dot-dashed lines) . The different symbols indicate the dynamical states suggested by (Parekh et al. 2015). See text and Table 7.1 for further details.

Table B.1: Similarly to table 7.1: mass-dependent mass bias (1-$b$) for the X-ray mass proxies. The values of $M^{\rm G}$, $M^{\rm Y}$ and $M^{\rm T}$ are taken from Table 1 of V09. The indicated uncertainties are the standard error of the mean.

| Proxy | Global | | $M^{\rm WL} < M^{\rm WL}_{\rm median}$ | | $M^{\rm WL} \geq M^{\rm WL}_{\rm median}$ | |
|---|---|---|---|---|---|---|
| $\langle \log_{10} \rangle$ | $\log_{10}(f)$ | $f$ | $\log_{10}(f)$ | $f$ | $\log_{10}(f)$ | $f$ |
| $M^{\rm G}/M^{\rm Y}$ | −0.065±0.015 | 0.861±0.030 | −0.104±0.022 | 0.787±0.040 | −0.029±0.015 | 0.935±0.033 |
| $M^{\rm G}/M^{\rm T}$ | −0.043±0.027 | 0.905±0.056 | −0.116±0.038 | 1.056±0.068 | 0.023±0.028 | 1.056±0.068 |

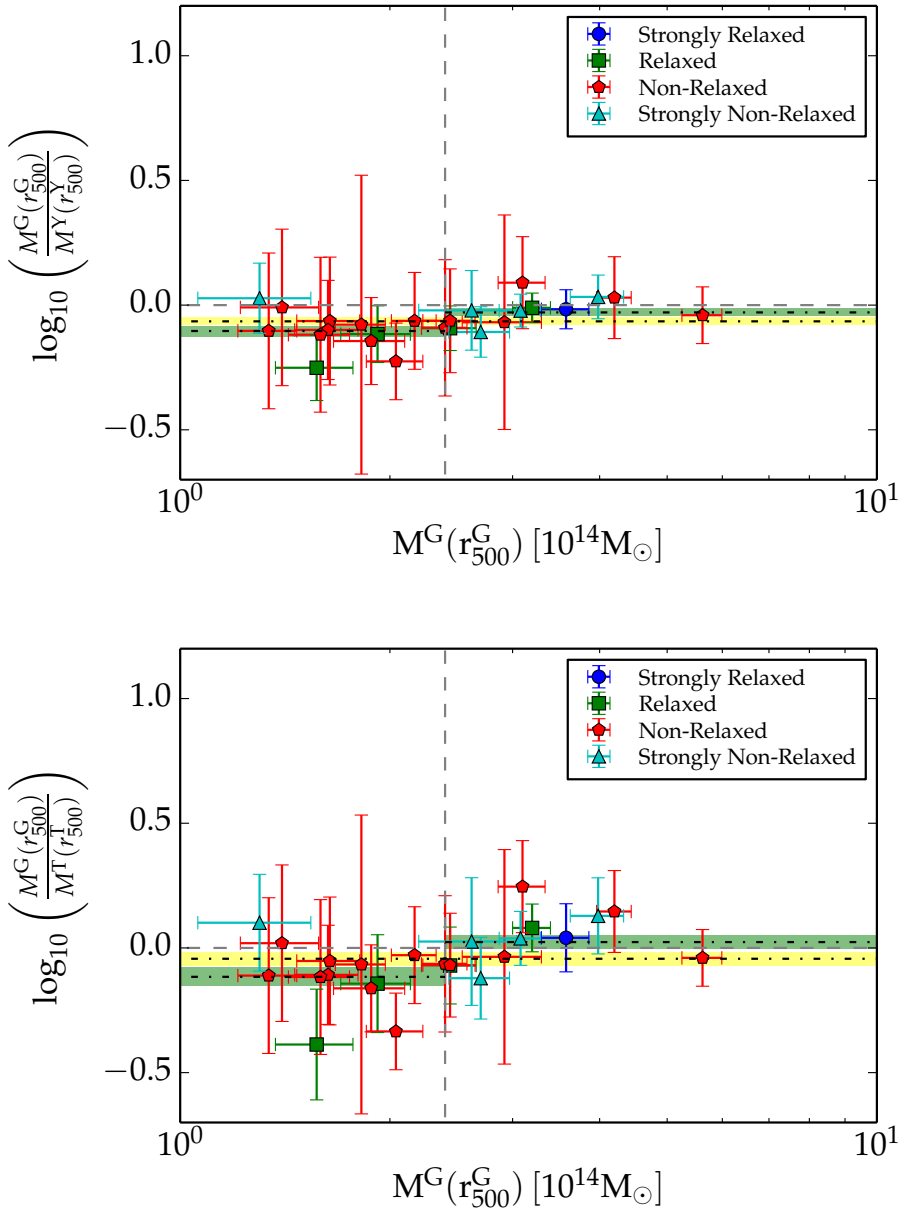


Figure B.3: Comparison of the X-ray $M_{\rm G}$ with the other two proxies ($M_{\rm Y}$ and $M_{\rm T}$) through logarithmic ratio. The mass is estimated at the radius of $M_{\rm G}$. Lines and colors as in Figure B.2. The results are summarized in Table B.1.

## B.2 LoCuSS

In Section 7.1.4, we have explored the findings of other studies on different samples. As Smith et al. (2016) discuss a redshift-dependent mass bias for *LoCuSS*, we check for a possible mass-dependent mass bias. We apply to different cuts in $M^{\mathrm{WL}}$: at the *LoCuSS* median WL mass ($6.5 \times 10^{14}\,\mathrm{M}_{\odot}$) and at the *400dCS* median WL mass ($2.27 \times 10^{14}\,\mathrm{M}_{\odot}$). The trend shown in Figure B.4 is consistent with the findings of our sample (see details in Section 7.1.4).

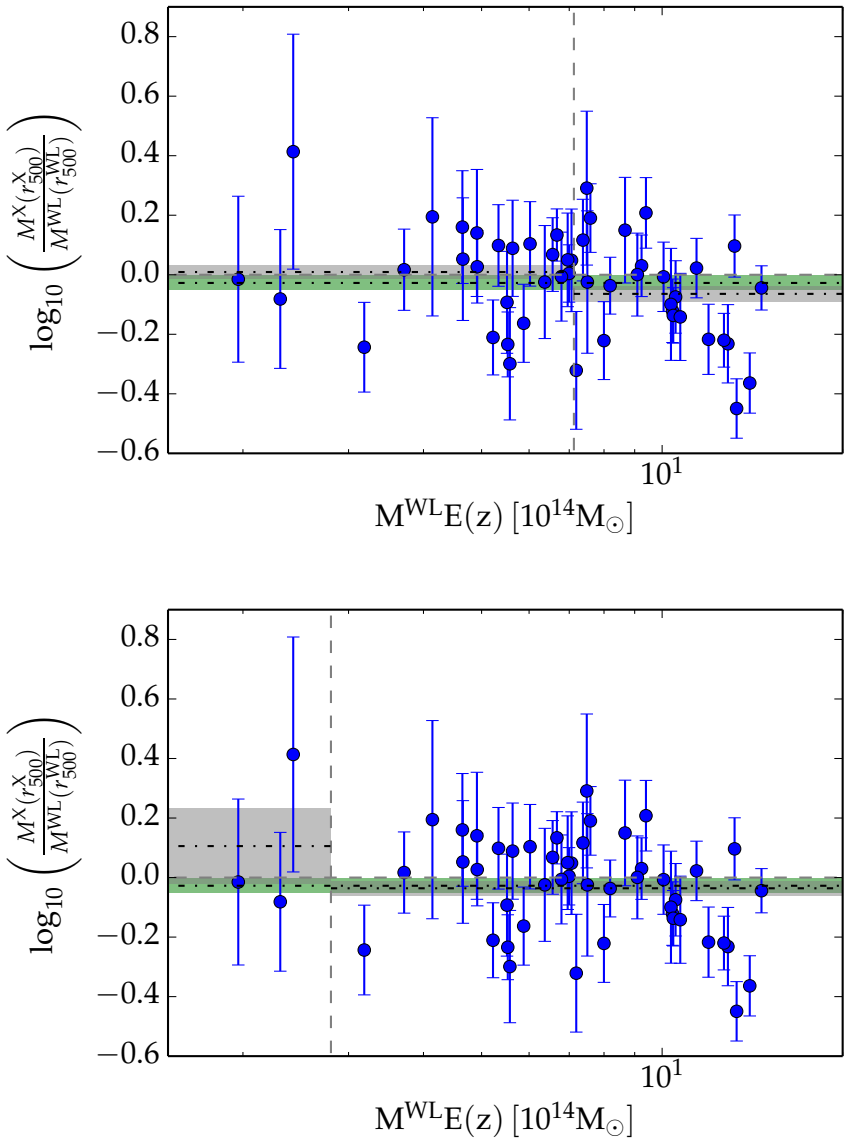


Figure B.4: Logarithmic mass ratio vs. WL mass for the *LoCuSS* sample. As we take the data from Martino et al. (2014) (X-ray) and Okabe & Smith (2016) (weak lensing), the radius at which the respective X-ray and WL masses are estimated is not the same.

# APPENDIX C

# Images of the Clusters

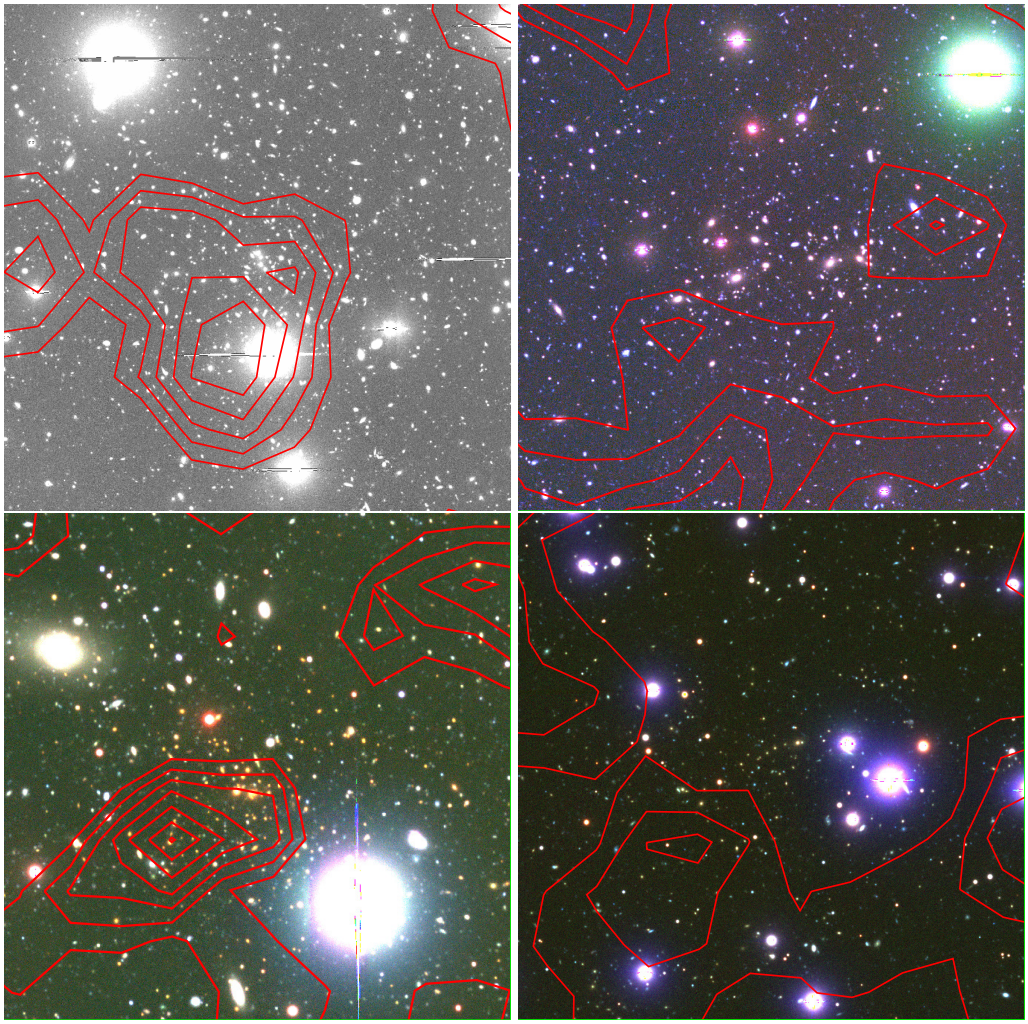

Figure C.1: Postage stamps of the inner 2 square arcminutes of the *IMACS* clusters. The red contours indicate the S-statistics for values in the range [1–10] with steps of 0.5. From the *top-right panel* in clockwise order: CL0328−2140, CL0333−2456, CL0405−4100, CL0542−4100.

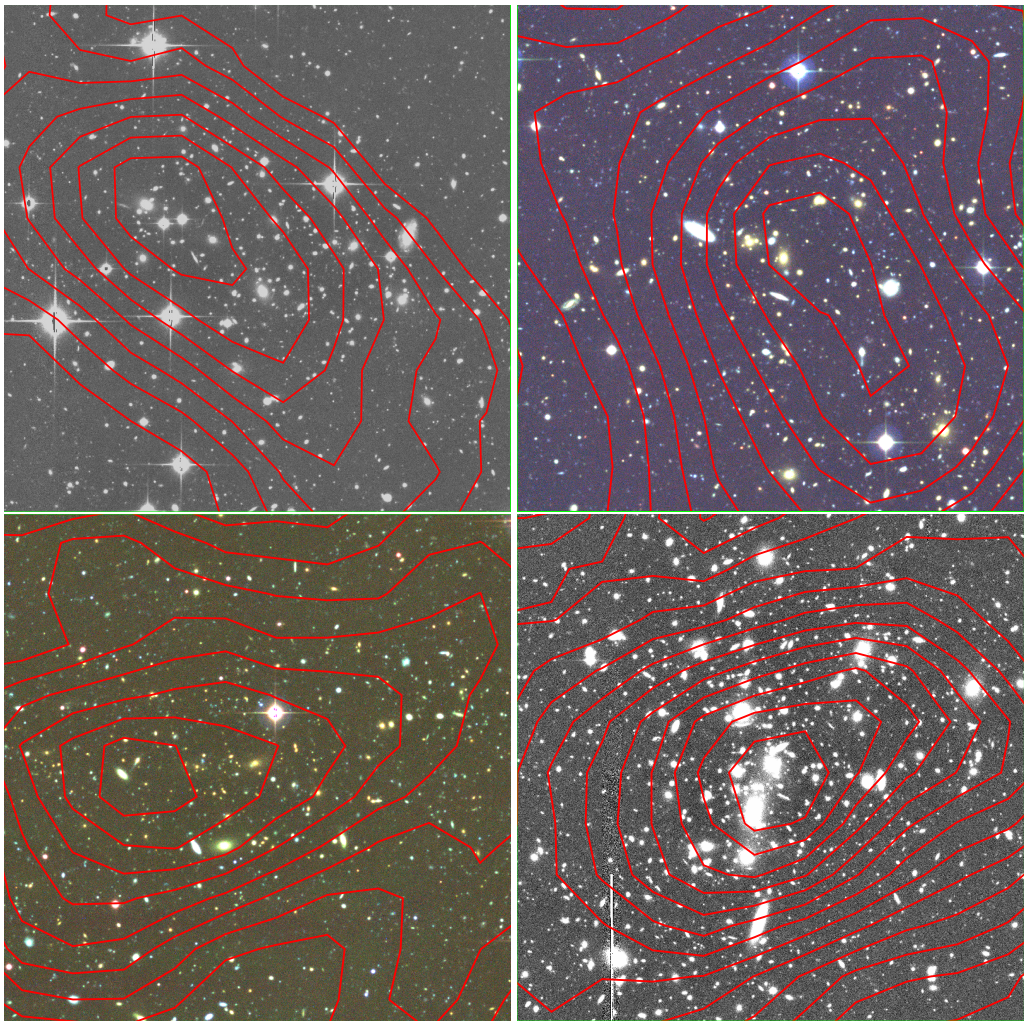

Figure C.2: Postage stamps of the inner 2 square arcminutes of the *MegaCam* clusters. The red contours indicate the S-statistics for values in the range [1–10] with steps of 0.5. From the *top-right panel* in clockwise order: CL0853+5759, CL1003+3253, CL1120+4318, CL1212+2733.

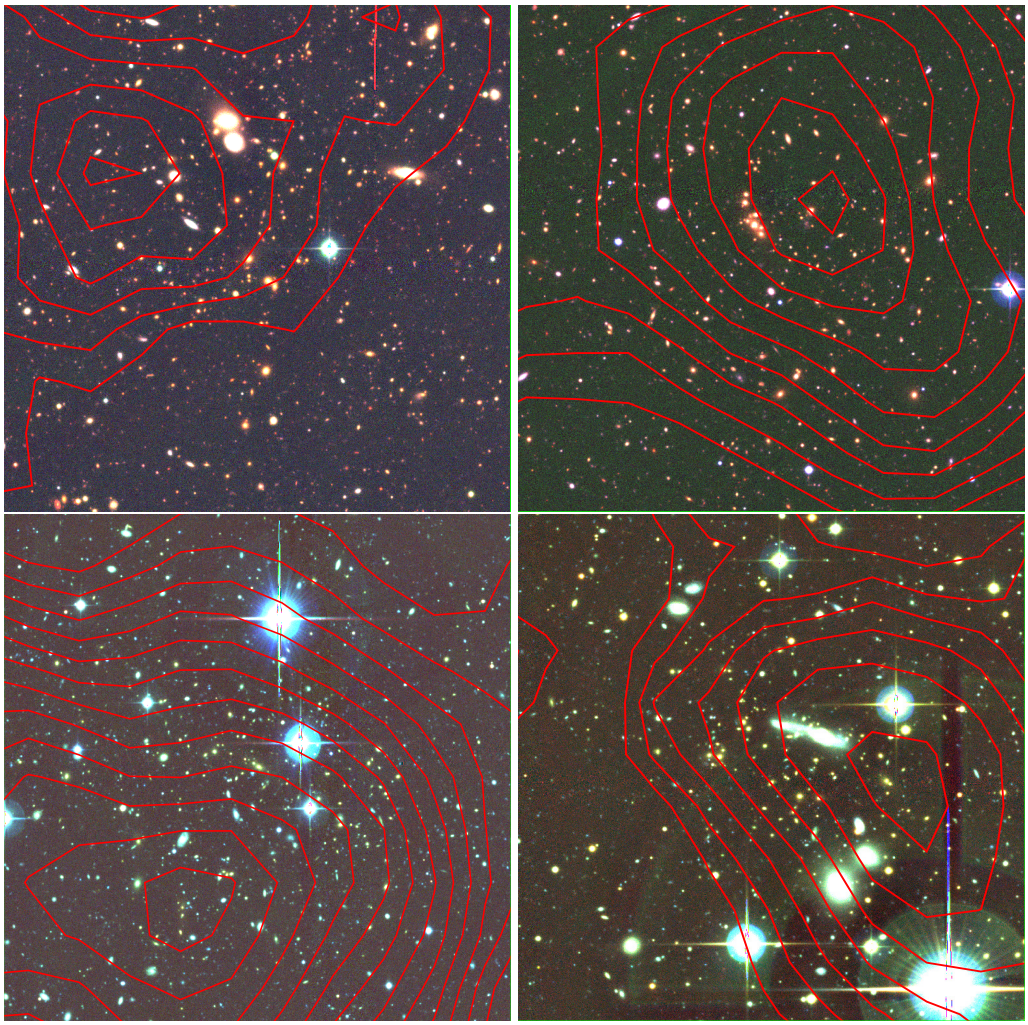

Figure C.3: Postage stamps of the inner 2 square arcminutes of the *MegaCam* clusters. The red contours indicate the S-statistics for values in the range [1–10] with steps of 0.5. From the *top-right panel* in clockwise order: CL1222+2709, CL1312+3900, CL1334+5031, CL1524+0957.

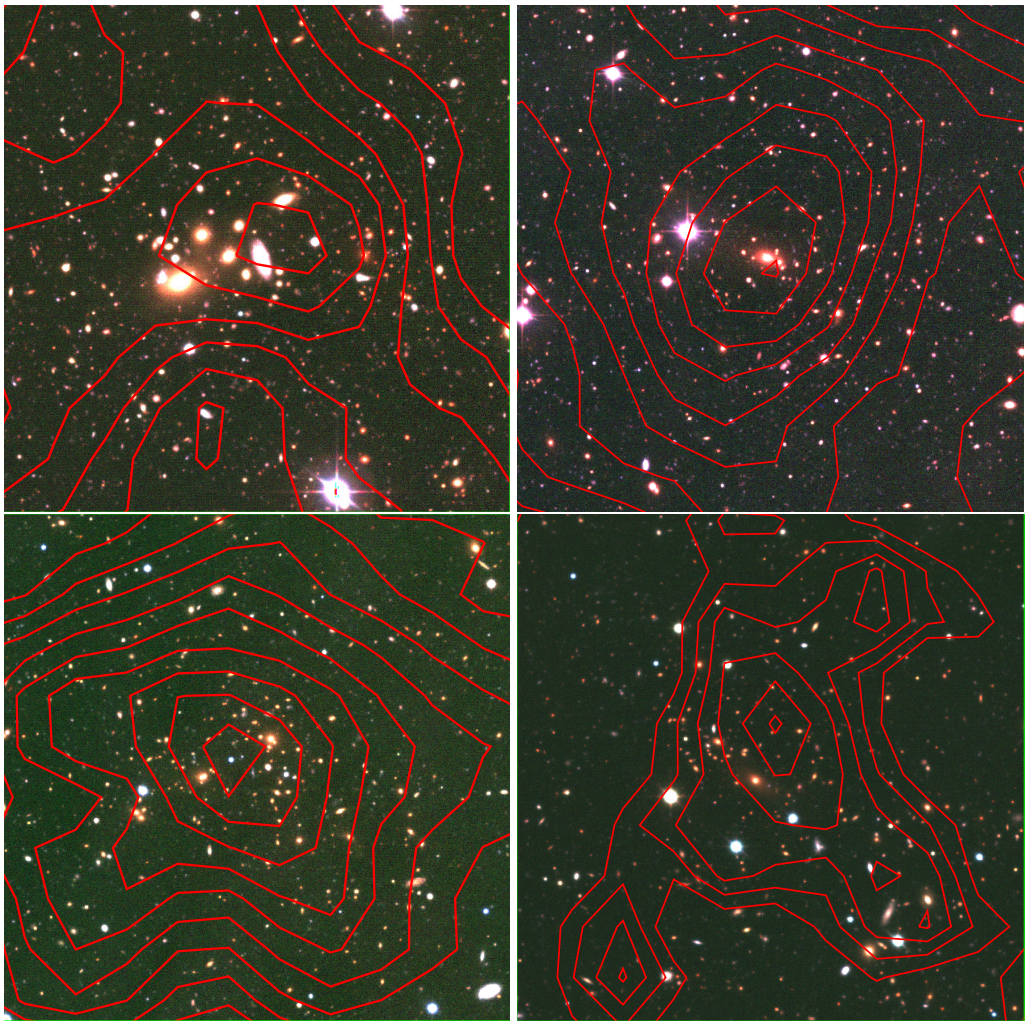

Figure C.4: Postage stamps of the inner 2 square arcminutes of the *WFI* clusters. The red contours indicate the S-statistics for values in the range [1–10] with steps of 0.5. From the *top-right panel* in clockwise order: CL0141−3034. CL0302−0423, CL0318−0302, CL0350−3801.

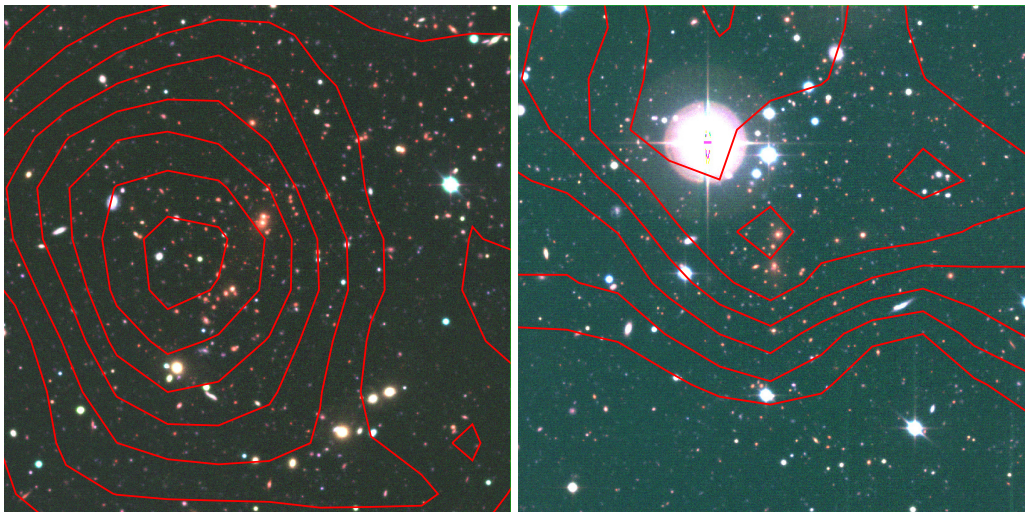

Figure C.5: Postage stamps of the inner 2 square arcminutes of the *WFI* clusters. The red contours indicate the S-statistics for values in the range [1–10] with steps of 0.5. *Left*: CL0355−3741, *right*: CL0522−3624.

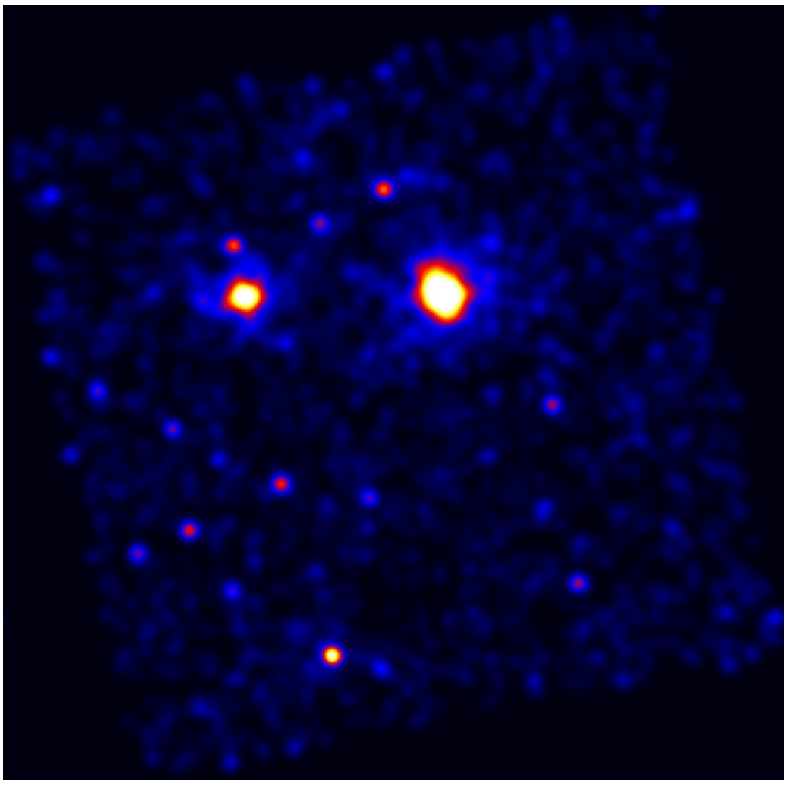

Figure C.6: *Chandra* X-ray image of CL0328−2140 (on the left) and its bright neighbor (on the right). Image obtained in the soft-band [0.5–2keV] and adaptively smoothed with a Gaussian kernel.

APPENDIX D

# Status of the *400dCS* Lensing Follow-up

In this thesis we have joined the eight *MMT clusters* of I12 to our 18 new clusters from the other three instruments. After discarding CL0542−4100, we investigate the scaling laws for a subsample of 25 objects of a total of 36 clusters of the *400dCS*.

Here we summarize the status of the weak lensing follow-up program in a table containing only the galaxy clusters which remain to be observed or analyzed. As we have collected all archival data and assessed the quality for those from *MegaCam*, in Table D.1 we do not list those *MegaCam* data which are found to be too shallow for weak lensing studies.

Table D.1: Summary of the status of the weak lensing follow-up of our sample. 25 objects have been studied. 4 objects have archival data. 6 objects need observations. In the case of data from more than one telescope, we list only the deepest observation (for lensing band, typically $r'/R$ or $i'/I$) or the data from the same telescope of the lensing band. Exposure times are in thousands of seconds (ks).

| Cluster | Redshift | $u'/B$ | $g'/V$ | $r'/R$ | $i'/I$ | $z'$ |
|---|---|---|---|---|---|---|
| CL1226+3332 | 0.89 | MegaCam 4.7 ks | SuprimeCam 2.2 ks | | ACS@HST 4.3 ks | SuprimeCam 1.1 ks |
| CL0152−1358 | 0.83 | FORS1 9.5 ks | SuprimeCam 7.2 ks | SuprimeCam 7.0 ks | SuprimeCam 4.5 ks | SuprimeCam 3.0 ks |
| CL1221+4918 | 0.70 | | | | | |
| CL0542-4100 | 0.69 | | | | | |
| CL1202+5751 | 0.68 | | | | | |
| CL0956+4107 | 0.59 | | | | | |
| CL1120+2326 | 0.56 | WFPC2@HST 13.4 ks | | | | |
| CL1354−0221 | 0.55 | FORS1 5.9 ks | FORS1 1.8 ks | FORS1 4.5 ks | ACS@HST 2.1 ks | FORS2 2.6 ks |
| CL1002+6858 | 0.50 | | SuprimeCam 15.1 ks | | SuprimeCam 9.0 ks | |
| CL0926+1242 | 0.49 | | | | | |
| CL0958+4702 | 0.39 | | | | | |

# Bibliography


Abell, G. O. 1958, ApJS, 3, 211

Akritas, M. G. & Bershady, M. A. 1996, ApJ, 470, 706

Albrecht, A., Bernstein, G., Cahn, R., et al. 2006, astro-ph/0609591

Allen, S. W., Evrard, A. E., & Mantz, A. B. 2011, ARA&A, 49, 409

Allen, S. W., Rapetti, D. A., Schmidt, R. W., et al. 2008, MNRAS, 383, 879

Amendola, L. & Tsujikawa, S. 2010, Dark Energy: Theory and Observations

Applegate, D. E., Mantz, A., Allen, S. W., et al. 2016, MNRAS, 457, 1522

Applegate, D. E., von der Linden, A., Kelly, P. L., et al. 2014, MNRAS, 439, 48

Arnaud, M., Pratt, G. W., Piffaretti, R., et al. 2010, A&A, 517, A92

Baade, D., Meisenheimer, K., Iwert, O., et al. 1999, The Messenger, 95, 15

Bartelmann, M. & Schneider, P. 2001, Phys. Rep., 340, 291

Battaglia, N., Bond, J. R., Pfrommer, C., & Sievers, J. L. 2012, ApJ, 758, 74

Becker, M. R. & Kravtsov, A. V. 2011, ApJ, 740, 25

Bertin, E. 2006, in Astronomical Society of the Pacific Conference Series, Vol. 351, Astronomical Data Analysis Software and Systems XV, ed. C. Gabriel, C. Arviset, D. Ponz, & S. Enrique, 112

Bertin, E. & Arnouts, S. 1996, A&AS, 117, 393

Bertin, E., Mellier, Y., Radovich, M., et al. 2002, in Astronomical Society of the Pacific Conference Series, Vol. 281, Astronomical Data Analysis Software and Systems XI, ed. D. A. Bohlender, D. Durand, & T. H. Handley, 228

Bhattacharya, S., Habib, S., Heitmann, K., & Vikhlinin, A. 2013, ApJ, 766, 32

Binney, J. & Tremaine, S. 1987, Galactic dynamics, ed. Binney, J. & Tremaine, S.

Birkinshaw, M., Gull, S. F., & Northover, K. J. E. 1978, MNRAS, 185, 245

Bleem, L. E., Stalder, B., de Haan, T., et al. 2015, ApJS, 216, 27

Bocquet, S., Saro, A., Dolag, K., & Mohr, J. J. 2016, MNRAS, 456, 2361

Borgani, S. & Guzzo, L. 2001, Nature, 409, 39

Borgani, S. & Kravtsov, A. 2011, Advanced Science Letters, 4, 204

Borm, K., Reiprich, T. H., Mohammed, I., & Lovisari, L. 2014, A&A, 567, A65

Boulade, O., Charlot, X., Abbon, P., et al. 2003, in Society of Photo-Optical Instrumentation Engineers (SPIE) Conference Series, Vol. 4841, Instrument Design and Performance for Optical/Infrared Ground-based Telescopes, ed. M. Iye & A. F. M. Moorwood, 72–81

Boylan-Kolchin, M., Springel, V., White, S. D. M., Jenkins, A., & Lemson, G. 2009, MNRAS, 398, 1150

Bryan, G. L. & Norman, M. L. 1998, ApJ, 495, 80

Burenin, R. A., Vikhlinin, A., Hornstrup, A., et al. 2007, ApJS, 172, 561

Carlstrom, J. E., Holder, G. P., & Reese, E. D. 2002, ARA&A, 40, 643

Cavaliere, A. & Fusco-Femiano, R. 1976, A&A, 49, 137

Cavaliere, A. G., Gursky, H., & Tucker, W. H. 1971, Nature, 231, 437

Clowe, D., Bradač, M., Gonzalez, A. H., et al. 2006, ApJ, 648, L109

Clowe, D., Gonzalez, A., & Markevitch, M. 2004, ApJ, 604, 596

Coles, P. & Lucchin, F. 2002, Cosmology: The Origin and Evolution of Cosmic Structure, Second Edition, 512

Croston, J. H., Hardcastle, M. J., & Birkinshaw, M. 2005, MNRAS, 357, 279

Cui, W., Borgani, S., Dolag, K., Murante, G., & Tornatore, L. 2012, MNRAS, 423, 2279

Donahue, M., Voit, G. M., Mahdavi, A., et al. 2014, ApJ, 794, 136

Doria, A., Gitti, M., Ettori, S., et al. 2012, ApJ, 753, 47

Dressler, A. M., Sutin, B. M., & Bigelow, B. C. 2003, in Discoveries and Research Prospects from 6- to 10-Meter-Class Telescopes II, ed. P. Guhathakurta, Vol. 4834, 255–263

Elvis, M. 1976, MNRAS, 177, 7P

Ensslin, T. A., Biermann, P. L., Klein, U., & Kohle, S. 1998, A&A, 332, 395

Erben, T., Hildebrandt, H., Lerchster, M., et al. 2009, A&A, 493, 1197

Erben, T., Hildebrandt, H., Miller, L., et al. 2013, MNRAS, 433, 2545

Erben, T., Schirmer, M., Dietrich, J. P., et al. 2005, Astronomische Nachrichten, 326, 432

Erben, T., Van Waerbeke, L., Bertin, E., Mellier, Y., & Schneider, P. 2001, A&A, 366, 717

Fabian, A. C. 1994, ARA&A, 32, 277

Fedeli, C., Bartelmann, M., Meneghetti, M., & Moscardini, L. 2008, A&A, 486, 35

Feretti, L. & Giovannini, G. 2008, in Lecture Notes in Physics, Berlin Springer Verlag, Vol. 740, A Pan-Chromatic View of Clusters of Galaxies and the Large-Scale Structure, ed. M. Plionis, O. López-Cruz, & D. Hughes, 143–+

Ferrari, C., Govoni, F., Schindler, S., Bykov, A. M., & Rephaeli, Y. 2008, Space Sci.Rev., 134, 93

Friedmann, A. 1922, Zeitschrift fur Physik, 10, 377

Giacconi, R., Murray, S., Gursky, H., et al. 1972, ApJ, 178, 281

Ginzburg, V. L. & Syrovatskii, S. I. 1965, ARA&A, 3, 297

Giodini, S., Lovisari, L., Pointecouteau, E., et al. 2013, Space Sci.Rev., 177, 247

Giovannini, G., Feretti, L., Venturi, T., Kim, K., & Kronberg, P. P. 1993, ApJ, 406, 399

Gitti, M., Brighenti, F., & McNamara, B. R. 2012, Advances in Astronomy, 2012, 950641

Gitti, M., Brunetti, G., & Setti, G. 2002, A&A, 386, 456

Hajian, A., Battaglia, N., Spergel, D. N., et al. 2013, J. Cosmology Astropart. Phys., 11, 064

Hartlap, J., Schrabback, T., Simon, P., & Schneider, P. 2009, A&A, 504, 689

Hektor, A., Raidal, M., & Tempel, E. 2013, ApJ, 762, L22

Henry, J. P. & Arnaud, K. A. 1991, ApJ, 372, 410

Heymans, C., Van Waerbeke, L., Bacon, D., et al. 2006, MNRAS, 368, 1323

High, F. W., Hoekstra, H., Leethochawalit, N., et al. 2012, ApJ, 758, 68

High, F. W., Stubbs, C. W., Rest, A., Stalder, B., & Challis, P. 2009, AJ, 138, 110

Hildebrandt, H., Erben, T., Dietrich, J. P., et al. 2006, A&A, 452, 1121

Hoekstra, H. 2003, MNRAS, 339, 1155

Hoekstra, H. 2013, Weak gravitational lensing

Hoekstra, H., Franx, M., Kuijken, K., & Squires, G. 1998, ApJ, 504, 636

Hoekstra, H., Herbonnet, R., Muzzin, A., et al. 2015, MNRAS, 449, 685

Hoekstra, H., Mahdavi, A., Babul, A., & Bildfell, C. 2012, MNRAS, 427, 1298

Hu, W. & Dodelson, S. 2002, ARA&A, 40, 171

Ilbert, O., Capak, P., Salvato, M., et al. 2009, ApJ, 690, 1236

Israel, H., Erben, T., Reiprich, T. H., et al. 2010, A&A, 520, A58

Israel, H., Erben, T., Reiprich, T. H., et al. 2012, A&A, 546, A79

Israel, H., Reiprich, T. H., Erben, T., et al. 2014, A&A, 564, A129

Israel, H., Schellenberger, G., Nevalainen, J., Massey, R., & Reiprich, T. H. 2015, MNRAS, 448, 814

Jenkins, A., Frenk, C. S., White, S. D. M., et al. 2001, MNRAS, 321, 372

Jones, C. & Forman, W. 1984, ApJ, 276, 38

Kaiser, N. 1986, MNRAS, 222, 323

Kaiser, N. & Squires, G. 1993, ApJ, 404, 441

Kaiser, N., Squires, G., & Broadhurst, T. 1995, ApJ, 449, 460

Karzas, W. J. & Latter, R. 1961, ApJS, 6, 167

Kellogg, E., Baldwin, J. R., & Koch, D. 1975, ApJ, 199, 299

Kelly, B. C. 2007, ApJ, 665, 1489

Kelly, P. L., von der Linden, A., Applegate, D. E., et al. 2014, MNRAS, 439, 28

King, I. 1962, AJ, 67, 471

Klein, M. 2013, PhD Thesis, Uni-Bonn

Kravtsov, A. V., Vikhlinin, A., & Nagai, D. 2006, ApJ, 650, 128

LaRoque, S. J., Bonamente, M., Carlstrom, J. E., et al. 2006, ApJ, 652, 917

Laureijs, R. 2009, Euclid Assessment Study Report, astro-ph/0912.0914

Lemaître, G. 1933, Annales de la Société Scientifique de Bruxelles, 53

Liang, Y.-F., Shen, Z.-Q., Li, X., et al. 2016, Phys.Rev.D, 93, 103525

Lin, Y., Mohr, J. J., & Stanford, S. A. 2003, ApJ, 591, 749

Luppino, G. A. & Kaiser, N. 1997, ApJ, 475, 20

Mahdavi, A., Hoekstra, H., Babul, A., et al. 2013, ApJ, 767, 116

Mantz, A., Allen, S. W., Ebeling, H., & Rapetti, D. 2008, MNRAS, 387, 1179

Mantz, A., Allen, S. W., Ebeling, H., Rapetti, D., & Drlica-Wagner, A. 2010a, MNRAS, 406, 1773

Mantz, A., Allen, S. W., Rapetti, D., & Ebeling, H. 2010b, MNRAS, 406, 1759

Mantz, A. B., Allen, S. W., Morris, R. G., et al. 2016, Submitted to MNRAS, astro-ph/1606.03407

Mantz, A. B., von der Linden, A., Allen, S. W., et al. 2015, MNRAS, 446, 2205

Martino, R., Mazzotta, P., Bourdin, H., et al. 2014, MNRAS, 443, 2342

Maughan, B. J. 2007, ApJ, 668, 772

McHardy, I. M. 1979, MNRAS, 188, 495

McNamara, B. R. & Nulsen, P. E. J. 2007, ARA&A, 45, 117

Medezinski, E., Broadhurst, T., Umetsu, K., et al. 2010, MNRAS, 405, 257

Medezinski, E., Umetsu, K., Okabe, N., et al. 2016, ApJ, 817, 24

Menanteau, F., González, J., Juin, J.-B., et al. 2010, ApJ, 723, 1523

Merloni, A., Predehl, P., Becker, W., et al. 2012, astro-ph/1209.3114

Merten, J., Meneghetti, M., Postman, M., et al. 2015, ApJ, 806, 4

Miley, G. 1980, ARA&A, 18, 165

Mills, B. Y. 1960, Australian Journal of Physics, 13, 550

Mortonson, M. J., Weinberg, D. H., & White, M. 2014, Particle Data Group 2014 Review of Particle Physics, astro-ph/1401.0046

Nagai, D., Vikhlinin, A., & Kravtsov, A. V. 2007, ApJ, 655, 98

Nandra, K., Barret, D., Barcons, X., et al. 2013, White Paper ESA Science program, astro-ph/1306.2307

Navarro, J. F., Frenk, C. S., & White, S. D. M. 1997, ApJ, 490, 493

Okabe, N. & Smith, G. P. 2016, MNRAS, 461, 3794

Parekh, V., van der Heyden, K., Ferrari, C., Angus, G., & Holwerda, B. 2015, A&A, 575, A127

Peacock, J. A. 1999, Cosmological Physics, 704

Peacock, J. A., Schneider, P., Efstathiou, G., et al. 2006, ESA-ESO Working Group on "Fundamental Cosmology", Tech. rep.

Pedlar, A., Ghataure, H. S., Davies, R. D., et al. 1990, MNRAS, 246, 477

Perlmutter, S., Aldering, G., Goldhaber, G., et al. 1999, ApJ, 517, 565

Pillepich, A., Porciani, C., & Reiprich, T. H. 2012, MNRAS, 422, 44

Pinzke, A. & Pfrommer, C. 2010, MNRAS, 409, 449

Planck Collaboration, Ade, P. A. R., Aghanim, N., et al. 2014, A&A, 571, A16

Planck Collaboration, Ade, P. A. R., Aghanim, N., et al. 2015a, Submitted to A&A, astro-ph/1502.01598

Planck Collaboration, Ade, P. A. R., Aghanim, N., et al. 2015b, Accepted by A&A, astro-ph/1502.01589

Planck Collaboration, Ade, P. A. R., Aghanim, N., et al. 2015c, astro-ph/1502.01597

Planck Collaboration, Aghanim, N., Arnaud, M., et al. 2011, A&A, 536, A26

Pointecouteau, E., Reiprich, T. H., Adami, C., et al. 2013, Athena+ supporting paper, astro-ph/1306.2319

Postman, M., Coe, D., Benítez, N., et al. 2012, ApJS, 199, 25

Pratt, G. W., Croston, J. H., Arnaud, M., & Böhringer, H. 2009, A&A, 498, 361

Predehl, P., Andritschke, R., Böhringer, H., et al. 2010, in Space Telescopes and Instrumentation 2010: Ultraviolet to Gamma Ray, Vol. 7732, 77320U

Press, W. H. & Schechter, P. 1974, ApJ, 187, 425

Rasia, E., Meneghetti, M., Martino, R., et al. 2012, New Journal of Physics, 14, 055018

Reichert, A., Böhringer, H., Fassbender, R., & Mühlegger, M. 2011, A&A, 535, A4

Reiprich, T. H., Basu, K., Ettori, S., et al. 2013, Space Sci.Rev., 177, 195

Reiprich, T. H. & Böhringer, H. 2002, ApJ, 567, 716

Riess, A. G., Filippenko, A. V., Challis, P., et al. 1998, AJ, 116, 1009

Rines, K. & Diaferio, A. 2006, AJ, 132, 1275

Robertson, H. P. 1935, ApJ, 82, 284

Roland, J., Véron, P., Pauliny-Toth, I. I. K., Preuss, E., & Witzel, A. 1976, A&A, 50, 165

Rosati, P., Borgani, S., & Norman, C. 2002, ARA&A, 40, 539

Rowley, D. R., Thomas, P. A., & Kay, S. T. 2004, MNRAS, 352, 508

Rozo, E., Rykoff, E. S., Bartlett, J. G., & Evrard, A. 2014, MNRAS, 438, 49

Rybicki, G. B. & Lightman, A. P. 1979, Radiative processes in astrophysics, ed. Rybicki, G. B. & Lightman, A. P.

Sarazin, C. L. 1986, Reviews of Modern Physics, 58, 1

Schellenberger, G., Reiprich, T. H., Lovisari, L., Nevalainen, J., & David, L. 2015, A&A, 575, A30

Schirmer, M. 2013, ApJS, 209, 21

Schirmer, M., Erben, T., Hetterscheidt, M., & Schneider, P. 2007, A&A, 462, 875

Schlegel, D. J., Finkbeiner, D. P., & Davis, M. 1998, ApJ, 500, 525

Schneider, P. 1996, MNRAS, 283, 837

Schneider, P. 2006, in Saas-Fee Advanced Course 33: Gravitational Lensing: Strong, Weak and Micro, ed. G. Meylan, P. Jetzer, P. North, P. Schneider, C. S. Kochanek, & J. Wambsganss, 269–451

Schneider, P. 2015, Extragalactic Astronomy and Cosmology: An Introduction

Schneider, P., van Waerbeke, L., Kilbinger, M., & Mellier, Y. 2002, A&A, 396, 1

Schrabback, T., Erben, T., Simon, P., et al. 2007, A&A, 468, 823

Seitz, C. & Schneider, P. 1997, A&A, 318, 687

Seitz, S. & Schneider, P. 1996, A&A, 305, 383

Seitz, S. & Schneider, P. 2001, A&A, 374, 740

Sereno, M. & Ettori, S. 2015, MNRAS, 450, 3633

Sheth, R. K. & Tormen, G. 2002, MNRAS, 329, 61

Simet, M., Battaglia, N., Mandelbaum, R., & Seljak, U. 2015, Submitted to MNRAS, astro-ph 1502.01024

Simionescu, A., Allen, S. W., Mantz, A., et al. 2011, Science, 331, 1576

Skrutskie, M. F., Cutri, R. M., Stiening, R., et al. 2006, AJ, 131, 1163

Smith, G. P., Mazzotta, P., Okabe, N., et al. 2016, MNRAS, 456, L74

Sunyaev, R. A. & Zel'dovich, Y. B. 1970, Comments on Astrophysics and Space Physics, 2, 66

Tinker, J., Kravtsov, A. V., Klypin, A., et al. 2008, ApJ, 688, 709

Umetsu, K., Medezinski, E., Nonino, M., et al. 2014, ApJ, 795, 163

van den Bergh, S. 1961, ApJ, 134, 970

Vikhlinin, A., Burenin, R. A., Ebeling, H., et al. 2009a, ApJ, 692, 1033

Vikhlinin, A., Kravtsov, A. V., Burenin, R. A., et al. 2009b, ApJ, 692, 1060

Voevodkin, A. & Vikhlinin, A. 2004, ApJ, 601, 610

Voit, G. M. 2005, Reviews of Modern Physics, 77, 207

von der Linden, A., Allen, M. T., Applegate, D. E., et al. 2014a, MNRAS, 439, 2

von der Linden, A., Mantz, A., Allen, S. W., et al. 2014b, MNRAS, 443, 1973

Walker, A. G. 1937, Proc. London Math. Soc. 1937, s2-42, 90

Warren, M. S., Abazajian, K., Holz, D. E., & Teodoro, L. 2006, ApJ, 646, 881

Wolf, M. 1906, Astronomische Nachrichten, 170, 211

Wright, C. O. & Brainerd, T. G. 2000, ApJ, 534, 34

Wu, H.-Y., Zentner, A. R., & Wechsler, R. H. 2010, ApJ, 713, 856

Zhang, Y.-Y., Laganá, T. F., Pierini, D., et al. 2011, A&A, 535, A78

Ziparo, F., Smith, G. P., Okabe, N., et al. 2015, Submitted to MNRAS, astro-ph/1507.04376

Zitrin, A., Rosati, P., Nonino, M., et al. 2012, ApJ, 749, 97

Zwicky, F. 1933, Helvetica Physica Acta, 6, 110

Zwicky, F. 1957, Morphological astronomy, ed. Zwicky, F.

# List of Figures

# List of Tables

# Acknowledgements

Along an important path it is inevitable to meet important people which I would like to thank here. In the last years I had the great luck not only to find extremely competent collaborators and advisors, but also very friendly individuals in everyday life. With this premise, it will not be surprising to see some repetition in my thanksgivings below.

My supervisor, Thomas H. Reiprich, comes first in the list as he made all this possible, allowing me to start from scratch with a topic so different from my previous background. It was a pleasure working with him and in his research group, which has become like a family to me. Special thanks go to Thomas Erben for his contribution to part of the data reduction, and to Peter Schneider for always being willing to discuss and give suggestions. A big "thank you" to Zeinab Shafiee for her collaboration with the WFI data analysis and, of course, Holger Israel and Matthias Klein which did not leave me without support despite the distance. I thank Alexey Vikhlinin for providing us the corrected X-ray luminosities of our sample.

I acknowledge the *International Max Planck Research School* of the Max Planck Institute für Astronomie and the *Bonn Cologne Graduate School* for financial support, which allowed me to broaden my knowledge with school and conferences and to train useful soft skills.

At AIfA I have appreciated the kindness of many colleagues and friends. I thank Gerrit for helping me to dust off my reminiscence on the X-ray analysis. Emilio e Luca F. for the "IT" rescue in critical conditions. Ellen and Sabine for the their kind help with bureaucracy. My officemates Axel and Dominik for the perfect harmony we had everyday in our room. I cannot miss the chance to truly thank the old and the new members of the group, Thomas, Lorenzo, Gerrit, Katharina, Bharad, Aarti, Miriam, Florian and Sofia.

For the very good times at lunch, outside or in short breaks I am grateful to (in alphabetical order): Carlo, Emiliano, Enrico, Gerrit, Jeff, Lorenzo, Luca G., Luca F., Matteo, Michele, Monica, Patrick, Thomas, Zahra. Also, thanks to the *Blazing Suns*, for helping me to reduce the stress with two baskets and a ball.

I thank Elisabetta for her great support and patience, especially in the last very busy period. The motivation from my family is something I have always given for granted, but a "thank you" might not be enough to pay back for the great effect that their presence does on me.

And the last thought goes to my far friends back home which, no matter how many kilometers are between us, have always been close.